Formation and Near-field Dynamics of a Wing Tip Vortex

Thesis by

Lavi R. Zuhal

In Partial Fulfillment of the Requirements for the Degree of

Doctor of Philosophy

California Institute of Technology

Pasadena, California

2001

(Defended April 20, 2001)

Acknowledgments

At an age when most young men have entered the world to make their fortune, I struggled with mathematics, science and the mysteries of the natural world. Those were difficult days, but days that I will look back upon with fond memories. There are many people, too many to mention in these few paragraphs, who helped me to get to this point and succeed where others have failed. I would like to take this opportunity to thank some of the people who contributed most toward the completion of this thesis.

I would like to thank my advisor Prof. Morteza Gharib for giving me the opportunity to work on this project. He gave me advice and direction while allowing me the freedom to develop the project according to my own vision. I would like to thank Profs. Hornung, Leonard, Shepherd, and Colonius for graciously agreeing to be members of my thesis committee. Their comments and suggestions were very helpful for making this thesis the "masterpiece" that you are about to read.

The many past and present members of Prof. Gharib's research group have lent their knowledge and experience in giving me many suggestions that saved hours and days of trial and error in perfecting the experimental setup and procedure. In particular, I would like to express my gratitude to Dr. Dana Dabiri, Dr. David Jeon, and Herrn Dr. sc. techn. Heinrich Stüer.

I would like to thank the many friends who made my stay at Caltech almost bearable. My experience would not be complete without a well-balanced, daily meal from the Chandler Dining facility and "intellectual" conversations with my lunchtime companions Dr. Eric Burcsu, Dr. Sandeep Sane, Ioannis Chasiotis, and Benjamin Chow. Dr. Burcsu deserves special recognition for his continuous lunch attendance over the past five years.

Few people have had such a great influence on my personal and scientific development than Nitin "Desh" Deshpande. Desh, a native Punenian, who is very proud of his Punenianity, has been a continuous inspiration to all of us. As an Aeronautical Engineer, he has made significant contributions to the "aircraft air-conditioning" industry. As a vegetarian, he introduced me to the wonders of "Punenian veggie," as well as many other aspects of Punenian food and culture.

This work is dedicated to my parents who have given me so much that it's impossible to put into words.

Abstract

The search for a more efficient method to destroy aircraft trailing vortices requires a good understanding of the early development of the vortices. For that purpose, an experimental investigation has been conducted to study the formation and near-field dynamics of a wing tip vortex.

Two versions of the Digital Particle Image Velocimetry (DPIV) technique were used in the studies. Planar DPIV was used to obtain velocity fields adjacent to the wing surface. Stereoscopic DPIV, which allows instantaneous measurements of all three components of velocity within a planar slice, was used to measure velocity fields behind the wing. The trailing vortex was produced by a rectangular half-wing model with an NACA 0012 profile. All measurements were made at Reynolds number, based on chord length, of 9040.

The present study has found that the wing sheds multiple vortices. A structure that closely resembles a wing tip vortex is first observed on the suction side of the wing near the tip at the mid-chord section of the wing. At the trailing edge of the wing, a smaller vortex with an opposite sense of rotation is observed next to the tip vortex. In addition to the two vortices, two vortex layers with opposite sense of rotation, one on the pressure side and one on the suction side, are apparent at the trailing edge. Farther downstream, most of the vorticity in the vortex layer, with the same sense of rotation as the tip vortex, rolls up into the wing tip vortex. The vortices, with opposite sense of rotation, break up into smaller vortices which orbit around the tip vortex. At least one

relatively strong satellite vortex appears in some of the instantaneous fields. The studies found that the interaction of the tip vortex and satellite vortices give rise to the unsteady motion of the wing tip vortex. In addition, the studies also examined the effects of the boundary layer and the tip geometry to the strength and motion of the trailing vortex.

Table of Contents

ACKNOWLEDGMENTS ..... **III**

ABSTRACT ..... **V**

TABLE OF CONTENTS ..... **VII**

LIST OF FIGURES ..... **X**

LIST OF TABLES ..... **XII**

LIST OF SYMBOLS ..... **XIII**

INTRODUCTION **1**

1.1 Introduction 1
1.2 Reviews 2
1.3 Objectives and Organization of Thesis 5

EXPERIMENTAL METHODS **8**

2.1 Introduction 8
2.2 Planar DPIV 9
2.3 Stereoscopic PIV 10
2.4 Implementation 11
2.4.1 Planar DPIV *11*
2.4.2 SPIV *11*

EXPERIMENTAL SETUP **20**

3.1 Testing Facility 20
3.2 The Wing Model 20
3.3 SPIV Setup 21
3.3.1 Light Sheet *22*
3.3.2 Image Recording *23*
3.3.3 Seeding *23*
3.4 Planar DPIV Setup 24

3-COMPONENT VELOCITY FIELDS BEHIND THE WING **29**

4.1 Introduction 29
4.2 Experimental Conditions 29
4.3 Averaging Methodology 30
4.4 Stereoscopic DPIV Results 32
4.4.1 Z/C = 0 ..... *34*
4.4.2. Z/C = 1 ..... *35*
4.4.3 Z/C = 2 ..... *36*
4.4.4 Z/C = 3 ..... *36*
4.4.5 Z/C = 4 ..... *37*
4.4.6 Z/C = 5 ..... *37*

STRUCTURE OF THE WING TIP VORTEX **56**

5.1 INTRODUCTION 56
5.2 CROSSFLOW PLANE PROFILES 57
5.2.1 Azimuthal Velocity Profile *57*
5.2.2 Axial Velocity Profile *58*
5.2.3 Out-of-plane Vorticity Profile *60*
5.3 CIRCULATION 61
5.4 CORE SIZE 65
5.5 COMPARISON WITH THEORY 67
5.6 SUMMARY 68

DYNAMICS OF THE WING TIP VORTEX 82

6.1 INTRODUCTION 82
6.2 AVERAGE AXIAL VORTICITY DISTRIBUTIONS 83
6.2.1 Vorticity Distributions at the Trailing Edge of the Wing *83*
6.2.2 Streamwise Evolution of the Wing Tip Vortex *84*
6.2.3 Vortex Core Trajectory *86*
6.3 INSTANTANEOUS VORTICITY DISTRIBUTIONS 88
6.3.1 Instantaneous Core Location *91*
6.4 SUMMARY 93

FORMATION OF THE WING TIP VORTEX 113

7.1 INTRODUCTION 113
7.2 EXPERIMENTAL CONDITIONS 113
7.3 VELOCITY AND VORTICITY FIELDS AROUND THE WING TIP 114
7.3.1 $\alpha = 0^0$ Case *115*
7.3.2 $\alpha = 4^0$ Case *117*
7.4 SUMMARY 119

EFFECTS OF BOUNDARY LAYER AND TIP GEOMETRY 134

8.1 INTRODUCTION 134
8.2 EXPERIMENTAL CONDITIONS 135
8.2.1 Boundary Layer Modification *135*
8.2 2 Wing Tip Modifications *135*
8.3 VORTICITY DISTRIBUTIONS 136
8.3.1 Boundary Layer Modification *136*
8.3.2 Wing Tip Modification (Rounded Tip Geometry) *138*
8.3.3 Comparison Between Different Types of Wing Tip Geometry *139*
8.4 STRUCTURE OF THE VORTEX CORE 142
8.5 INSTANTANEOUS CORE LOCATION 144
8.6 SUMMARY 146

SUMMARY AND CONCLUSIONS 166

9.1 VELOCITY FIELD BEHIND THE WING 166
9.2 VORTICITY FIELD BEHIND THE WING 168
9.3 FLOW ADJACENT TO THE WING TIP 168
9.4 EFFECTS OF BOUNDARY LAYER AND TIP GEOMETRY 169

REFERENCES..... 171

List of Figures

Figure 2.1. Photograph of Scheimpflug adaptor 16
Figure 2.2. Angular lens configuration 16
Figure 2.3. Calibration grid 17
Figure 2.4. Schematic for the SPIV 3-component reconstructions 18
Figure 3.1. Photograph of the setup 26
Figure 3.2. Light sheet optics 27
Figure 3.3. Schematic of planar DPIV setup 27
Figure 4.1. Schematic of the setup and the coordinate system 39
Figure 4.2. Running average vs. number of velocity fields 39
Figure 4.3. Average values computed with the two averaging methods 40
Figure 4.4. Three-component velocity field close to trailing edge of the wing 41
Figure 4.5. Velocity fields, z/c = 0, $\alpha = 0^0$ 42
Figure 4.6. Velocity fields, z/c = 0, $\alpha = 2^0$ 43
Figure 4.7. Velocity fields, z/c = 0, $\alpha = 10^0$ 44
Figure 4.8. Velocity fields, z/c = 1, $\alpha = 2^0$ 45
Figure 4.9. Velocity fields, z/c = 1, $\alpha = 10^0$ 46
Figure 4.10. Velocity fields, z/c = 2, $\alpha = 2^0$ 47
Figure 4.11. Velocity fields, z/c = 2, $\alpha = 10^0$ 48
Figure 4.12. Velocity fields, z/c = 3, $\alpha = 2^0$ 49
Figure 4.13. Velocity fields, z/c = 3, $\alpha = 10^0$ 50
Figure 4.14. Velocity fields, z/c = 4, $\alpha = 2^0$ 51
Figure 4.15. Velocity fields, z/c = 4, $\alpha = 10^0$ 52
Figure 4.16. Velocity fields, z/c = 5, $\alpha = 2^0$ 53
Figure 4.17. Velocity fields, z/c = 5, $\alpha = 10^0$ 54
Figure 5.1. Azimuthal velocity profile for $\alpha = 2^0$ case 71
Figure 5.2. Azimuthal velocity profile for $\alpha = 4^0$ case 71
Figure 5.3. Azimuthal velocity profile for $\alpha = 6^0$ case 71
Figure 5.4. Azimuthal velocity profile for $\alpha = 8^0$ case 72
Figure 5.5. Azimuthal velocity profile for $\alpha = 10^0$ case 72
Figure 5.6. Axial velocity profile for $\alpha = 2^0$ case 73
Figure 5.7. Axial velocity profile for $\alpha = 4^0$ case 73
Figure 5.8. Axial velocity profile for $\alpha = 6^0$ case 73
Figure 5.9. Axial velocity profile for $\alpha = 8^0$ case 74
Figure 5.10. Axial velocity profile for $\alpha = 10^0$ case 74
Figure 5.11. Out-of-plane vorticity profile for $\alpha = 2^0$ case 75
Figure 5.12. Out-of-plane vorticity profile for $\alpha = 4^0$ case 75
Figure 5.13. Out-of-plane vorticity profile for $\alpha = 6^0$ case 75
Figure 5.14. Out-of-plane vorticity profile for $\alpha = 8^0$ case 76
Figure 5.15. Out-of-plane vorticity profile for $\alpha = 10^0$ case 76
Figure 5.16. Peak vorticity vs. Z/C 76
Figure 5.17. Circulation vs. radius for $\alpha = 2^0$ case 77
Figure 5.18. Circulation vs. radius for $\alpha = 4^0$ case 77

Figure 5.19. Circulation vs. radius for $\alpha = 6^0$ case 77
Figure 5.20. Circulation vs. radius for $\alpha = 8^0$ case 78
Figure 5.21. Circulation vs. radius for $\alpha = 10^0$ case 78
Figure 5.22. Mean V_θ vs. radius 79
Figure 5.23. Core radius vs. Z/C 79
Figure 5.24. Maximum V_θ vs. Z/C 80
Figure 5.25. Minimum w vs. Z/C 80
Figure 5.26. Core radius vs. Z/C 80
Figure 6.1. Axial vorticity field, $\alpha = 0^0$, Z/C = 0 94
Figure 6.2. Axial vorticity field, $\alpha = 2^0$, Z/C = 0 94
Figure 6.3. Axial vorticity field, $\alpha = 4^0$, Z/C = 0 95
Figure 6.4. Axial vorticity field, $\alpha = 6^0$, Z/C = 0 95
Figure 6.5. Axial vorticity field, $\alpha = 8^0$, Z/C = 0 96
Figure 6.6. Axial vorticity field, $\alpha = 10^0$, Z/C = 0 96
Figure 6.7. Axial vorticity fields at Z/C = 0.5 97
Figure 6.8. Axial vorticity fields at Z/C = 1 98
Figure 6.9. Axial vorticity fields at Z/C = 1.5 99
Figure 6.10. Axial vorticity fields at Z/C = 2 100
Figure 6.11. Axial vorticity fields at Z/C = 3 101
Figure 6.12. Axial vorticity fields at Z/C = 4 102
Figure 6.13. Average core trajectories 103
Figure 6.14. Instantaneous vorticity fields, $\alpha = 4^0$, Z/C = 0 104
Figure 6.15. Instantaneous vorticity fields, $\alpha = 8^0$, Z/C = 0 105
Figure 6.16. Instantaneous vorticity fields, $\alpha = 4^0$, Z/C = 4 106
Figure 6.17. Instantaneous vorticity fields, $\alpha = 8^0$, Z/C = 4 107
Figure 6.18. Instantaneous vorticity fields, $\alpha = 2^0$, Z/C = 3 108
Figure 6.19. Instantaneous vorticity fields, $\alpha = 2^0$, Z/C = 3 109
Figure 6.20. Instantaneous locations of the vortex core 110
Figure 6.21. Rms vs. Z/C 111
Figure 7.1. Schematic of the experimental setup 121
Figure 7.2. Measurement plane locations for $\alpha = 0^0$ case 121
Figure 7.3. Axial vorticity field, N = 1, $\alpha = 0^0$ 122
Figure 7.4. Axial vorticity field, N = 2, $\alpha = 0^0$ 123
Figure 7.5. Axial vorticity field, N = 3, $\alpha = 0^0$ 124
Figure 7.6. Axial vorticity field, N = 4, $\alpha = 0^0$ 125
Figure 7.7. Axial vorticity field, N = 5, $\alpha = 0^0$ 126
Figure 7.8. Measurement plane locations for $\alpha = 4^0$ case 127
Figure 7.9. Axial vorticity field, N = 1, $\alpha = 4^0$ 128
Figure 7.10. Axial vorticity field, N = 2, $\alpha = 4^0$ 129
Figure 7.11. Axial vorticity field, N = 3, $\alpha = 4^0$ 130
Figure 7.12. Axial vorticity field, N = 4, $\alpha = 4^0$ 131
Figure 7.13. Axial vorticity field, N = 5, $\alpha = 4^0$ 132
Figure 8.1.a. Location of the trip wire 148
Figure 8.1.b. Modified wing tip geometries 149

Figure 8.2. Boundary layer modification, axial vorticity field, $\alpha = 4^0$, Z/C = 0 150
Figure 8.3. Boundary layer modification, axial vorticity field, $\alpha = 4^0$, Z/C = 1 151
Figure 8.4. Boundary layer modification, axial vorticity field, $\alpha = 4^0$, Z/C = 2 152
Figure 8.5. Boundary layer modification, axial vorticity field, $\alpha = 4^0$, Z/C = 3 153
Figure 8.6. Boundary layer modification, axial vorticity field, $\alpha = 4^0$, Z/C = 4 154
Figure 8.7. Tip geometry modification, axial vorticity field, $\alpha = 4^0$, Z/C = 0 155
Figure 8.8. Tip geometry modification, axial vorticity field, $\alpha = 4^0$, Z/C = 1 156
Figure 8.9. Tip geometry modification, axial vorticity field, $\alpha = 4^0$, Z/C = 2 157
Figure 8.10. Tip geometry modification, axial vorticity field, $\alpha = 4^0$, Z/C = 3 158
Figure 8.11. Tip geometry modification, axial vorticity field, $\alpha = 4^0$, Z/C = 4 159
Figure 8.12. Comparison between different types of wing tip geometry 160
Figure 8.13. Generation of the vortices of opposite sign for $\alpha = 0^0$ case 161
Figure 8.14. Comparison of the axial velocity profiles 162
Figure 8.15. Comparison of the circulation profiles of the main tip vortex 163
Figure 8.16. Instantaneous location of the vortex center for the three different cases .. 164

List of Tables

Table 5.1. Comparison of circulation at the trailing edge and the total circulation at Z/C = 4 65
Table 8.1. Circulation of the small opposite-signed vortex 144

List of Symbols

a	3-dimensional lift curve slope ($dC_l/d\alpha$)
AR	aspect ratio
α	angle of attack
α_1, α_2, β_1, β_2	angles between the cameras and the interrogation plane
b	wing span
C	chord length
C_l	lift coefficient
DPIV	Digital Particle Image Velocimetry
φ	angle between the lens plane and the camera plane
Γ	circulation
$\Gamma_{v, Z/C=0}$	wing tip vortex circulation at the trailing edge
l	lift per unit span
N	label for the streamwise location for measurement adjacent to the wing
ν	viscosity
ω	vorticity
P	pressure
P_{tot}	total pressure
r	vortex core radius
ρ	density
r_{avg}	average location of the vortex center
rms	root mean square

R	radial distance from the vortex center
Re	Reynolds number
T	nondimensional time
θ	angle between the object plane and the lens plane
U	freestream velocity
V_θ	azimuthal velocity
W	out-of-plane velocity
X	lateral coordinate
Y	vertical coordinate
Z	longitudinal coordinate
Z/C	nondimensional downstream distance from the wing

CHAPTER 1
Introduction

1.1 Introduction

The dynamics of trailing vortices are of great importance in engineering. Trailing vortices are produced at the tip of lifting surfaces where fluid accelerates from the high-pressure to the low-pressure region. The interest in understanding the dynamics of trailing vortices is motivated by the problems associated with their presence. One problem associated with tip vortices is the noise generation on rotorcraft. Blade vortex interaction has been identified as the major source of noise generated by a rotor. The noise is generated when a blade passes over tip vortices produced by other blades. Another problem is that of trailing vortices generated by aircraft wings. Large transport aircrafts are known to produce strong and persistence trailing vortices. These vortices induce rolling moments that can be hazardous to a following aircraft. The safety hazard presented by the trailing vortices determines the spacing distance between aircrafts during landing. This results in a limited number of airplanes that can land at an airport within a certain period of time, which obviously has some economic impact.

For the reasons presented above, wing tip vortices have been the subject of many investigations in the past. Most of the previous investigators focused their attention on the stability and the prediction of decay of these vortices in the far field. The dynamics

of trailing vortices in the far field is reasonably well understood and documented. However, the formation and the near field dynamics of wing tip vortices have not been adequately studied.

In this thesis, results from an experimental study of formation and the near field dynamics of wing tip vortices are presented. The wing tip vortices are studied by using two versions of Digital Particle Image Velocimetry (DPIV), which are non-intrusive global velocity measurements techniques. From the measured velocity fields, the formation, dynamics, and structure of the trailing vortex are examined.

1.2 Reviews

There are numerous publications found in the literature on the topics of wing tip vortices. In this section, we only review a few of those that are most relevant to the current study. Extensive reviews on the topics of wing tip vortices can be found in Widnall (1975) and Spalart (1998).

Measurements of velocity profiles have been attempted by many researchers in the past. Logan (1971) measured both azimuthal and axial velocity profiles by using five-hole pressure probes. He found that there is significant retardation of axial velocity within the vortex core over the downstream distance of 10-26 chord lengths behind the wing. Logan also reported that there is axial velocity excess at the edge of the vortex core. Baker et al. (1974) made a series of LDV measurements of the trailing vortex. They considered the effect of vortex meandering in the data analysis. Baker et al. (1974) reported that the vortex meandering reduced the maximum tangential velocity by approximately 30%. They also found that the measurements are in reasonable agreement

with the theory of Moore and Saffman. Bippes (1977) studied the tip vortex by means of hydrogen bubble method for flow visualization and photo-grammetric evaluation of photographs. From the results, Bippes concluded that the direction of the axial flow in the core depends on the Reynolds number. Green and Acosta (1991) performed trailing vortex measurements by using a double-pulsed holographic of injected micro bubbles. They found that the core mean axial velocity is consistently higher than the freestream velocity in the region close to the wing. Additionally, they found that the axial flow is highly unsteady. They also concluded that the axial velocity strongly depends on the Reynolds number (similar to Bippes conclusion). Devenport et al. (1996) examined the structure of wing tip vortices by using hot wire anemometry. They developed a theory to correct for the effects of vortex meandering. However, as mentioned in Spalart (1998), their strategy to correct the meandering effect is not definitive.

Almost all measurements mentioned in the above paragraph are performed by using either intrusive or point measurement techniques. However, it is well known that the wing tip vortex is very sensitive to disturbances from intrusive probes and can become subjected to a meandering motion. These problems can be resolved by employing the particle image velocimetry (PIV) technique. (The measurement technique employed by Green and Acosta is actually a primitive version of this.) A number of PIV measurements of the wing tip vortex have been conducted in the past. Vogt et al. (1996) used planar DPIV to measure wing tip vortex shed by an NACA 0012 wing. From the PIV measurements, they obtained azimuthal velocity profiles across the vortex core and showed that the profile looks different from LDV measurement results. Jacob et al. (1997) investigated the trailing vortex wake of a rectangular NACA 0012 wing (full

wing) up to a 1400 chord-length downstream by using planar DPIV. Their results showed that the maximum tangential velocity varies very little near the wing and decays in the region far from the wing. Recently, Chen et al. (1999) studied the wake of a flapped wing using planar DPIV. Their results showed that trailing vortices of a flapped wing exhibit Lamb-Oseen tangential velocity distribution with slow growth.

The existence of axial flow within the core of tip vortices was investigated analytically by several researchers. Batchelor (1964) showed that the axial flow in the core is a consequence of the low-pressure region within that core, which accelerates fluids in the core region faster than the freestream velocity (assuming that the flow is steady and the viscous effect can be neglected). He also gave a similarity solution for the flow in the far downstream. Moore and Saffman (1973) studied the structure of laminar trailing vortices by including the effect of core viscosity. They showed that the axial flow within the vortex core could be either higher or lower than the freestream velocity, depending on the distribution of tip loading on the wing. Both Batchelor's and Moore-Saffman's analyses are based on the assumption that the perturbation of the axial velocity within the core is very small.

The formation and early development of wing tip vortices have not been studied sufficiently. Part of the problem is that the flow is highly three-dimensional in the region near the wing, which makes it difficult to study this problem experimentally. Francis and Kennedy (1979) provide one of a few experimental studies on the formation of a trailing vortex. Francis and Kennedy investigated the formation of a wing tip vortex by using hot wire anemometry. They took velocity measurements close to the wing surface and inferred the vorticity field, in a region adjacent to the wing surface, from the velocity

measurements. Green (1988) performed a surface flow visualization to study the early stages of the vortex rollup process. Several numerical simulations to model the rollup of wing tip vortices have been performed in the past. The most common procedure is to replace the vorticity in the wake with a vortex sheet and study the evolution of the vortex sheet. Moore (1974) studied the rollup of vorticity shed by an elliptically loaded wing. Krasny (1987) numerically investigated the vortex sheet evolution for an elliptically loaded wing and a configuration that includes flap and fuselage.

1.3 Objectives and Organization of Thesis

The ultimate goal of research on wing tip vortices is to find a method that can accelerate the "destruction" of the trailing vortices. In real situations, trailing vortices generated by an aircraft normally undergo the so-called *Crow instability* (Crow 1970). This sinusoidal instability is caused by the interaction of the two trailing vortices generated by the wing. By this instability, the two vortices eventually touch each other and break into a series of vortex rings. The destruction of tip vortices by the Crow instability is more rapid than the viscous or turbulent decay of a single vortex (Widnall 1975). However, the destruction process by this instability is not very efficient since the instability grows very slowly. The search for another mechanism, which would lead to a more efficient way of eliminating trailing vortices, requires a good understanding of the early development of the vortices. Unfortunately, the early stages of the development of a wing tip vortex are still not well understood.

The objective of this thesis is to investigate the formation and the near field dynamics of a trailing vortex. This is achieved by performing global velocity

measurements using two versions of the Digital Particle Image Velocimetry technique. From the velocity measurements, the following can be studied and addressed:

1. The structure of the trailing vortex with the correction for the meandering effect.
2. The formation of the trailing vortex starting from its early stages on the wing surface.
3. The interaction between vortices shed by the wing and its effect on the motion of the trailing vortex.
4. The effect of wing tip geometry and the boundary layer on the strength and motion of the wing tip vortex.

The thesis is organized into nine chapters. The basic descriptions and implementation of the two versions of the PIV method used in the experiments are discussed in Chapter 2. The description of the apparatus used during the experimental phase is given in Chapter 3. The 3-components planar velocity fields, measured using stereoscopic PIV, are presented in Chapter 4. The structure of the measured wing tip vortex is considered in Chapter 5. In Chapter 6, the trailing vortex dynamics and vortex interactions behind the wing are examined. Results from velocity measurements around the wing surface are presented in Chapter 7. The effects of boundary layer and tip geometry are studied in Chapter 8. Finally, a summary and conclusions are given in Chapter 9.

CHAPTER 2
Experimental Methods

2.1 Introduction

It has been reported in the literature that there were various problems encountered by the previous researchers in conducting velocity measurements of wing tip vortices. Some of the problems encountered are the following:

1. The vortices are very sensitive to disturbances from intrusive probes.
2. The locations of the vortices are changing with time even in the steady conditions of the wind/water tunnels (vortex meandering phenomenon).
3. The flow is highly three-dimensional especially in the near field region.

These facts of course affect the choice of experimental methods used in the present study.

A measurement technique such as three-component laser-Doppler velocimetry (LDV) can guarantee no disturbance of the flow with high spatial and temporal resolution. However, vortex meandering phenomenon makes it difficult, if not impossible, to study this problem using pointwise measurement techniques. In addition, single-point diagnostic tools also require measurements at many locations within the vortex. This prevents instantaneous measurements of the whole region of study.

The dilemmas discussed in the above paragraphs lead us to choose a non-intrusive "field" measurement technique. Particle Image Velocimetry (PIV) is one of the existing

techniques that satisfies the requirements mentioned above. Digital particle image velocimetry (DPIV) is a technique capable of measuring two-component velocity field within a plane instantaneously. To address the three-dimensionality of the flow, three-component velocity measurements are preferred. There are several techniques, extended versions of DPIV, which allow instantaneous measurement of a three-component "planar" velocity field. One of these techniques is stereoscopic PIV (SPIV). Both DPIV and SPIV are used in the present study.

In the rest of this chapter, brief descriptions of DPIV and SPIV are given. The implementations of both methods in the present study are discussed.

2.2 Planar DPIV

In PIV, small and neutrally buoyant particles are added to the flow. The region of study is illuminated twice with a light sheet, generated by high-powered lasers. It is assumed that the particles move with the flow velocity between the two illuminations. The light scattered by the tracer particles during the two illuminations are focused onto two separate frames of a CCD sensor that is positioned parallel to the light sheet. The images are then acquired in real time and downloaded to the hard disk of a computer.

The projection of the local displacement vectors of the particles onto the plane of the light sheet is measured by cross-correlating the two sequential images. The image interrogation scheme used to obtain the displacement field is described in Willert and Gharib (1991). The velocity field is obtained by taking into account the time between exposures of the two successive images. Once the velocity field is obtained, other flow

quantities such as circulation, stream functions, and vorticity components normal to the plane of the light sheet can be numerically computed.

2.3 Stereoscopic PIV

In stereoscopic PIV, one measures three-component velocity field within a plane instantaneously. Among several other three-component PIV methods existing in the literature, SPIV was chosen in the present study because it is a direct extension of planar DPIV. The image interrogation scheme used in this technique is exactly the same as that use in planar DPIV.

The planar-three-component velocity field is obtained by comparing the in-plane displacement field as viewed by two cameras, placed at different locations, which are focused onto the same region in the flow. The in-plane displacement field as viewed by each camera is obtained by using the same routine as that used in planar DPIV.

Besides being a direct extension of planar DPIV, SPIV also has another advantage in the present experiment. The fact that SPIV takes into account the out-of-plane motion (which is ignored in 2D DPIV) can improve the accuracy of the in-plane motion. This is of course an advantage especially in the present experiment where there are large out-of-plane motions.

The fact that SPIV only provides measurement of all three velocity components within a plane implies that it has no advantage over 2D DPIV in giving additional vorticity components. Only in-plane velocity gradients are available from the measured velocity field. Consequently, the only vorticity component that can be calculated from the measured field is the out-of-plane component. While obtaining the other two

vorticity components is certainly desirable, having only one vorticity component is not a drawback since the out-of-plane vorticity is the main vorticity component in the problem currently studied.

2.4 Implementation

2.4.1 Planar DPIV

The implementation of planar DPIV in this experiment is very similar to that described in Vogt et al. (1996). The light sheet is aligned perpendicular to the freestream direction. The only modification is the placement of the recording camera. Instead of mounting the camera inside the tunnel with the optical axis perpendicular to the light sheet, the camera is placed outside the test section wall of the wind tunnel. The light, scattered by the seeding particles, is directed into the camera by a small 45-degree mirror placed inside the wind tunnel. The mirror is mounted far enough downstream from the measurement plane to reduce the effect of flow disturbance due to its presence. A more detailed description of the planar DPIV setup is given in Chapter 3.

The placement of the small mirror instead of the camera inside the wind tunnel reduces the interference. Also, this arrangement prevents the contamination of the CCD chip by the smoke particles.

2.4.2 SPIV

Stereoscopic PIV was used in this experiment to measure velocity fields behind the wing model. The implementation of this method in the present experiment is

described in this subsection. A more detailed description of SPIV can be found in Raffel, Willert and Kompenhans (1998).

In SPIV, stereoscopic recording is achieved by the use of a second camera, which records images of particles in the region of interest from a different viewing axis. The measurement precision of the out-of-plane component increases as the opening angle between the two cameras reaches 90 degrees (Raffel, Willert and Kompenhans, 1998). There are two basic stereoscopic imaging configurations available: a lens translation method and an angular lens displacement method. The latter was chosen in this experiment since it is more robust than the former.

In the angular lens configuration, the lens principal axis is aligned with the principal viewing direction. However, with this approach, it is impossible to get focused across the entire field of view since the object plane is no longer perpendicular to the axis of the lens. This problem can be overcome by tilting the CCD plane according to the Scheimpflug criterion. The Scheimpflug criterion says essentially that the object, lens, and image plane of each camera intersect at a common line.

In the present experiment, the Scheimpflug condition is accomplished with the help of Scheimpflug adaptors. Figure 2.1 shows the photograph of one of the Scheimpflug adaptors used in the experiment. As shown in Figure 2.1, the lens is fixed at some distance from the camera head. The camera is mounted on an aluminum box that can be rotated with respect to the lens. The procedure of focusing the cameras according to the Scheimpflug condition is as follows. First, each adaptor is aligned to the measurement region so that both systems are imaging exactly the same region of interest. Next, the center of the image of each camera is focused. Then, the camera head of each

camera is tilted until the whole field of view is focused. After completing the last step, the viewing direction of each camera has changed slightly. Therefore, it is necessary to re-align the lens and repeat the whole procedure until both cameras image the same measurement area with focus across the entire field of view. This iterative process can be quite time-consuming.

The process of tilting the CCD plane with respect to the lens plane introduces another problem. By tilting the camera head, the magnification factor is no longer constant across the entire field of view since, for each camera, one side of the object plane is closer to the principal axis of the lens than the other side of the object plane (see Figure 2.2). This results in a strong perspective distortion that requires an additional calibration.

To calibrate the cameras, a square calibration grid is placed inside the light sheet. The top part of Figure 2.3 shows a typical image of the grid from one of the cameras. As depicted in the figure, the horizontal lines, especially on the top and bottom part of the images, are highly distorted. Trapezoids are formed instead of rectangles due to this perspective distortion. "Dewarping" the original images from each of the camera so that the magnification factor remains constant over the entire image can solve this problem. The dewarping process consists of finding a mapping function for each of the cameras that maps the trapezoids into rectangles of the same size. The detailed steps are as follows:

1. Locating the grid intersections by cross-correlating the image with a + correlation mask. The peaks of the cross-correlation are identified as the location of the grid intersections.

2. Selecting an origin that is a common point in images from both cameras.
3. Setting the spacing between the grid lines and reconstructing a rectangular grid.
4. Finding the mapping function, for each camera, which maps the original image to that of the reconstructed rectangular grid.
5. Applying the mapping to each particle image obtained by the corresponding cameras.

The bottom part of Figure 2.3 shows the image of the grid after applying the mapping to the original image (upper part of 2.3). It is clearly shown that the "trapezoids" have been transformed into "rectangles". Note that some portions of the image on the upper and lower edges are lost in the transformation process.

Once the original images are dewarped, image pairs from each of the cameras separately undergo standard DPIV image interrogation schemes to obtain two projected, planar displacement fields.

The three-dimensional displacement field is reconstructed from the two planar displacements fields. Figure 2.4 shows the general geometric description used for the reconstruction. In a coordinate system center at the origin (point O), camera 1 and camera 2 are located at points (x_1, y_1, z_1) and (x_2, y_2, z_2), respectively. Consider point Q, somewhere in the object plane, where the displacement vector is to be determined. Angle α_1 is defined to be the angle between the viewing direction of camera 1 and the z direction in the XZ plane while β_1 is that in the YZ plane. Similar definitions can be made for camera 2. The measured projected planar displacement components, as described previously, are (dx_1, dy_1) and (dx_2, dy_2) for camera 1 and 2, respectively.

From the schematics shown on the lower part of Figure 2.4, it is easy to see that the three displacements can be reconstructed by using the following formulas (Willert 1997):

$$dx = \frac{dx_2 \tan\alpha_1 - dx_1 \tan\alpha_2}{\tan\alpha_1 - \tan\alpha_2} \tag{2-1}$$

$$dy = \frac{dy_2 \tan\beta_1 - dy_1 \tan\beta_2}{\tan\beta_1 - \tan\beta_2} \tag{2-2}$$

$$dz = \frac{dx_2 - dx_1}{\tan\alpha_1 - \tan\alpha_2}. \tag{2-3}$$

Using (2-3), the expression for *dy* can be rewritten:

$$dy = \frac{dy_1 + dy_2}{2} + \frac{dx_2 - dx_1}{2}\left(\frac{\tan\beta_2 - \tan\beta_1}{\tan\alpha_1 - \tan\alpha_2}\right). \tag{2-4}$$

Note that (2-4) can be used, instead of (2-2) in the case where β_1 and β_2 are very small, as in the present experiment.

The formulas for reconstructing the 3-component displacements from the planar fields given above assume that the angular difference along the vector ***dx***, the displacement vector, is negligible. Therefore, these formulas are good as long as the distance between the light sheet and each of the cameras is large, as is the case in this experiment.

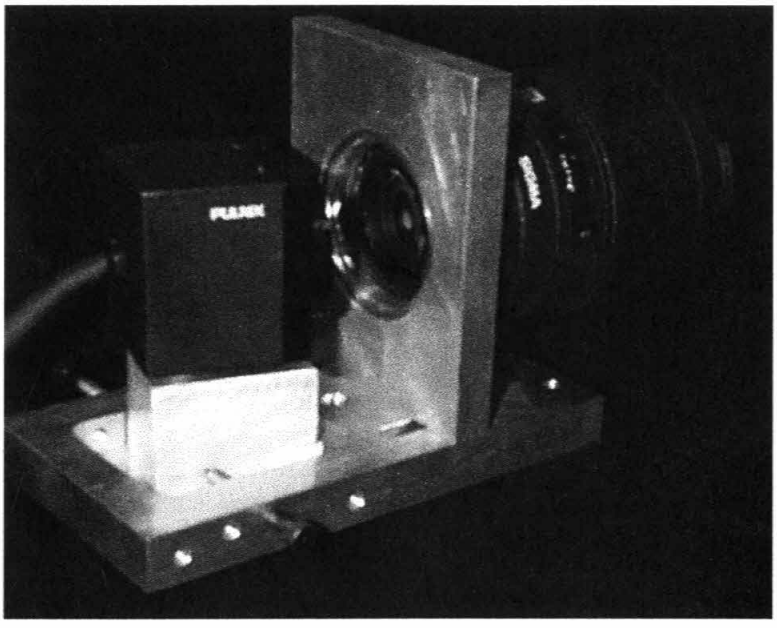

Figure 2.1. Photograph of Scheimpflug adaptor

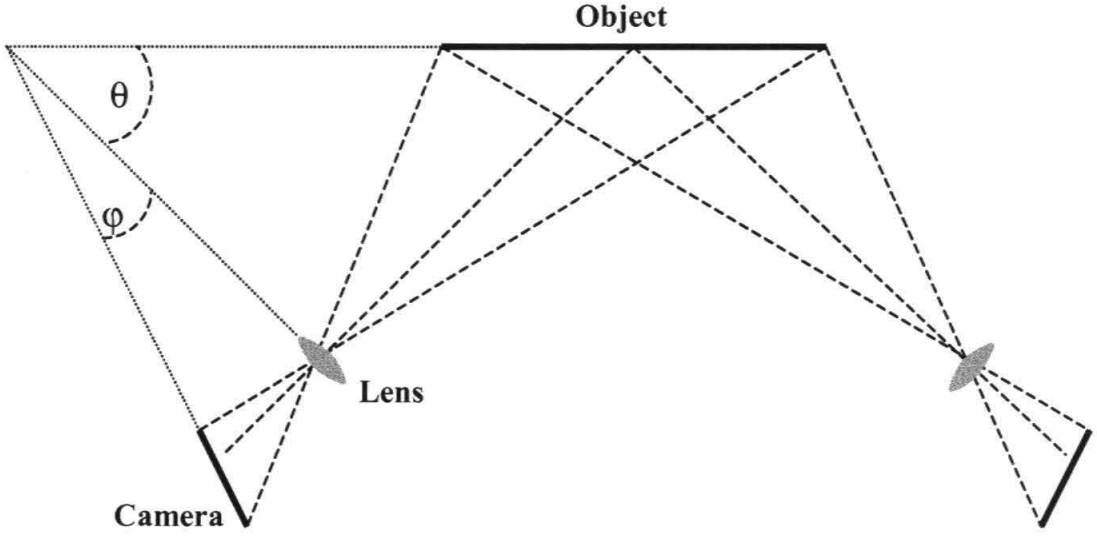

Figure 2.2. Angular lens configuration

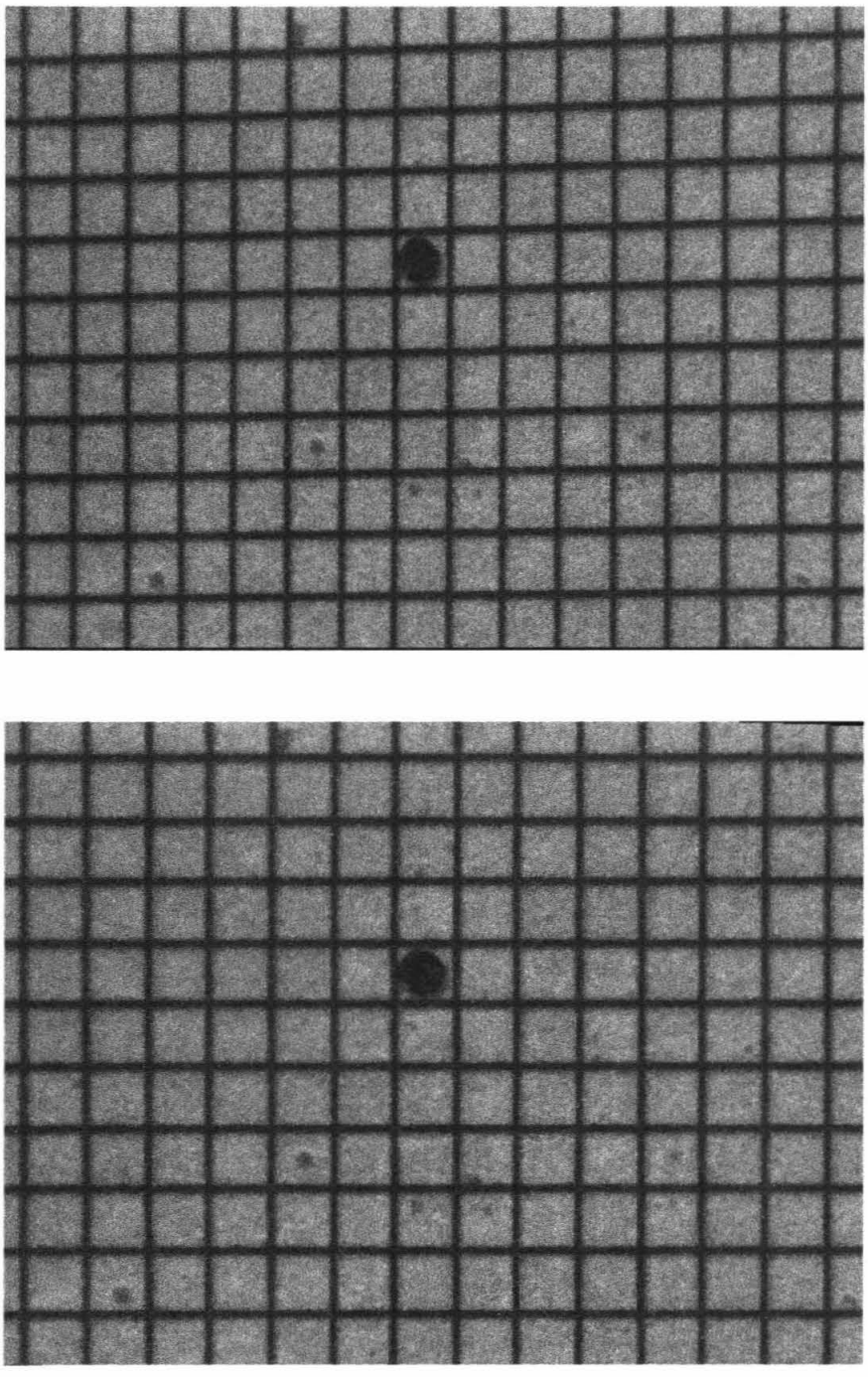

Figure 2.3. Calibration grid (upper: original, lower: after dewarped)

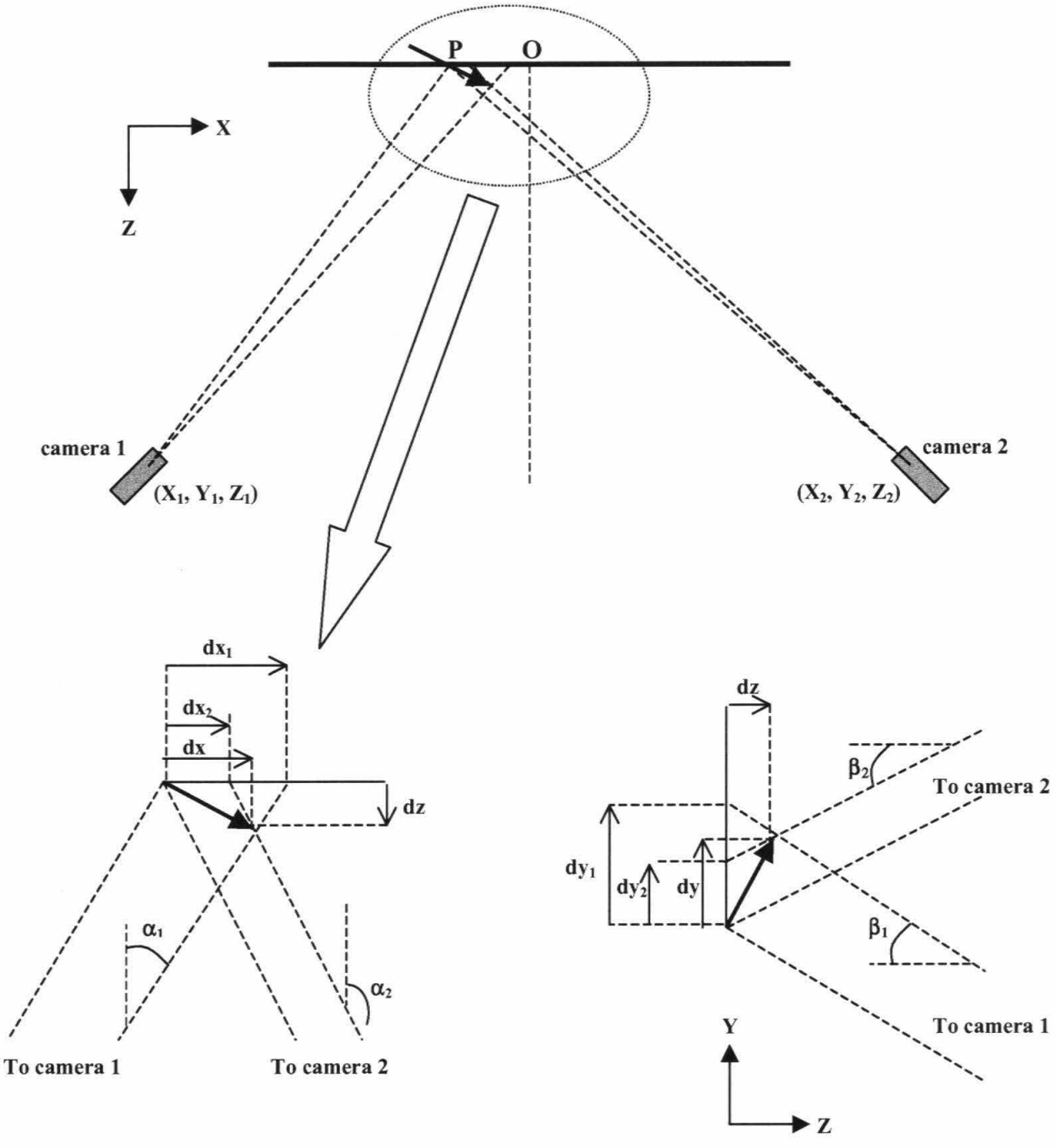

Figure 2.4. Schematic for the SPIV 3-component reconstructions

CHAPTER 3

Experimental Setup

3.1 Testing Facility

The experiments were conducted in the GALCIT 2-foot wind tunnel. The tunnel, which is a low-turbulence closed-loop wind tunnel, has a test section of two feet wide, two feet high, and seven feet long. The sidewalls and the ceiling of the tunnel are made of 1.8 cm thick clear Plexiglas. The floor is made of plywood. The tunnel can be operated up to a maximum speed of 50 m/s.

3.2 The Wing Model

The wing model has an NACA 0012 profile with an effective span of 41.91 cm and a chord length of 9.1 cm. The tip of the wing model is rectangular.

The wing is made from composite material. However, the composite material resulted in unwanted reflections of the light sheet when taking measurements close to or around the surface of the wing. Painting the wing with ultra flat black color reduced the unwanted reflections allowing measurements to be made in the region very close to the wing. However, light still scattered from the tip surface when the light sheet impinged on it, which prevented the taking of PIV data in the region around the tip of the wing. This

problem is finally solved by putting an NACA 0012-shape mirror on the surface of the tip. The mirror reflects the light uniformly back up onto the light sheet, ultimately eliminating the unwanted reflections.

The wing is positioned vertically at 40 cm behind the front of the test section. It is mounted on a force balance that is located underneath the test section. The force balance is placed on a rotating table. The angle of attack of the wing is adjusted by turning a wheel on the rotating table. The mounting system is designed such that the wing would remain near the center of the test section regardless of the angle of attack. Figure 3.1 shows the photograph of the whole experimental setup.

3.3 SPIV Setup

A photograph of the SPIV setup can also be seen in Figure 3.1. The whole SPIV system is mounted on a frame which is connected to a railing system that is fixed to the floor of the room. The frame consists of two legs, one on each side of the tunnel, and two sets of beams that bridge the two legs. Each of the two cameras is installed on each of the two legs. As shown in the figure, the laser and the light sheet optics are mounted on the upper bridge. The light generated is deflected down into the tunnel so that it is aligned perpendicular to the flow direction.

The frame can be moved parallel to the tunnel to take data at different downstream stations. Notice that in this arrangement, the distance between the light sheet and the cameras is always fixed. Therefore, cameras, as described in the last chapter, only need to be calibrated once. In other words, there is no need to do a re-

calibration when the light sheet is moved to a different downstream station since the light sheet and the cameras move together.

3.3.1 Light Sheet

The light source for the light sheet is provided by a New Wave Research "Gemini PIV" 120 mj/pulse Nd:Yag laser. The laser system consists of two IR laser heads combined in a single package. Each is operated at 15 Hz with pulse duration of 10 ns, which matches the framing rate of the cameras.

Figure 3.2 shows the schematic of the light sheet optics. The optics consists of two spherical and two cylindrical lenses. This combination of lenses allows for the width and the thickness of the light sheet to be changed independently. The thickness of the light sheet is approximately constant across the field of view. After passing the light sheet optics, the light is deflected down perpendicularly using a 45-degree mirror.

In this experiment, the light sheet is aligned perpendicular to the direction of the free stream. In this arrangement, the out-of-plane particle loss can be significant. One method to reduce the loss is to reduce the time between the first and the second image recording. This, however, reduces the dynamic range in the measurement. The method used in this experiment to reduce the out-of-plane loss is to shift the light sheet slightly, in the downstream direction, between illumination pulses. Moreover, the light sheet is slightly thickened to accommodate strong out-of-plane gradients in the vortex core region.

3.3.2 Image Recording

The flow is imaged using two Pulnix TM-9701 CCD cameras (768x480 pixels). 105 mm focal-length lenses are mounted in front of the cameras on the Scheimpflug adaptors. The synchronization of the two cameras is achieved using an external master triggering device (Sigma Electronics CSG-4500) that sends a synchronization signal to the two cameras.

The output signal from one of the cameras is used to trigger the laser system through a timing box. The timing box in turn controls the flash lamp signal of the lasers. For all measurements in this experiment, the time delay between images in a pair is set at 650 μs.

The output signals from the cameras are recorded on a real-time digital recorder. The signals are digitized using a color analog-to-digital frame grabber (Coreco RGB-SE), which acquires images at resolution of 640x480 pixels. The digitized images are then downloaded to a hard disk and processed by SPIV software.

3.3.3 Seeding

Choosing proper tracer particles for PIV measurements in wind tunnel applications is a difficult task. Particles that are often used for wind tunnel measurements are not easy to handle. Liquid droplets tend to evaporate quickly and solid particles are difficult to disperse (Raffel et al., 1998). There is also concern about whether the particles scatter enough light.

The first tracer particles used in this experiment are generated by pressurizing olive oil. The particles are able to reflect enough light. However, as these particles are

much denser than air, they have low particle distributions inside the vortex core. The particle concentration was so low that a hole could be observed by the naked eye in the low-pressure region (vortex core).

The final choice for particle seeding was smoke generated by the CORONA COLT 4 smoke generator. The machine produces particles that range in size from 0.1μ to 0.5μ in diameter. This type of tracer particle is able to scatter enough light, which resolves the problem of low particle concentration in the vortex core.

3.4 Planar DPIV Setup

Planar DPIV is used in this experiment to take velocity measurements around the tip of the wing. Views of the cameras are partly blocked due to the presence of the wing. Therefore, SPIV, in the present setup, can only be used to take measurements in the region above the wing tip. (Again, the wing is mounted vertically so that above the wing tip means farther away from the wing in the spanwise direction.) It is possible to change the setup by moving the wing model farther downstream and arranging the camera differently. However, that requires changing the whole experimental setup. Alternatively, measurement can be made in this region easily by using planar DPIV, which only requires a slight change in the setup.

The light sheet optics and image recording equipment are exactly those used for SPIV. Here, only one of the cameras is needed. The camera is mounted outside the tunnel (mounted on the same frame discussed in 3.3) with the viewing axis perpendicular to the sidewall of the tunnel. A small mirror is mounted inside the tunnel to direct the light scattered by the seeding particles into the camera. As mentioned in Chapter 2, the

mirror is mounted far enough downstream to reduce the interference effect. The schematic of the planar DPIV setup is shown in Figure 3.3.

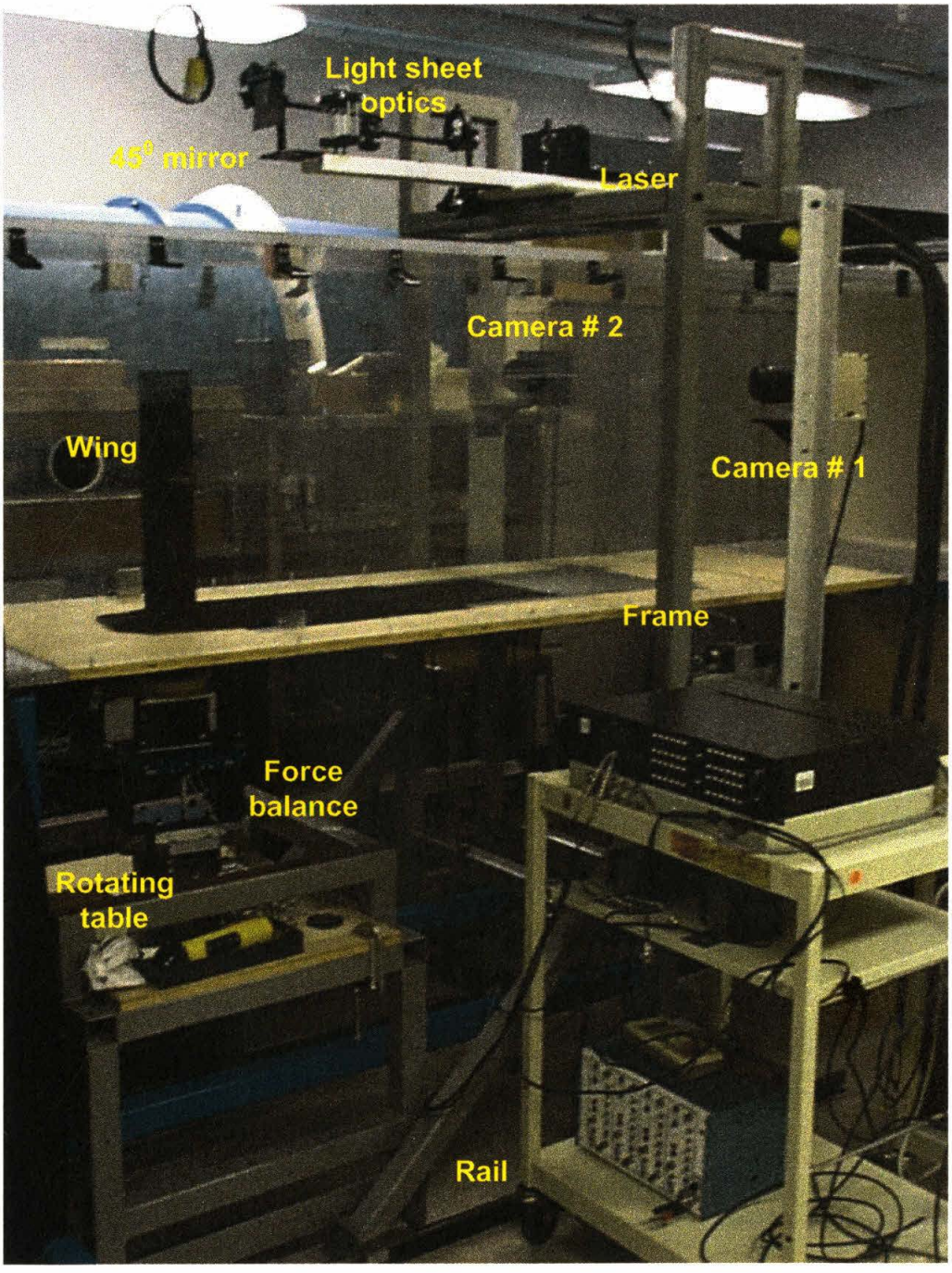

Figure 3.1. Photograph of the setup

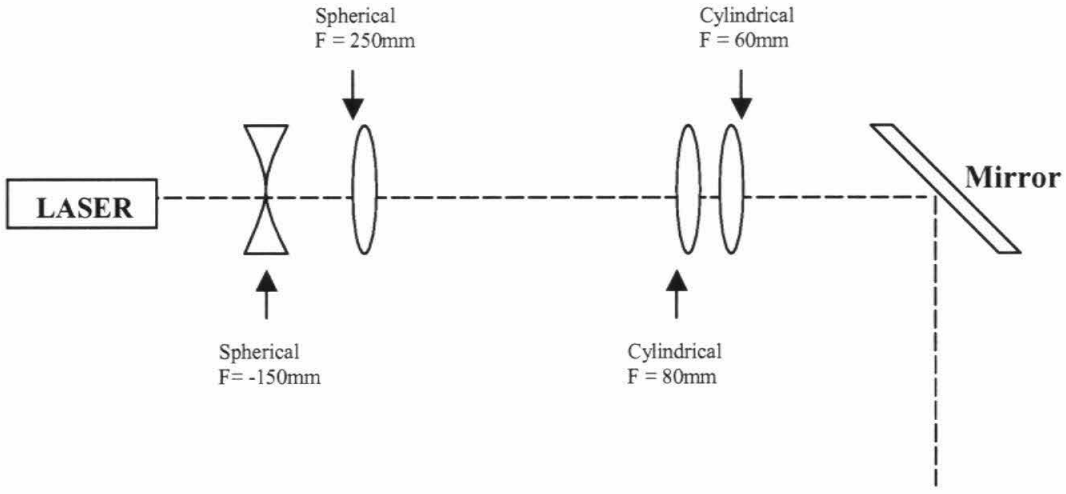

Figure 3.2. Light sheet optics (side view)

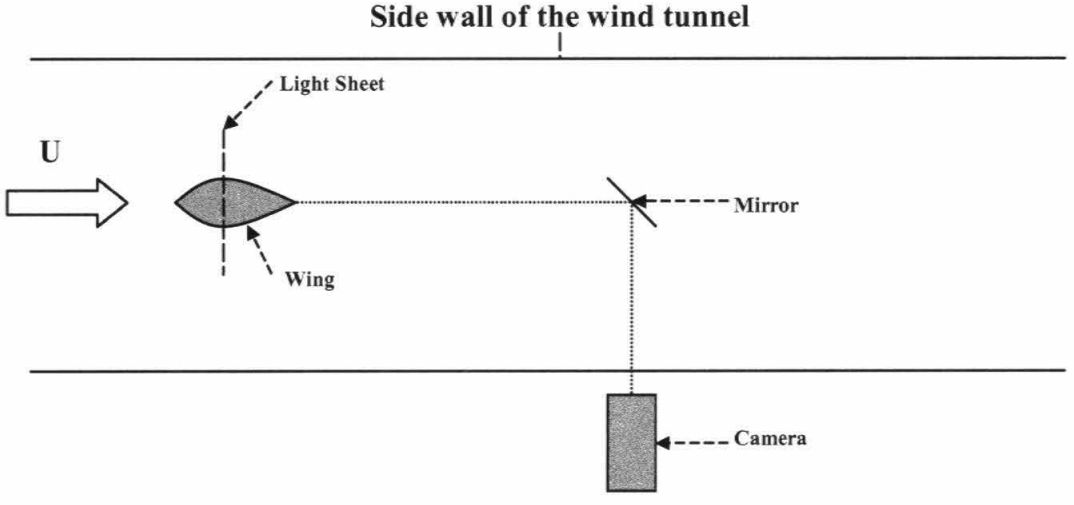

Figure 3.3. Schematic of planar DPIV setup (top view)

CHAPTER 4

3-Component Velocity Fields Behind the Wing

4.1 Introduction

In this chapter, we present the majority of PIV data obtained in the experiment. The experimental conditions are given in Section 4.2. This is followed by discussion about the methods of averaging used to obtain average velocity data. Lastly, the three-component planar velocity fields, measured by SPIV, are presented in Section 4.4. The results presented in this chapter will be discussed in detail in Chapters 5 and 6.

4.2 Experimental Conditions

The coordinate system used throughout the rest of this thesis is shown in Figure 4.1. The Z-axis is parallel to the freestream direction. The Y-axis is along the span and the X-axis forms a right-handed system with the Z and Y-axis. With this coordinate system, the measurement plane is in the X-Y plane. The area at which the measurements are made is also depicted in Figure 4.1.

For all data taken in this experiment, the freestream velocity of the wind tunnel is set at 1.5 m/s. This corresponds to a Reynolds number, based on the chord length of the wing model, of approximately 9040. Relatively low freestream velocity is chosen to

reduce the out-of-plane particle loss described in Chapter 3. There have been several attempts to increase the freestream velocity. The results are not very encouraging even with the combination of increased light sheet thickness and the light sheet stepping method described in the last chapter.

For SPIV measurements, data is taken at different angles of attack, ranging from 0^0 to 10^0 with 2^0 increments. For each angle of attack, measurements are made at different downstream stations, ranging from 0 to 5-chord lengths behind the wing.

For all measurements, 200 pairs of images are taken for a given angle of attack at a given streamwise location. This corresponds to 200 instantaneous velocity fields for each case. Figure 4.2 shows the plot of the number of instantaneous velocity fields against the running average of the in-plane velocity components along with their rms fluctuations at a given point in the field (somewhere in the vortex core). It is clearly shown in the figure that the running averages of these quantities converge at "Number of fields" equals 200.

4.3 Averaging Methodology

Average quantities presented in subsequent chapters are calculated from ensemble average velocity fields. It is found that, in some cases, the location of the wing tip vortex fluctuates in space, a phenomena referred to as "vortex meandering". Because of the unsteadiness of the vortex location, the values of the average quantities depend on the way the averaging is done.

There are two methods used to compute the ensemble average of the velocity fields in the present study. The first one is simply to overlay each of the 200 velocity

fields and compute the ensemble average. The second one is to identify the center of the vortex in each instantaneous field, shift the individual field so that the vortex center is located at a common point, and then compute the average.

Near the trailing edge, the main vortices are approximately steady. In this region, the average velocity is calculated using the first method. It will be shown in the subsequent chapter that the wing tip vortex meanders in regions downstream of the wing. In these cases, the second method is employed to compute the average.

Figure 4.3 shows the profiles of azimuthal velocity, axial velocity, and vorticity along a cut through the center of the vortex. These profiles are taken from mean velocity fields calculated by the two methods discussed previously. The figure shows that, while in most regions the profiles are almost identical, the peak values of the profiles calculated by the second method are higher than those computed by the first method. The difference in the values of the peak vorticity, for example, is approximately 5%. Also, the peak value of the mean out-of-plane velocity computed by the first method is approximately 3% lower than that computed by the second method. This is due to the vortex unsteadiness that smears out the peak values when averaging is computed using the first method.

Although the differences in the peak values calculated by the two methods are relatively small for the example presented above, they are not always the case in general. The difference in peak values as high as 10% is observed in some of the data. In addition to the smearing out of the mean peak values, vortex meandering also generates fluctuations of velocities at a given point fixed in space. These fluctuations are sometimes mistakenly interpreted as turbulence by some researchers in the past. The use

of global instantaneous measurement technique in the present studies is clearly an advantage since it allows a definitive correction for the vortex meandering effect.

4.4 Stereoscopic DPIV Results

In this section, results from stereoscopic PIV measurements are presented. As a reminder, stereoscopic PIV is used, in the present experiment, to measure velocity fields downstream of the wing (0-5 chord-length behind the wing). Also, the wing is mounted along the Y-axis and the location of the tip, at a 0^0 angle of attack, is at coordinate point (41, 40.5), in all plots to follow. The unit for distance and velocity is mm and mm/s, respectively.

Figure 4.4 presents a typical three-component planar velocity field in three-dimensional space measured at the trailing edge of the wing using stereoscopic PIV. For clarity of the velocity vectors within the vortex and its core, the freestream velocity is subtracted (the out-of-plane component of velocity in the figure is relative to the freestream). In the figure, both the colorbar legend and the size of the arrows indicate the magnitude of the velocity vectors. Besides the obvious in-plane motion, this figure depicts the presence of axial velocity in the vortex core and wake region. In this frame of reference, the axial velocity vectors are directed toward the wing, indicating that the out-of-plane velocities within the vortex are lower than the freestream velocity.

Figure 4.4 is displayed for presentation purposes only. It is difficult to obtain the detailed information provided by the measured velocity field if it is displayed as in Figure 4.4. For that reason, the measured three-component velocity fields are presented

differently in the rest of this section. For each case, the in-plane motion is presented in the vector field format while the out-of-plane component is displayed as a contour plot.

For each case (given angle of attack, at a given streamwise location), both the average and one instantaneous field are presented. Again, the average is computed from 200 instantaneous fields, using methods described in Section 4.3 (the first method for fields measured at 0 chord length and the second method for fields measured at 1-5 chord length downstream of the wing).

All velocities are given with respect to a lab-fixed coordinate system. The colorbar legend for the in-plane vector field is the magnitude of the total velocity (all three components). This also means that the color bar legend for the vector field is proportional to the pressure difference (P_{tot}-P). The color bar legend for the contour plot, however, is with respect to the out-of-plane velocity magnitude only.

Note that the light sheet is always normal to the freestream velocity direction, not normal to the wing tip vortex itself. Therefore, the measured velocity components are the projections into this plane. This is important to note especially for high angle of attack data taken in regions close to the wing where the normal direction of the vortex is not exactly parallel to the Z-axis.

In this section, we present only the results of the measurements for $\alpha = 0^0$, $\alpha = 2^0$, and $\alpha = 10^0$ case. The last two cases represent the low ($\alpha = 2^0$ and $\alpha = 4^0$) and high ($\alpha = 6^0$ to $\alpha = 10^0$) angles of attack, respectively. Discussion about the results and possible explanation for the phenomena observed are given in the later chapters.

4.4.1 Z/C = 0

In this subsection, we present velocity measurements taken at the trailing edge of the wing (Z/C = 0). The velocity fields, taken at this streamwise station, are shown in Figure 4.5 to Figure 4.7 (the plots are arranged in order of increasing angle of attack).

Both instantaneous and average in-plane velocity components for $\alpha = 0^0$ case (left-hand side of Figure 4.5) show vectors, in the region near the wing, pointing toward the root of the wing (inboard). At $\alpha = 0^0$, the flow behind the wing is just the wake flow behind a slender body, as clearly depicted in the plots. At a very low angle of attack ($\alpha = 2^0$), the initiation of the tip vortex is clearly visible (see Figure 4.6). The directions of in-plane velocity vectors on the high-pressure side are split. Near the tip, the vectors are directed outboard circling the tip while vectors slightly inboard are still pointing toward the root, as in the $\alpha = 0^0$ case. As expected, the tip vortex gets stronger as the angle of attack is increased to a higher value (Figure 4.7, for $\alpha = 10^0$ case). Here, the pressure side in-plane motion is directed toward the outboard part of the wing across the entire field of view. For all α, vectors in the suction side are directed toward the root. The presence of a shear layer at the trailing edge of the wing is evident in all in-plane vector fields presented in this subsection.

Contours of average and instantaneous out-of-plane velocity components are shown on the right-hand side of Figure 4.5 to Figure 4.7. Areas of very low out-of-plane velocity are apparent in the wake region for $\alpha = 0^0$ case (Figure 4.5). The out-of-plane velocity increases in all directions away from the wake and approaches the freestream velocity in the region far from the wing. At $\alpha = 2^0$ (Figure 4.6), areas of very low axial velocity are observed in the vicinity of the vortex core and shear layer. This region of

low velocity continues to increase as α is increased further (as depicted in Figure 4.7). However, the magnitude of the out-of-plane velocity is slightly higher (closer to freestream value) than in the lower angle of attack case. This is understandable since at a higher angle of attack the out-of-plane direction (Z-axis) is no longer parallel to the normal plane of the vortex, especially in a streamwise location that is very close to the wing. The values, shown in the figure, are actually the projection of the "axial" velocity component into the Z-axis.

4.4.2. Z/C = 1

Examples of instantaneous and average velocity fields at a streamwise location of 1 chord length behind the wing are presented in Figure 4.8 and Figure 4.9.

The in-plane velocity fields for $\alpha = 2^0$ case at this station (Figure 4.8) resemble that taken at Z/C = 0. Here, the size of the wing tip vortex has clearly increased to a larger size. The wake of the wing is still visible in the $\alpha = 2^0$ case. This is a strong indication that the rollup process has not been completed. At a higher angle of attack (Figure 4.9, for $\alpha = 10^0$), the in-plane vector fields in the vortex region look qualitatively the same as in the lower α case. However, in this case, the wake of the wing is no longer noticeable.

The contour of the out-of-plane velocity components for $\alpha = 2^0$ case shows two separate regions of low axial velocity (core and wake region). The peak magnitudes of these low out-of-plane velocities are, however, higher than that measured at Z/C = 0. Contours for a higher angle of attack case, $\alpha = 10^0$, look slightly different from the

contour for $\alpha = 2^0$ case. In the former cases, the out-of-plane velocity fields have lower magnitude in the regions that resemble an ellipse. However, the corresponding in-plane vector fields for such cases do not give any indication that the tip vortex is of an elliptical shape.

4.4.3 Z/C = 2

The velocity fields for the $\alpha = 2^0$ case, at a streamwise station of 2-chord length behind the wing, are shown in Figure 4.10. The out-of-plane velocity contours for the $\alpha = 2^0$ case are now qualitatively similar to the higher angle of attack case (looks like an ellipse). Also, the out-of-plane velocities in the region near the vortex for all α is now closer to the freestream velocity compared to that presented in the previous sub-section.

The in-plane and out-of-plane velocity fields for $\alpha = 10^0$ case are shown in Figure 4.11. At this downstream station, the in-plane vector plots and out-of-plane contour plots for $\alpha = 10^0$ case are qualitatively the same as those for the corresponding $\alpha = 10^0$ case, at Z/C = 1.

4.4.4 Z/C = 3

Typical average and instantaneous velocity fields measured at a streamwise station of 3-chord length behind the wing for the low and high angle of attack cases are shown in Figure 4.12 to Figure 4.13, respectively. These plots are arranged as in previous sub-sections. The plots, presented here, are qualitatively the same as in Z/C = 2 case.

4.4.5 Z/C = 4

Instantaneous and average velocity fields, for $\alpha = 2^0$ and 10^0 case at streamwise location of 4-chord length behind the wing, are presented in Figure 4.14 and Figure 4.15, respectively. Again, with the exception of the magnitude of the velocity components and the size of the vortex core, there seems to be no qualitative difference between this case and the case considered in Section 4.4.3.

4.4.6 Z/C = 5

The streamwise station of 5-chord length behind the model is the final streamwise station at which measurements are made. Examples of velocity fields obtained from measurements at this station are shown in Figure 4.16 and Figure 4.17, with the usual arrangement.

The in-plane velocity vector field for the $\alpha = 2^0$ (Figure 4.16) at this station still resembles that taken at earlier stations. The wake of the wing is still visible, within the field of view, although it is much shorter than before. (But the tip vortex also has moved downward, at this station, with respect to the field of view.) The in-plane velocity fields for a higher angle of attack ($\alpha = 10^0$) case still resemble the vector fields presented previously (see Figure 4.17).

At this downstream station, the shape of the out-of-plane velocity contour in the region around the tip vortex has become more circular for the lower angle of attack cases

($\alpha = 2^0$). On the other hand, the shape of the low velocity contour, in the vicinity of the tip vortex, is still of elliptical shape for the higher angle of attack case ($\alpha = 10^0$ case).

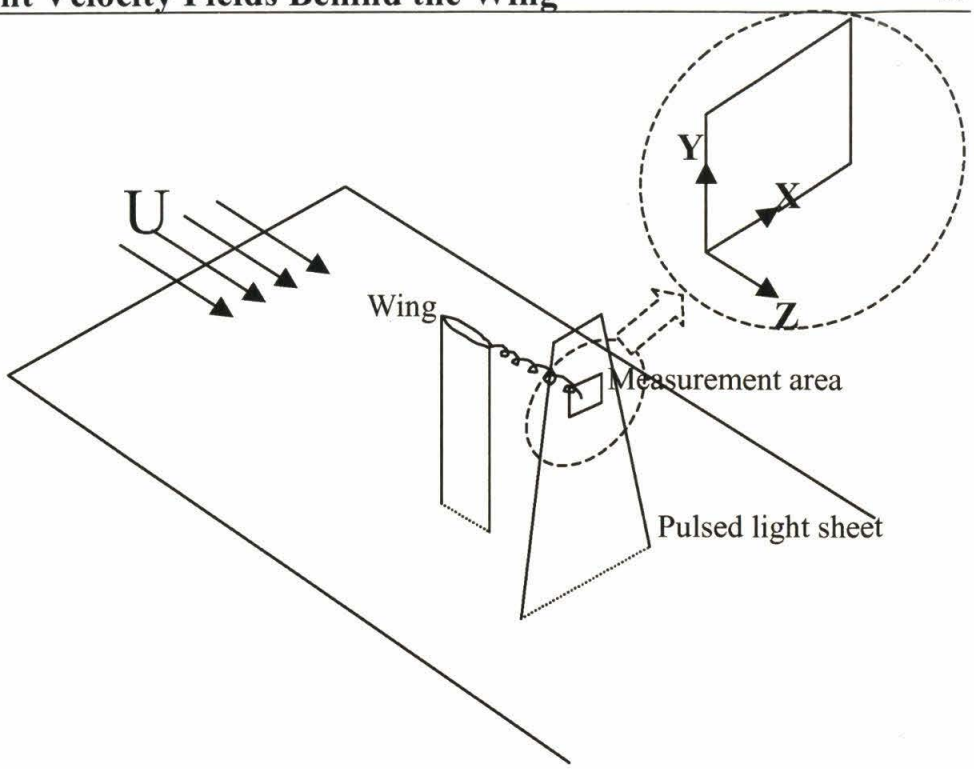

Figure 4.1. Schematic of the setup and the coordinate system

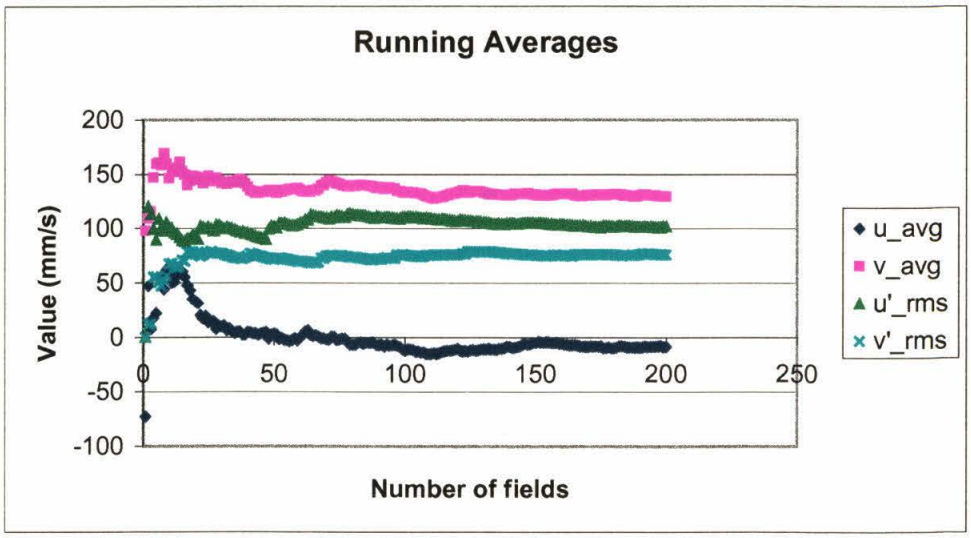

Figure 4.2. Running average vs. number of velocity fields

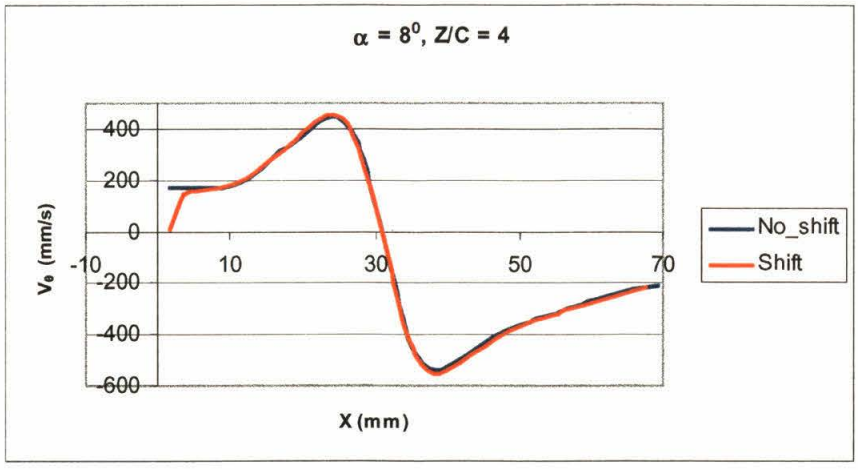

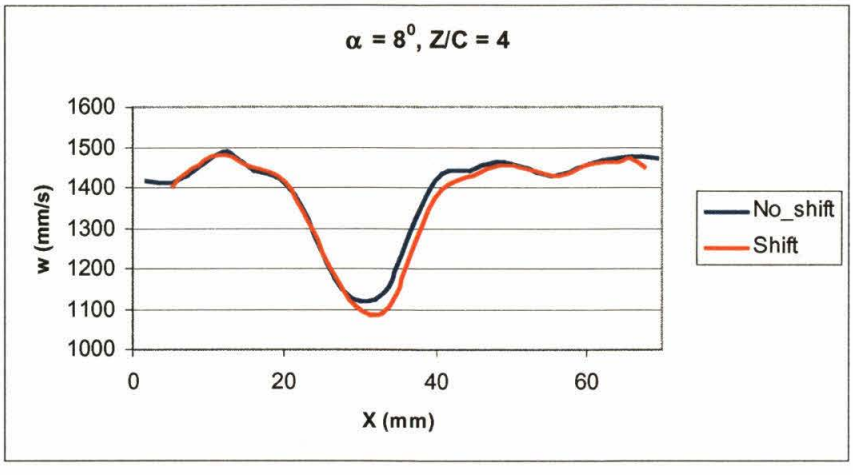

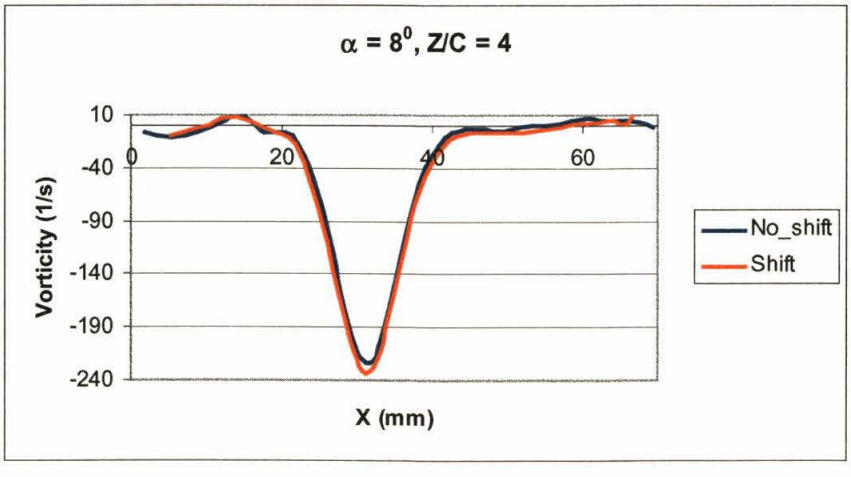

Figure 4.3. Average values computed with the two averaging methods

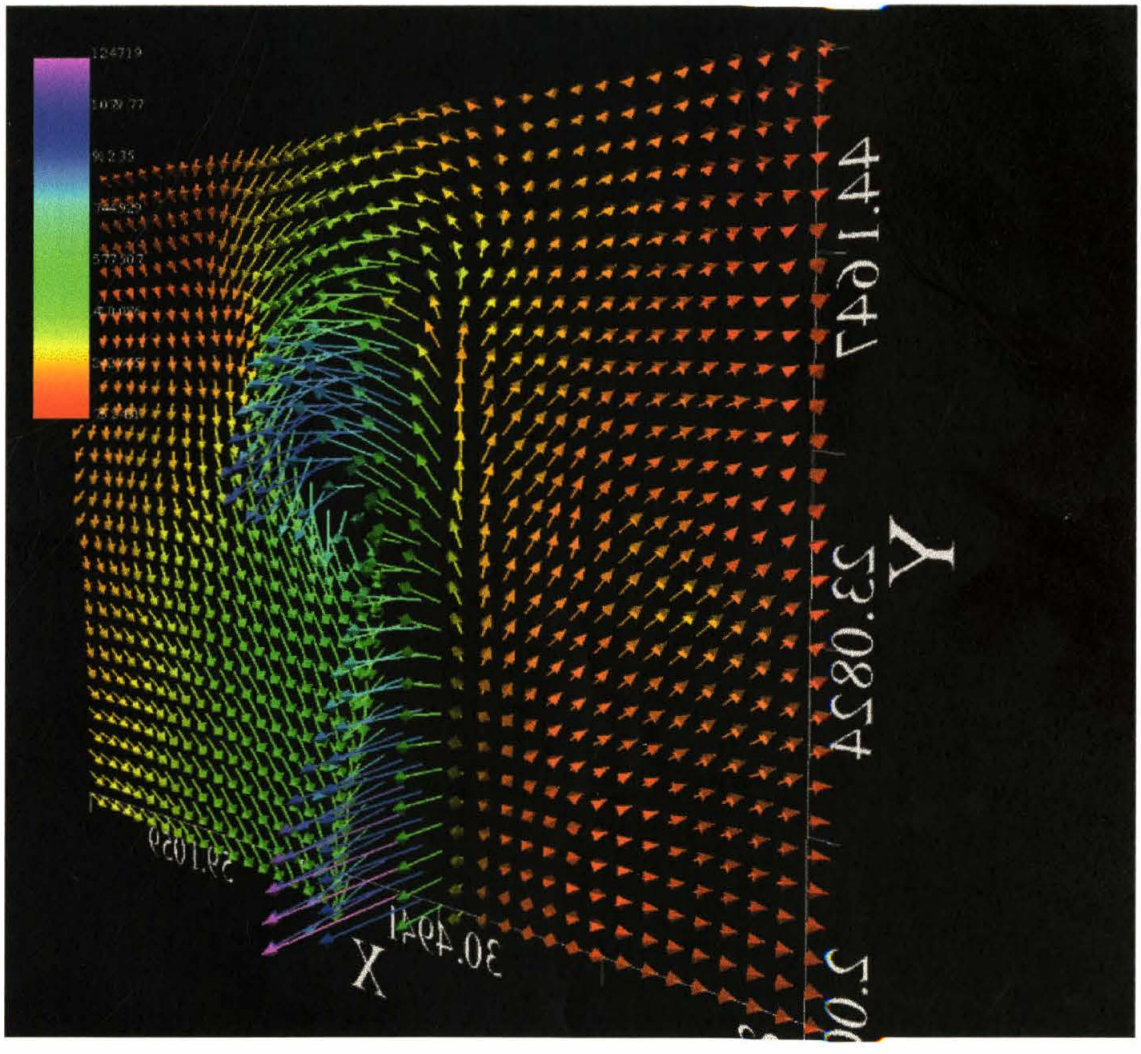

Figure 4.4. Three-component velocity field close to trailing edge of the wing

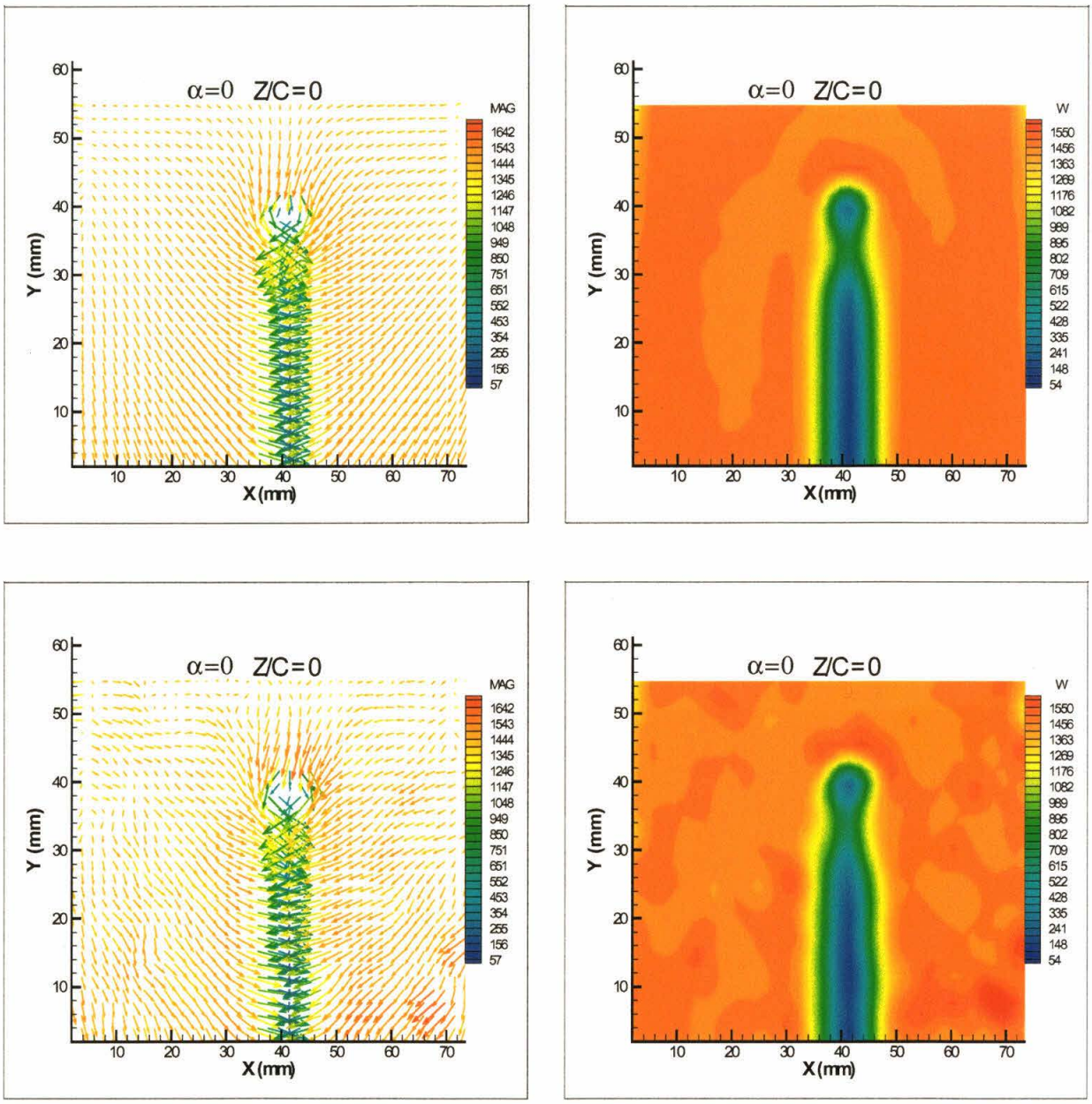

Figure 4.5. Velocity fields, z/c = 0, $\alpha = 0^0$ (upper: average, lower: instantaneous)

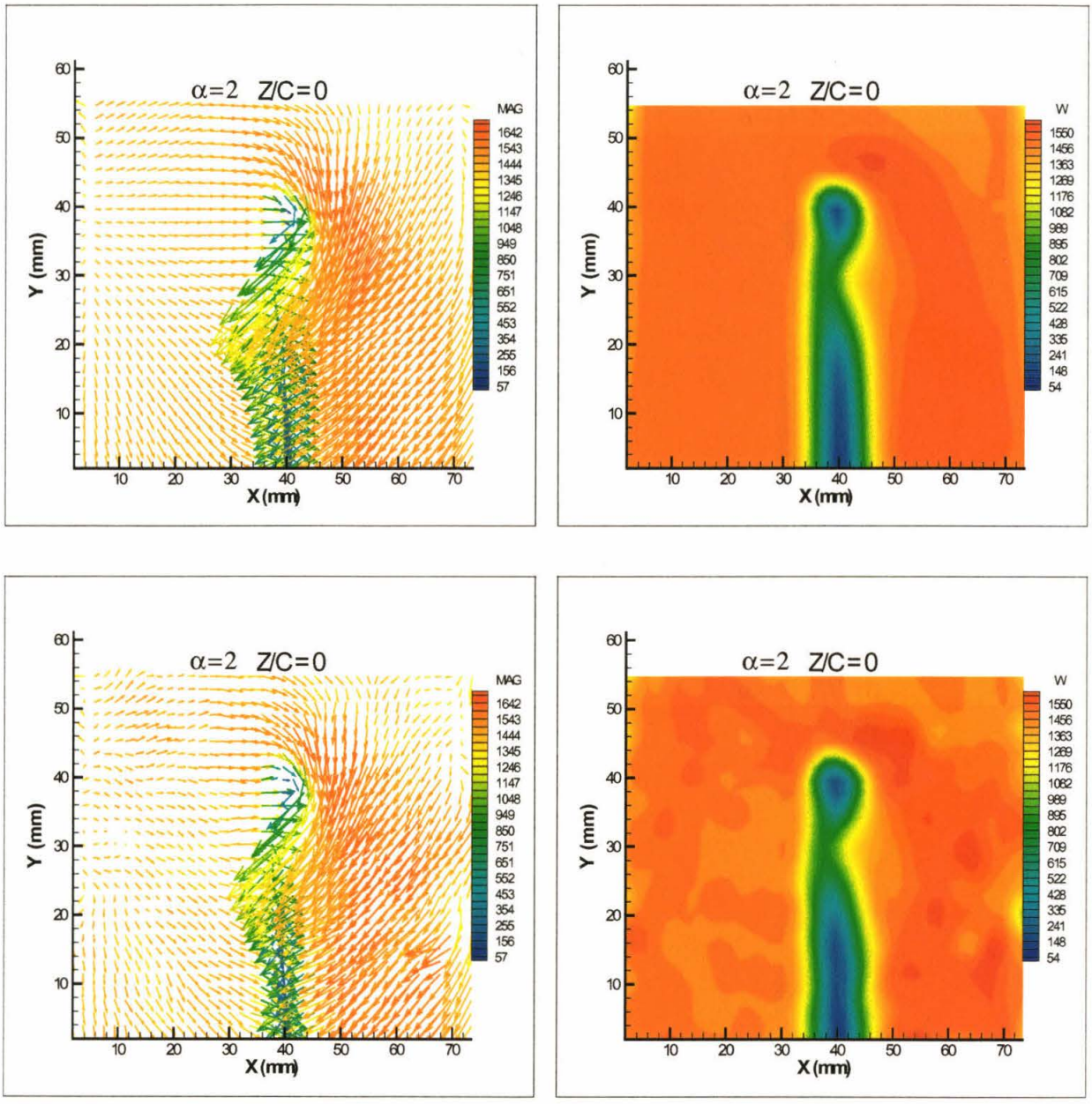

Figure 4.6. Velocity fields, z/c = 0, $\alpha = 2^0$ (upper: average, lower: instantaneous)

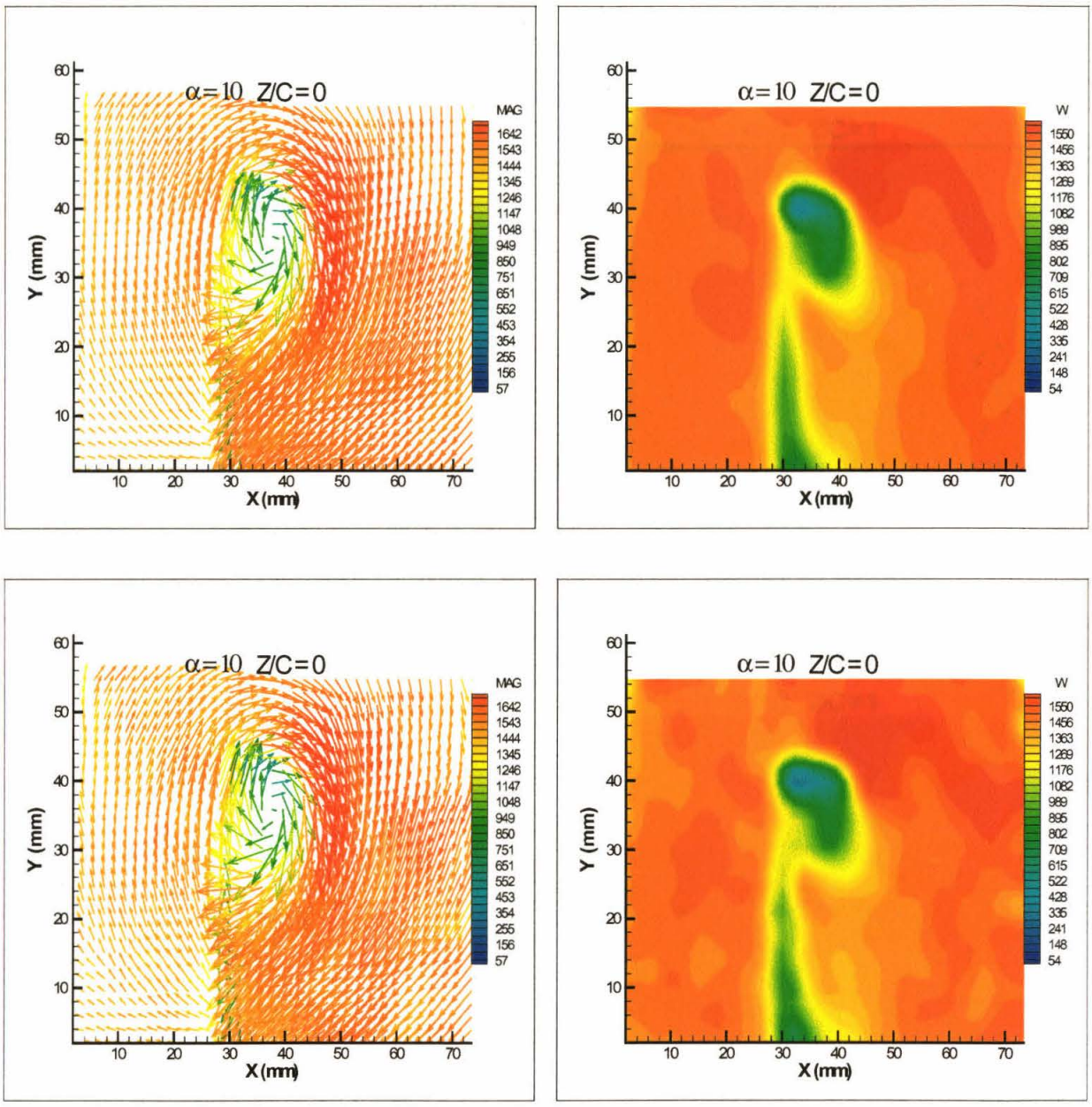

Figure 4.7. Velocity fields, z/c = 0, $\alpha = 10^0$ (upper: average, lower: instantaneous)

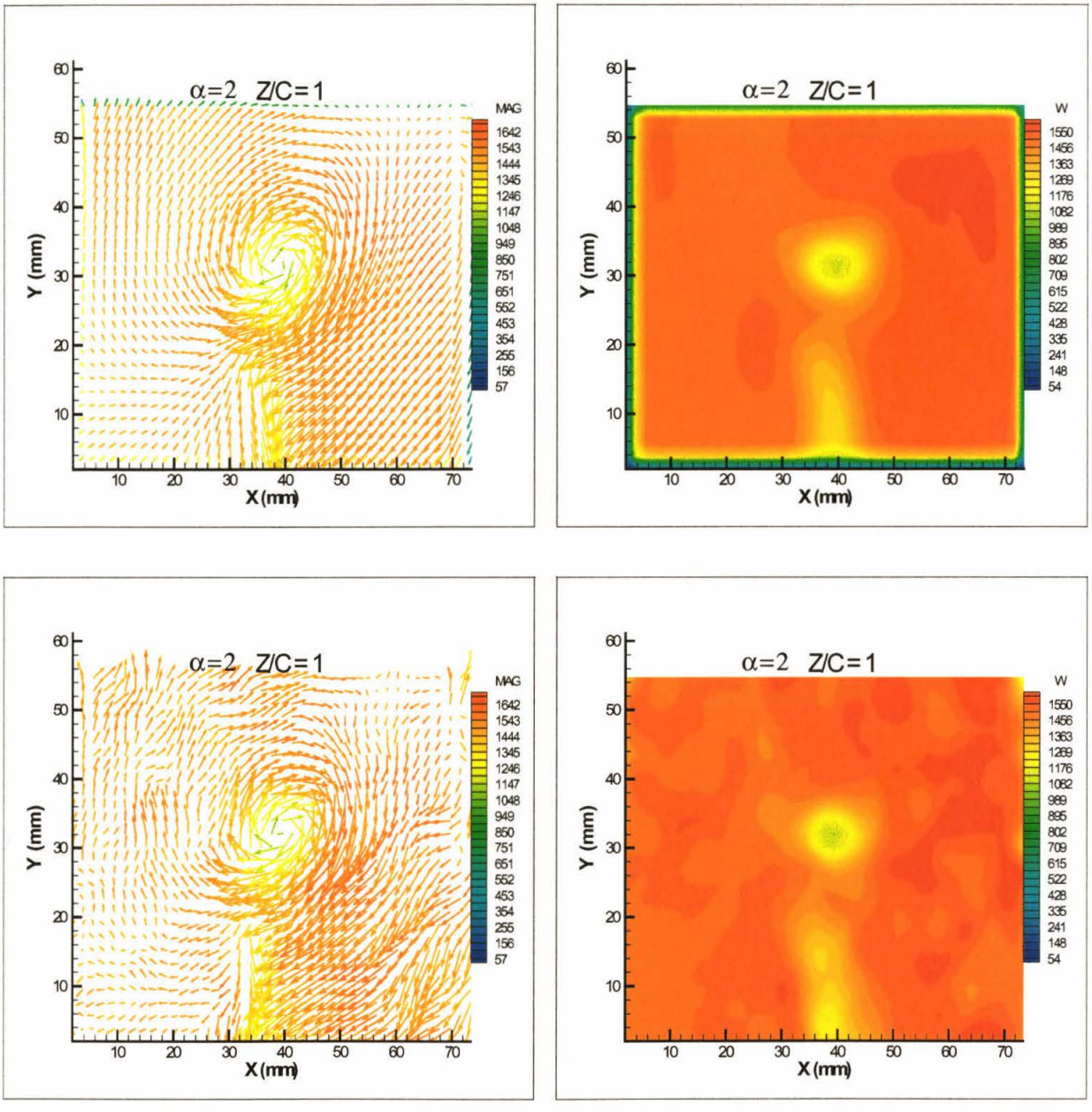

Figure 4.8. Velocity fields, z/c = 1, $\alpha = 2^0$ (upper: average, lower: instantaneous)

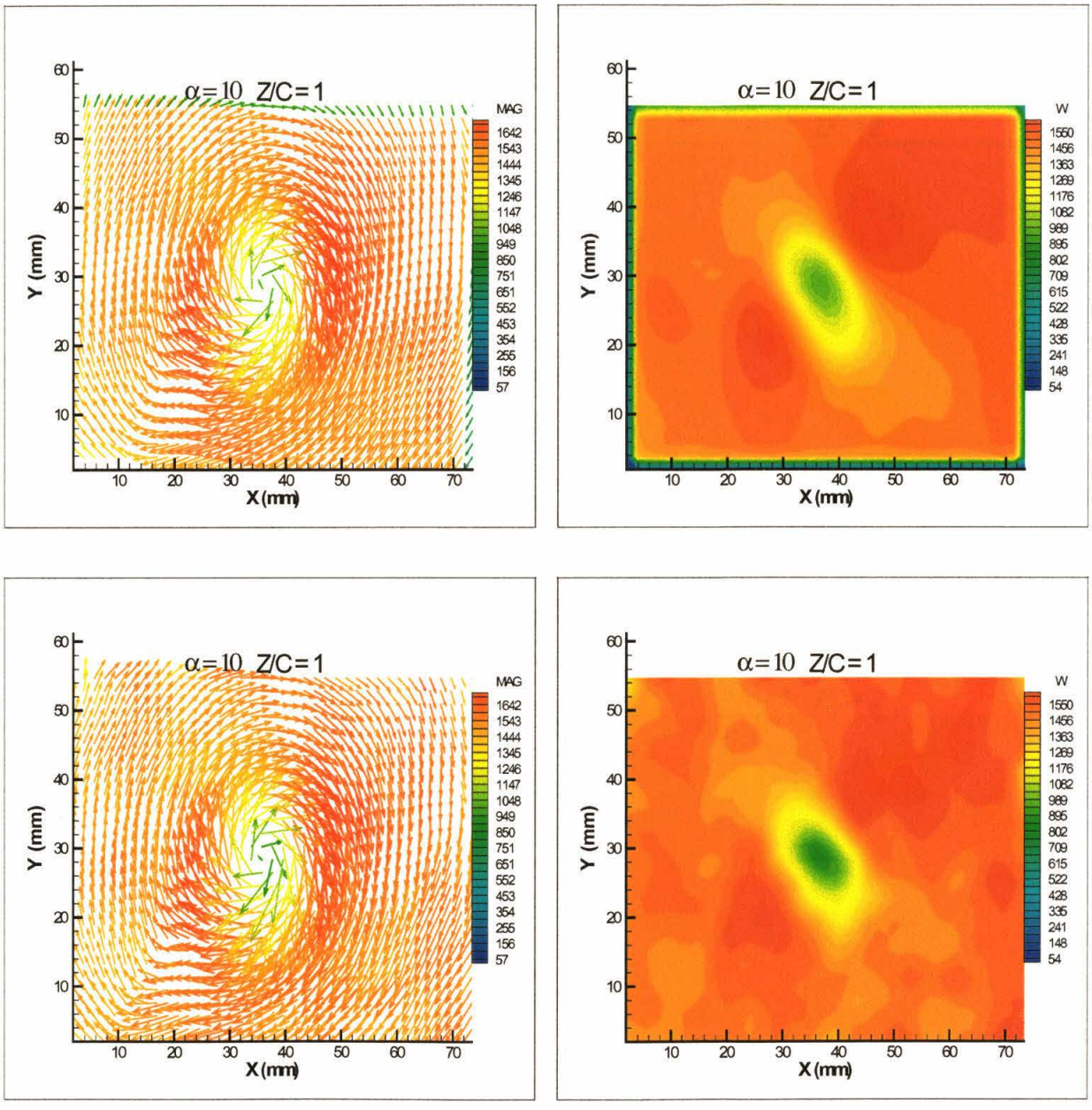

Figure 4.9. Velocity fields, z/c = 1, $\alpha = 10^0$ (upper: average, lower: instantaneous)

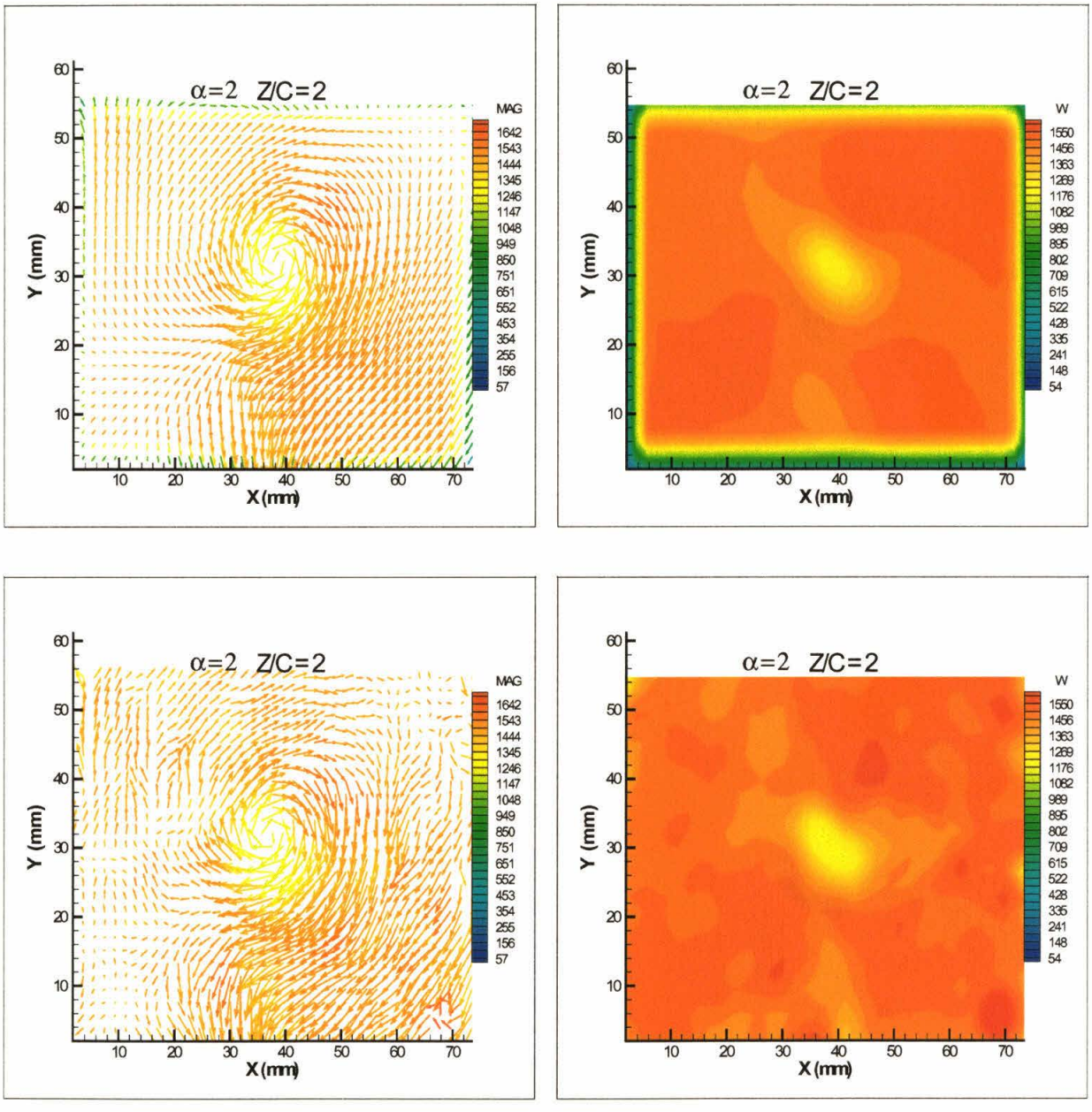

Figure 4.10. Velocity fields, z/c = 2, $\alpha = 2^0$ (upper: average, lower: instantaneous)

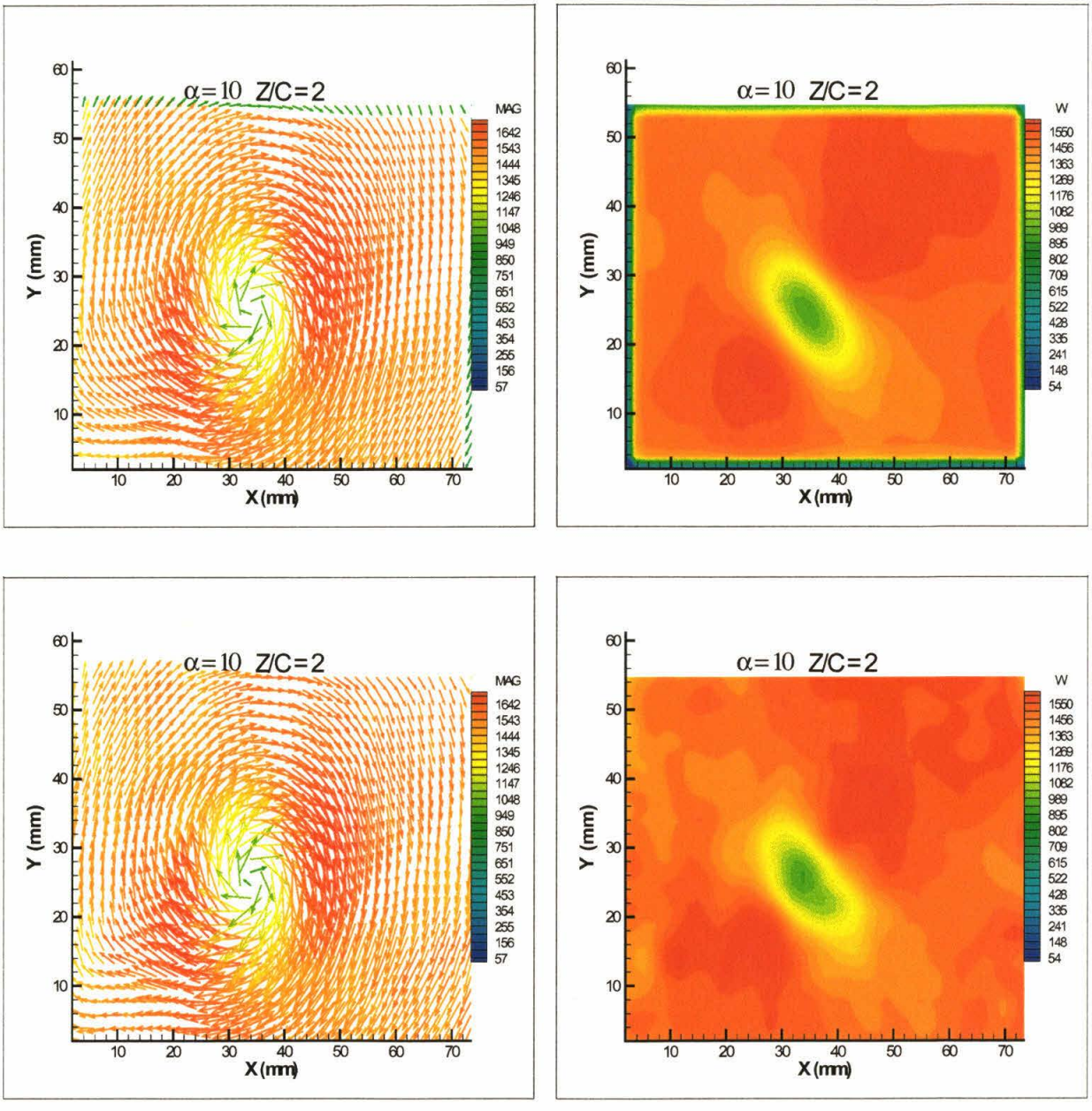

Figure 4.11. Velocity fields, z/c = 2, $\alpha = 10^0$ (upper: average, lower: instantaneous)

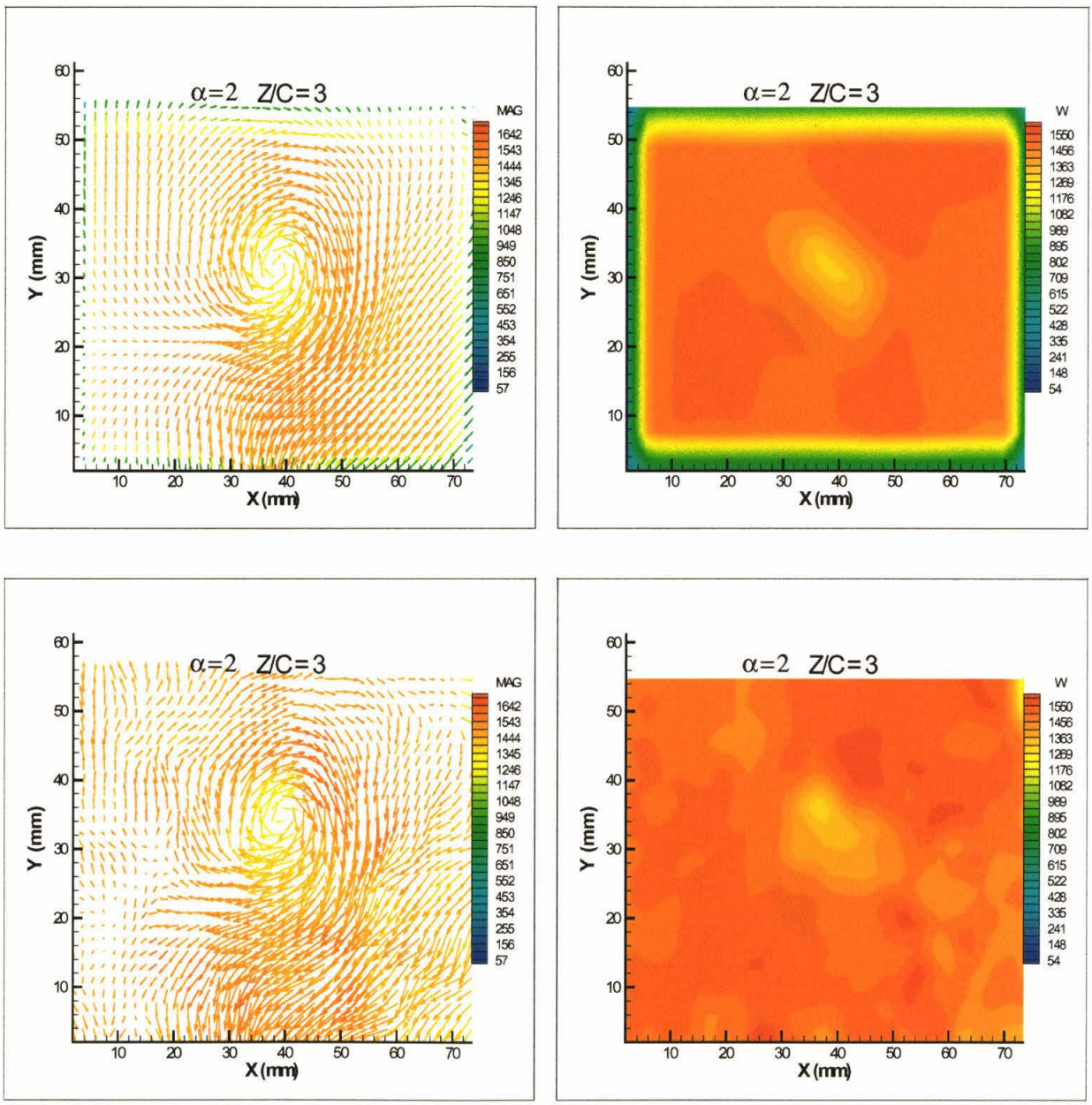

Figure 4.12. Velocity fields, z/c = 3, $\alpha = 2^0$ (upper: average, lower: instantaneous)

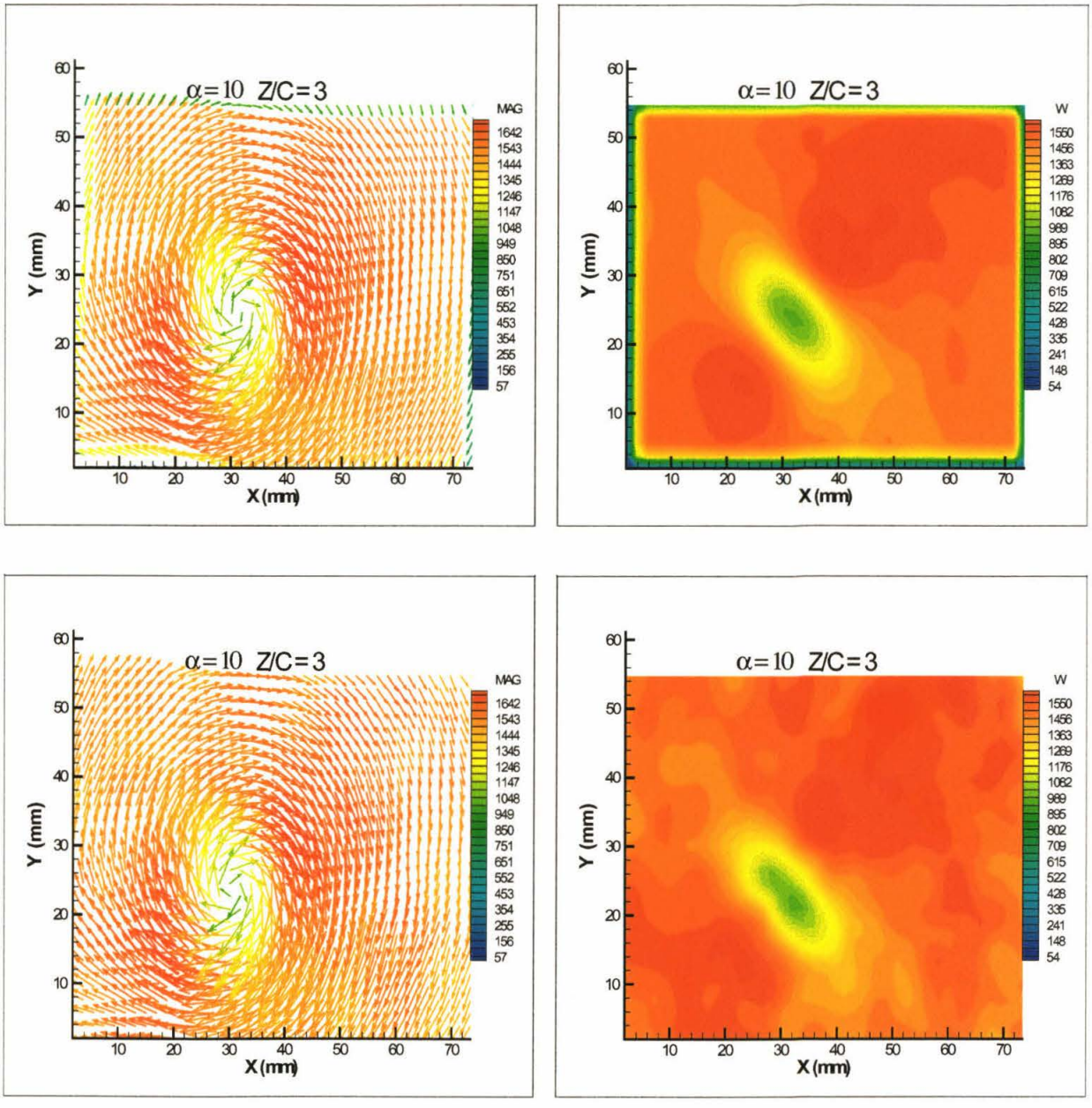

Figure 4.13. Velocity fields, z/c = 3, $\alpha = 10^0$ (upper: average, lower: instantaneous)

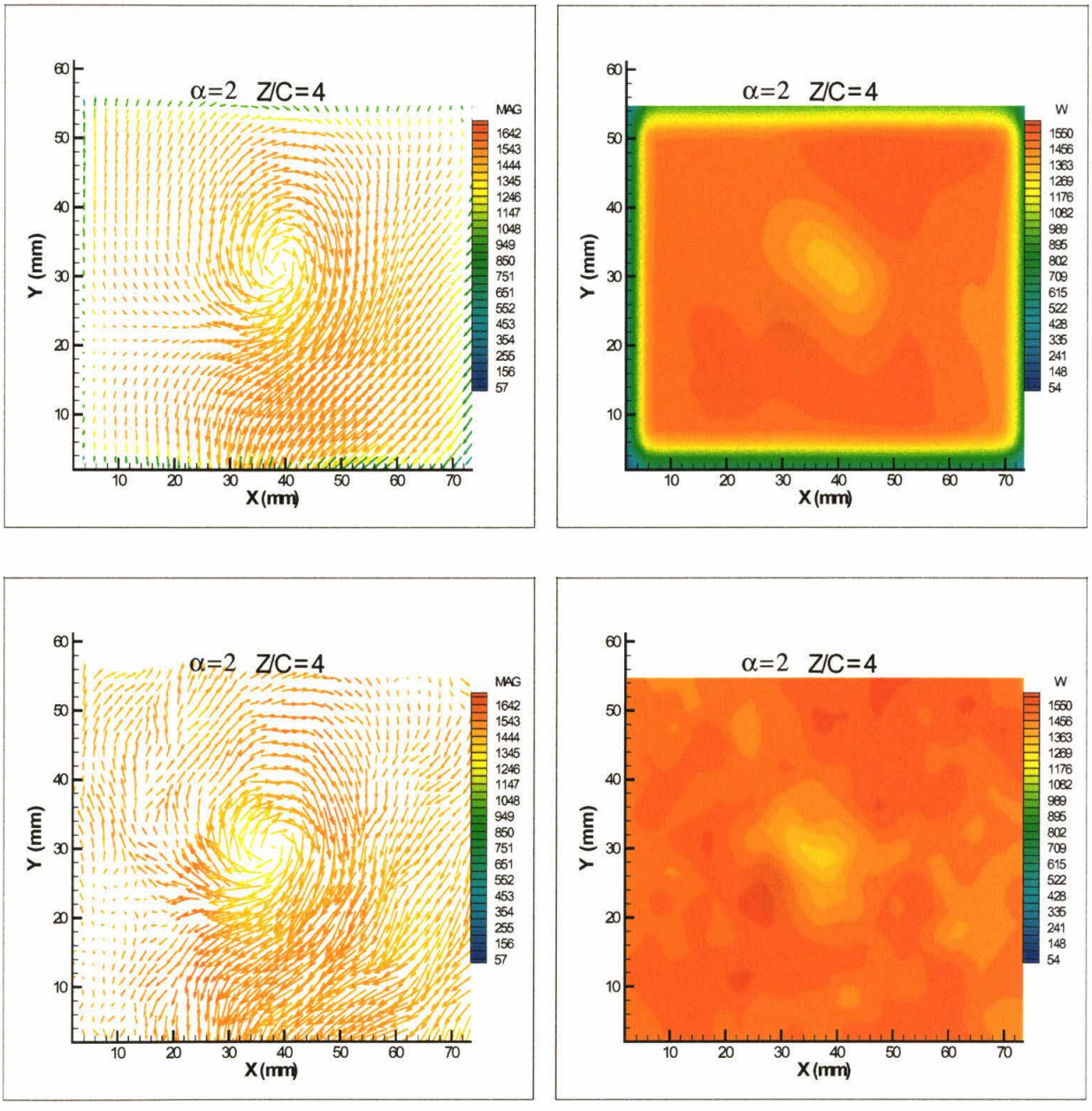

Figure 4.14. Velocity fields, z/c = 4, $\alpha = 2^0$ (upper: average, lower: instantaneous)

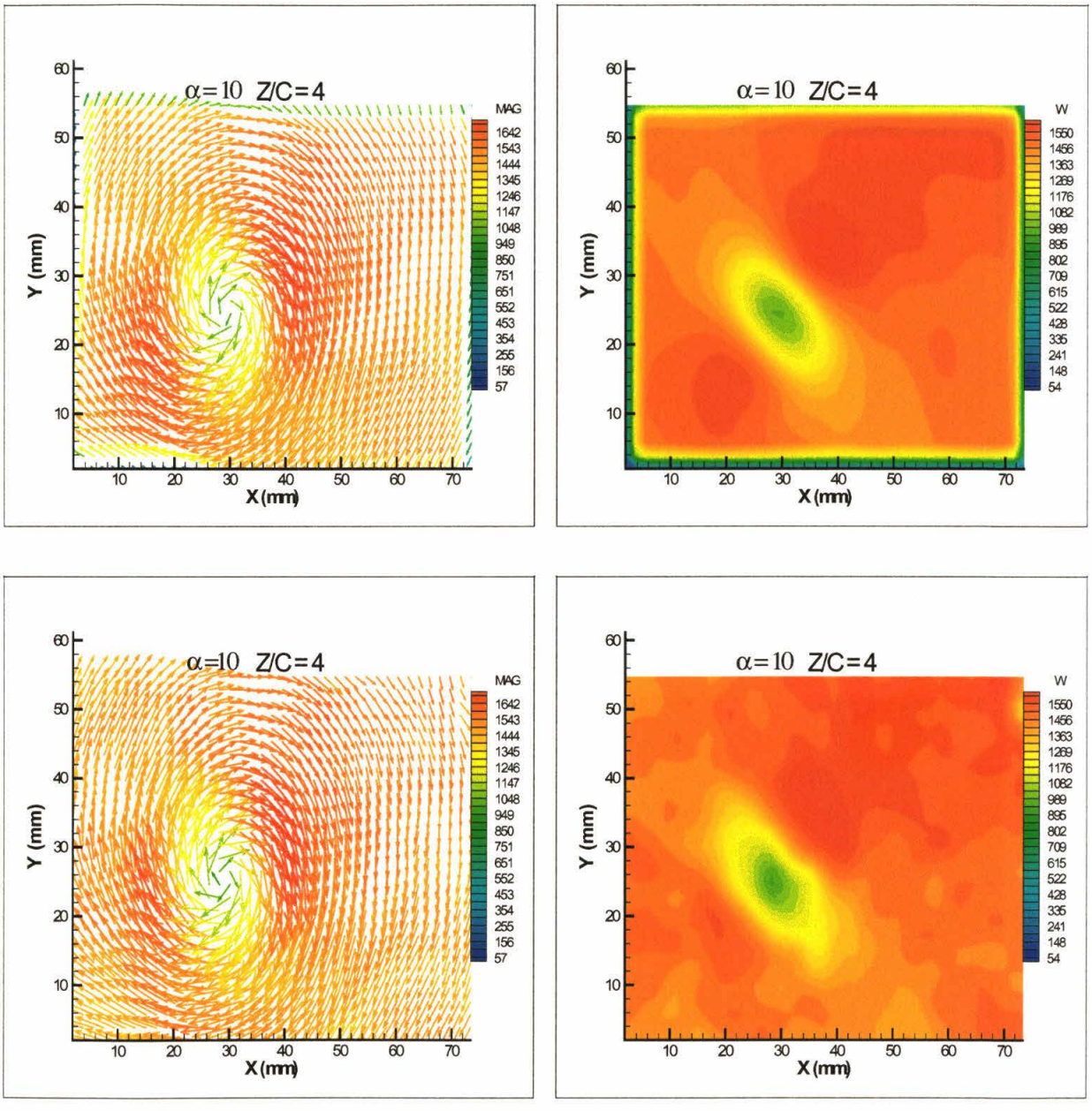

Figure 4.15. Velocity fields, z/c = 4, $\alpha = 10^0$ (upper: average, lower: instantaneous)

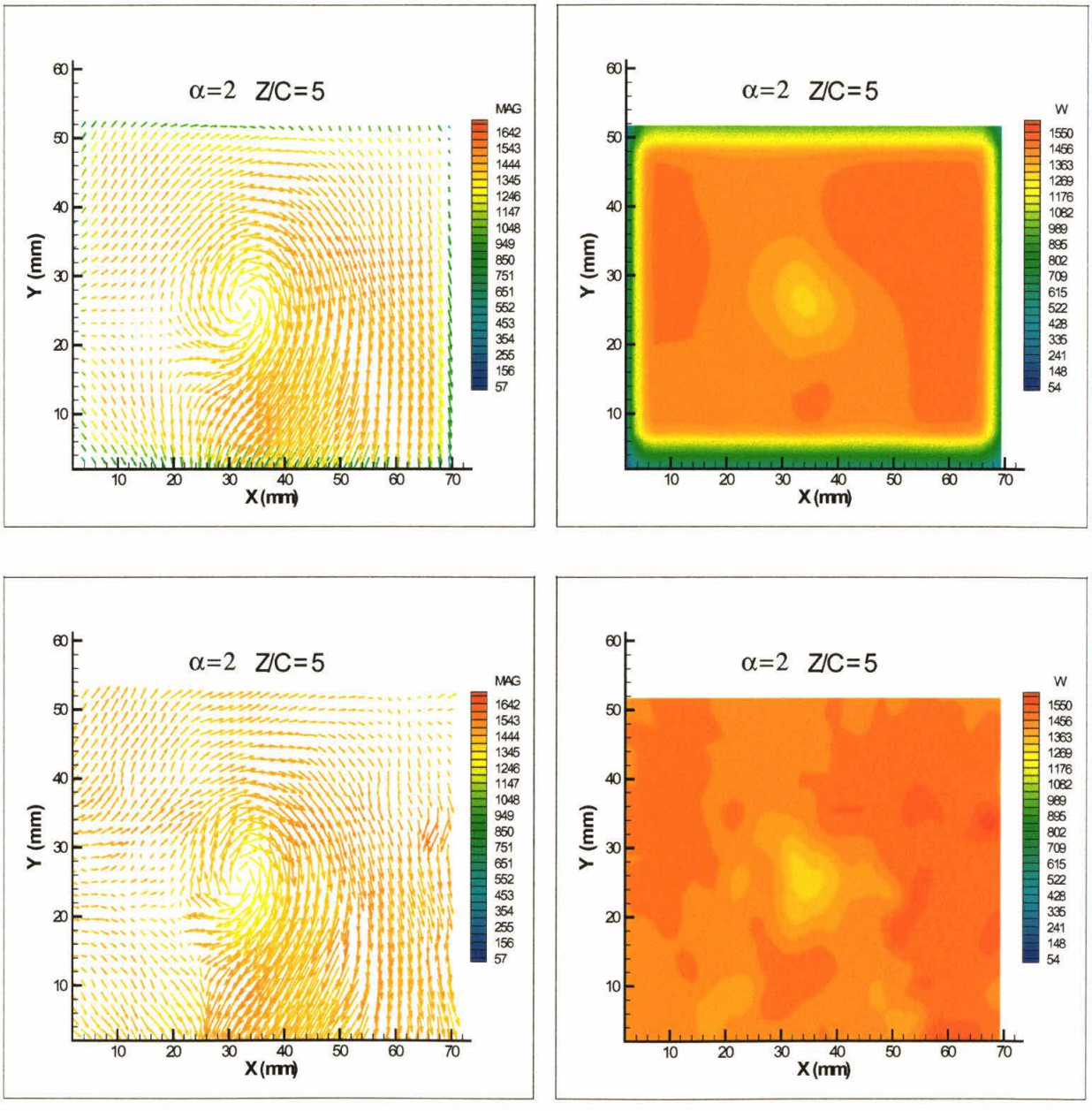

Figure 4.16. Velocity fields, z/c = 5, $\alpha = 2^0$ (upper: average, lower: instantaneous)

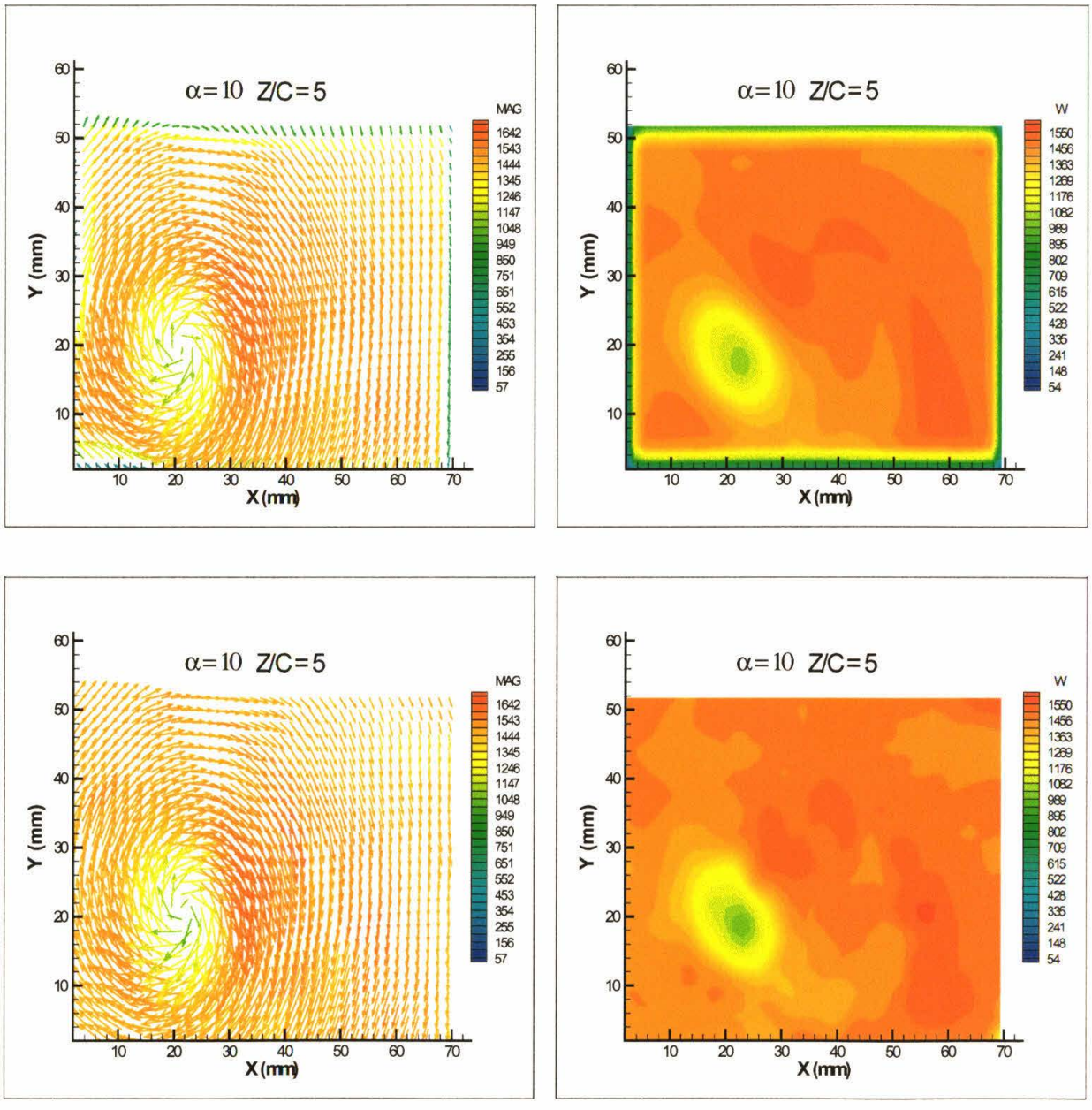

Figure 4.17. Velocity fields, z/c = 5, $\alpha = 10^0$ (upper: average, lower: instantaneous)

CHAPTER 5

Structure of the Wing Tip Vortex

5.1 Introduction

Flow quantities, such as circulation and vorticity, can be calculated from stereoscopic PIV data presented in Chapter 4. In addition, profiles of axial, azimuthal, and radial velocity along a line can be extracted from the three-component velocity data. Such information is important for investigating the structure of the wing tip vortex, which is the topic of the current chapter.

This chapter begins with the presentation of crossflow velocity and out-of-plane vorticity profiles along a cut through the center of the tip vortex. Next, circulation profiles as a function of radial distance are given. The peak values of some of the quantities are then compared with the theoretical prediction of Moore and Saffman (1973). All quantities presented in this chapter are computed from the average velocity fields, taking into account the effect of vortex meandering as described previously.

Flow quantities presented in this chapter are given for all angle of attack cases. Only quantities calculated from data collected at streamwise stations of 1 to 4-chord lengths behind the wing are presented in this chapter. Quantities obtained from data collected at a 5-chord length downstream of the wing is not presented because, for several angles of attack, the location of the wing tip vortex is too close to the edge of the

field of view. Also, quantities acquired from data taken at the trailing edge are not presented because, in most cases, the tip vortex is not yet well-defined at this streamwise station.

5.2 Crossflow Plane Profiles

In this section, crossflow profiles of azimuthal and axial velocity along a line parallel to the X-axis (along Y = constant) through the center of the vortex are presented. The profiles are extracted from the average velocity fields shown in Chapter 4.

In addition to the velocity profiles, vorticity profiles along the same cut as mentioned above are also presented. The vorticity fields from which the profiles are extracted are calculated from the average velocity fields. The complete presentation of the vorticity fields is given in Chapter 6.

5.2.1 Azimuthal Velocity Profile

As mentioned in Chapter 1, measurements of the tangential velocity profile of the tip vortex have been performed by many researchers in the past. This profile is of considerable interest due to its direct relevance to the aircraft safety issue. Also, measurement of the tangential profile is relatively easy to conduct.

In this section, the azimuthal velocity profile is obtained from the average velocity field (which is computed by taking into account the unsteadiness of the vortex) by taking a cut at a particular Y position as mentioned above. The azimuthal velocity profiles are shown in Figure 5.1-Figure 5.5, arranged in order of increasing angle of

attack. Each plot, corresponding to a particular value of α, ranging from 2^0 to 10^0, contains profiles at different streamwise stations. In each of the plots, the value of tangential velocity is normalized by the freestream velocity.

Each of the plots shows some similar trends. The value of the azimuthal velocity starts from zero at the core, rises almost linearly to peak values at the edge of the vortex, and falls off monotonically to small values away from the vortex core, which is identical to a typical vortex velocity profile. Also, it is clear that the profiles are not symmetric. The values of the maximum tangential velocity are smaller than the minimum values of the tangential velocity.

The figures also indicate that the peak value of the azimuthal velocity increases with α, which is not surprising at all. The evidence of strong rotational motion, induced by the tip vortex, is without a doubt shown in the plots. The maximum magnitudes of the tangential velocity range from approximately 10% of the freestream velocity for the $\alpha = 2^0$ case to approximately 50% of the freestream velocity for the $\alpha = 10^0$ case.

5.2.2 Axial Velocity Profile

Results from previous measurements of axial velocity have indicated regions of either excess or deficit axial velocity within the vortex core. Green (1988) observed that the core axial velocity is higher than the freestream velocity for Z/C = 2 and 4 (the measurements were made at Re~10^5). Logan (1971) reported an axial velocity deficit within the vortex core at Z/C = 10 and 26. Bippes (1977) observed the reversal of the excess core axial velocity at Re > 5 x 10^5 and concluded that the direction of axial flow within the core depends on the Reynolds number. The reversal of the core axial velocity

direction, when Re is increased, is also observed by Green (1988). Moore and Saffman (1973) showed that an excess or deficit of core axial velocity depends not only on the Reynolds number, but on Z/C and the tip loading as well.

The axial velocity profiles, along the same line described in the previous section, are displayed in Figure 5.6-Figure 5.10. As before, the figures are arranged in order of increasing angle of attack. In each plot, the axial velocity is normalized with the freestream velocity as before.

The axial velocity profile depicted in Figure 5.6-Figure 5.10 exhibits some similar trends. For all α cases at all Z/C considered in this study, the axial velocity within the vortex core is less than the freestream velocity. The axial velocity profiles are at a minimum at the center of the vortex core and increase to the freestream value away from the vortex core. In some cases, $\alpha = 10^0$ at Z/C = 1 for example, the appearance of small axial velocity excess, approximately 3% of the freestream velocity, is observed near the edge of the vortex. This observation is in agreement with the results obtained by Logan (1971).

The axial velocity profile in the vortex core is best described in the relative coordinate system in which fluid at infinity is at rest (obtained by subtracting 1 from the values given in the plots). In this coordinate system, the magnitude of the peak axial velocity deficit increases with angle of attack. The peak magnitude ranges from 10% to 40% of freestream velocity. This is approximately the same as the range for the peak tangential velocity discussed in previous subsection. Also, for a given angle of attack, the core axial velocity deficit decreases with the downstream distance from the wing.

This is a strong indication of streamwise acceleration of the core fluid within the streamwise regions considered in the experiment.

5.2.3 Out-of-plane Vorticity Profile

The axial vorticity field can be calculated from the in-plane components of the average velocity field. The complete presentation of the out-of-plane vorticity fields is given in Chapter 6. In this subsection, we only present the axial vorticity profiles along a cut through the center of the vortex as described before.

The plots of the axial vorticity profiles for the range of α considered in this experiment are shown in Figure 5.11-Figure 5.15, where the figures are arranged as usual. Each of the plots shown in Figure 5.11-Figure 5.15 reveals that the vorticity peaks at the center of the core and approaches zero outside the core region. This vorticity distribution is evidently different from the vorticity distribution of a Rankine vortex, in which the vorticity is constant inside the vortex and zero outside the vortex. In fact, the shape vorticity profile inside the vortex closely resembles an "inverted" Gaussian distribution.

The values of the peak vorticity, for all α considered, are plotted against the downstream distance from the wing in Figure 5.16. At each downstream station, the magnitude of the peak vorticity increases with an increasing angle of attack. The magnitude of the peak vorticity decreases with increasing Z/C. For each α case, the peak is at its highest value at Z/C = 1 and lowest value at Z/C = 4.

5.3 Circulation

Circulation can be calculated from the in-plane velocity components by computing the line integral of velocity along a circular contour concentric with the vortex. In this thesis, the center of the vortex is defined as the point at which the magnitude of the axial vorticity is the highest. In this section, the results of the calculation of the circulation as a function of the radial distance from the center of the vortex are presented. Plots shown in this section are organized as usual.

The maximum radial distance from the vortex center, at which the circulation is calculated, is limited due to the limitation in the measurement field of view. The maximum radial distance for the calculation is set between 20~25 mm from the vortex center to ensure that the circular contour is still far enough from the edges of the field of view where the measured velocity are less reliable.

The circulation profiles as a function of radial distance from the vortex center for the $\alpha = 2^0$ and 4^0 cases are displayed in Figure 5.17 and Figure 5.18, respectively. As shown in the figures, the values of circulation start from a small value at small R and increase to reach peak values at a radial distance of 10~15 mm from the vortex center. However, instead of staying constant at the maximum values as R increases further, the values of the circulation reduce to smaller values. In fact, for the $\alpha = 2^0$ case at Z/C = 1, the circulation profile depicted in Figure 5.17 clearly exhibits an overshoot. The circulation overshoot is mentioned in Saffman (1991) in his discussion of turbulent line vortices. He predicted that turbulence creates a region of concentrated vorticity surrounding the tip vortex, with its sign opposite that of the tip vortex. However, the circulation overshoot observed here is due to the presence of opposite sign vortex shed by

the wing (discussed in the next chapter), which is contained inside the circular contour used to calculate the circulation. Therefore, the circulation overshoot observed here is not the phenomenon that was predicted by Saffman.

The circulation profiles for $\alpha = 6$, 8, and 10^0 are shown in Figure 5.19, Figure 5.20, and Figure 5.21, respectively. Here, the largest circular contour used for calculating the integral is evidently not large enough. However, it seems that in these cases each of the circulation profiles for a particular α asymptotically converges to one value at higher R. Also, the maximum value of circulation for a given α case is approximately constant, over the range of Z/C considered in this chapter (Z/C = 1~4). This indicates that the total circulation is conserved over the range of Z/C.

Several additional trends can be identified from the set of plots shown in Figure 5.17 to Figure 5.21. First, circulation at a given R increases with the angle of attack. This also means that the maximum value of circulation increases with the angle of attack as expected. Also, the radius, at which the value of circulation reaches a maximum, increases with the angle of attack for the lower angle of attack cases. This, however, cannot be concluded for the higher angle of attack cases because the circulation profiles have not yet reached a maximum at the largest contour used for the line integration. Finally, the slope of the circulation in the region inside the vortex core decreases with increasing downstream distance from the wing, which indicates the slowing down of the azimuthal motion with increasing Z/C.

The values of the circulation obtained from the experiment can be compared to the total circulation of the wing, calculated from a simple theoretical prediction based on the *Lifting-line Theory*. For steady two-dimensional inviscid flow over arbitrary shaped

cylinder, circulation is related to the lift per unit span according to the *Kutta-Zhukovsky Theorem*:

$$\Gamma = \frac{l}{\rho U},$$

where l is the lift per unit span and ρ is the density of the fluid.

The above equation can be rewritten by using the definition of lift coefficient, C_l, as

$$\Gamma = \frac{0.5\rho U^2 C C_l}{\rho U} = 0.5 U C C_l .$$

C_l is related to α by

$$C_l = a\ (\alpha - \alpha_{l=0}),$$

where a is the three-dimensional lift curve slope. For wing with elliptic distribution, it may be shown that (Houghton and Carpenter 1993):

$$a = \frac{2\pi}{1 + \frac{2}{AR}}.$$

Thus

$$\Gamma = \frac{k\pi U C(\alpha - \alpha_{l=0})}{1 + \frac{2}{AR}} \qquad (5\text{-}1)$$

, where k is a constant added to Equation 5-1 take into account the way the wing is mounted (k = 1 for a wing in a freestream). For a wing mounted in the experimental configuration (Green 1988), $k = 1.05$.

The values of the circulation calculated using Equation 5-1 are shown as black solid lines in Figures 5.17 to 5.21. As shown in the figures, the values of circulation obtained from the experiment and those calculated using Equation 5-1 differ by 30~35 %

for the lower angle of attack cases and 15~18 % for the higher angle of attack cases. The relatively large difference between the predicted and the measured value is probably due to the use of elliptic loading distribution assumption in deriving Equation 5-1, which is obviously not a very good assumption for the wing used in the present experiment. Also, the measured circulation profiles have not yet reached a maximum at the largest contour used for the line integration for the higher α cases. Accordingly, the difference between the measured and the predicted values may be smaller than 15~18 % for the higher α cases.

As mentioned in Section 5.3, the maximum values of circulation do not vary significantly with Z/C (in the range of Z/C = 1~4). As will be shown in the later chapters, the wing tip vortex actually forms on the suction side of the wing surface. It is interesting to compare the maximum circulation (for a given α case) at these stations to the circulation of the tip vortex at the trailing edge of the wing (Γ_v). As will be shown in Chapter 6, the wing tip vortex at the trailing edge is not circular. Therefore, the computation of circulation with circular contour might not be as accurate as for the cases presented above. Consequently, the values of the circulation at the trailing edge are estimated by integrating along contours that follow the shape of the tip vortex at the trailing edge. The estimated values of circulation of the wing tip vortex at the trailing edge are presented in Table 5.1. In addition, the values of tip vortex circulation at the trailing edge are compared with the values of the maximum circulation at Z/C = 4. As presented in Table 5.1, the circulation of the wing tip vortex at the trailing edge is approximately 95 % (for $\alpha = 2^0$ to6^0 case) and 85% (for $\alpha = 8^0$ and 10^0 case) of the maximum circulation at station farther downstream, where almost all vorticity has rolled

up into the trailing vortex (see Chapter 6). This result shows that almost all of the "bound" vorticity has rolled up into the trailing vortex at the trailing edge of the wing. In other words, the trailing vortex is almost completely formed when it leaves the wing.

α	$\Gamma_{v,Z/C=0}$ (mm^2/s)	$\Gamma_{max,Z/C=4}$(mm^2/s)	$\Gamma_{v,Z/C=0}/\Gamma_{max,Z/C=4}$
2	-6852	-7157	0.96
4	-14,359	-15,000	0.96
6	-26,382	-27,890	0.95
8	-32,114	-37,311	0.86
10	-38,778	-44,571	0.87

Table 5.1. Comparison of circulation at the trailing edge and the total circulation at Z/C = 4

5.4 Core Size

The growth rate of wing tip vortex core is another quantity of interest, especially in the near field region where the shear layer rolls up into a tip vortex. The growth rate can be estimated from the slope of the core size as a function of the streamwise station. In this section, the estimated size of the core is obtained from the information presented in the previous section.

The radius of the vortex core is normally defined as the value of R for which the magnitude of V_θ is at a maximum. As discussed in Section 5.2.1, the profile of the tangential velocity is not symmetric with respect to the core axis for all α cases.

Therefore, it is difficult to obtain the radius from the plots displayed in Section 5.2.1 without any ambiguity.

Another way to estimate the core size is to use circulation. By normalizing the circulation in a certain way ($\frac{\Gamma}{2\pi r}$), the "phase" average tangential velocity can be estimated.

Figure 5.22 shows the plots of circulation as a function of R, where the value of circulation is normalized as mentioned above. The two plots shown are for cases $\alpha = 2^0$ and $\alpha = 10^0$, which represent the low and the higher angle of attack cases, respectively. The maximum value for the "average" azimuthal velocity is between 9%~7.4% of U for $\alpha = 2^0$ case and 37%~43% of U for $\alpha = 10^0$ case. These values are comparable to those presented in Section 5.2.1.

From plots similar to that shown in Figure 5.22, the radius, for which the value of V_θ is at a maximum, can be acquired and the size of the core can be estimated. The results are shown in Figure 5.23, where the core radius for all α case is plotted against the normalized streamwise station. The size of the vortex core clearly increases with downstream distance, for all α cases. The radius of the core ranges from approximately 5.5 to 7.5mm for the $\alpha = 2^0$ and approximately 7 to 9 mm for the $\alpha = 10^0$ case. The growth of the core size is almost linear for the higher α case ($\alpha = 6^0, 8^0, 10^0$), with the slope of about 0.55. Note that, unlike a *point vortex*, the wing tip vortex core radius, as defined in this subsection, is not the same as the radius at which the circulation is at maximum (see Figures 5.17 to 5.21).

5.5 Comparison with Theory

In this section, we compare some of the experimental results, presented in this chapter, with the theory of Moore and Saffman (1973). In the theory, the wing tip vortex flow is assumed to be laminar and the relative axial velocity is much smaller than the freestream velocity. The theory includes the effect of core viscosity. The theory is derived for arbitrary wing loading. In this section, the elliptic loading assumption is used in all calculations. With this assumption, the vortex core radius, maximum tangential velocity, and axial velocity at the vortex center are given by

$$r = 2.92\sqrt{\frac{\upsilon z}{U}} \tag{5-2}$$

$$V_{\theta \max} = 0.49\frac{\sqrt{6}}{2}U\alpha\frac{c}{\sqrt{b}}\left(1+\frac{\pi c}{2b}\right)^{-1}\left(\frac{\upsilon z}{U}\right)^{-\frac{1}{4}} \tag{5-3}$$

$$\frac{W_{core}-U}{U} = -2.4x10^{-5}\left(\frac{\alpha}{\deg}\right)^{2}\sqrt{\mathrm{Re}}\left(\frac{c}{z}\right)^{\frac{1}{2}} - 0.28\left(\frac{c}{z}\right)^{\frac{1}{2}}. \tag{5-4}$$

The first comparison is made for the magnitudes of the peak tangential velocity. As mentioned before, the magnitudes of the peak tangential velocity, presented in Section 5.2.1, are not symmetric with respect to the core axis. Therefore, as in Section 5.4, the peak values are obtained from the normalized circulation plots. The comparison between the peak values obtained from the experiment and that predicted by the theory is shown in Figure 5.24, where the peak tangential velocity normalized by the freestream velocity, for all α cases, is plotted against the normalized streamwise station. In the figure, the solid line with a particular color is the theoretical prediction for a given α case, while

symbols with the same color are the corresponding results from the experiment. As shown in the figure, the agreement is not very good for all α cases. The theory seems to under predict the peak tangential velocity by 40 to 55 %.

The plot of normalized axial velocity at the center of the core vs. the streamwise station is shown in Figure 5.25. Here, the Y-axis is actually the normalized axial velocity relative to the freestream velocity. Unlike in the azimuthal velocity case, the theoretical prediction agrees quite well for the low angle of attack case. For the higher α case, the theoretical prediction is still quite close to the experimental result at small Z/C except for the $\alpha = 10^0$ case.

The size of the vortex core presented in the last section can also be compared with the theoretical prediction. The comparison is shown in Figure 5.26. Here, the estimated core radius from the experiment is slightly higher than that predicted by the theory, for all α. Also, results from the experiment indicate that the growth rate of the vortex core weakly depends on the angle of attack while the theory predicts the growth rate to be independent of α. However, results from both the theory and experiment qualitatively agree with each other.

5.6 Summary

In this chapter the structure of the measured trailing vortex is investigated. Profiles of azimuthal velocity, axial velocity, and axial vorticity along a line through the center of the core are presented. Plots of circulation as a function of radial distance from

the vortex center are displayed. Also, the size of the vortex core is estimated. Finally, some of the results are compared with the theory of Moore and Saffman (1973).

All quantities presented are calculated or extracted from the average velocity fields. The average velocity fields are computed by taking into account the effect of vortex meandering.

A brief listing of salient results presented in this chapter are as follows:

1. For a given α, the peak azimuthal velocity decreases with increasing streamwise distance from the wing. At a given Z/C, the peak azimuthal velocity increases with α. The profile of tangential velocity is not symmetric with respect to the core axis.
2. There is a strong axial velocity deficit in the core region. In the relative coordinate system in which the fluid at infinity is at rest, the magnitude of the peak axial velocity deficit increases with the angle of attack. Also, for a given angle of attack, the core axial velocity deficit decreases with the downstream distance from the wing. The peak axial velocity is of the same order of magnitude as the peak tangential velocity.
3. The circulation of the wing tip vortex at the trailing edge is approximately 86% to 96% of the value of maximum circulation at stations farther downstream, which shows that almost all the "bound" vorticity has rolled up into the trailing vortex at the trailing edge of the wing. Downstream of the wing, the value of the maximum circulation is approximately constant. The magnitude of the peak vorticity decreases with Z/C while the size of the vortex core increases with Z/C, as the vorticity diffuses away from the core region of the vortex.

4. The trends of increasing or decreasing peak azimuthal velocity, peak axial velocity, and core size with increasing downstream distance from the wing agree with the theoretical predictions of Moore and Saffman (1973).

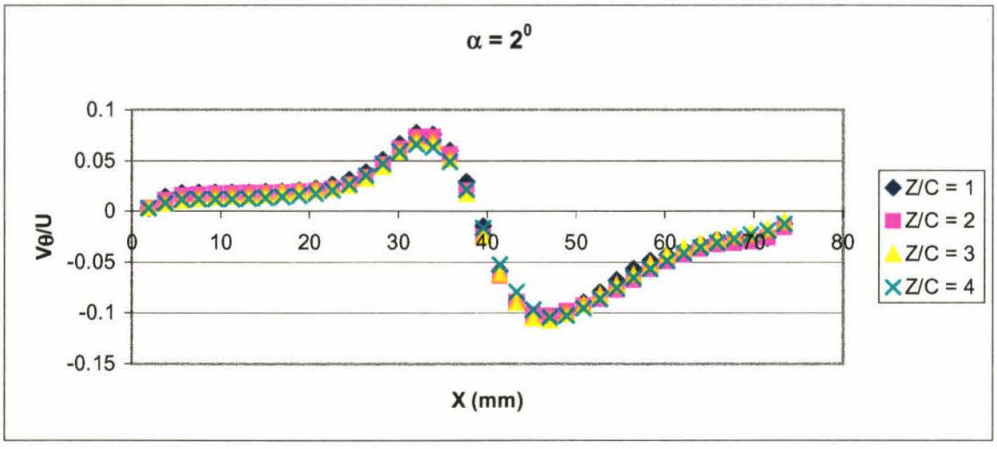

Figure 5.1. Azimuthal velocity profile for $\alpha = 2^0$ case

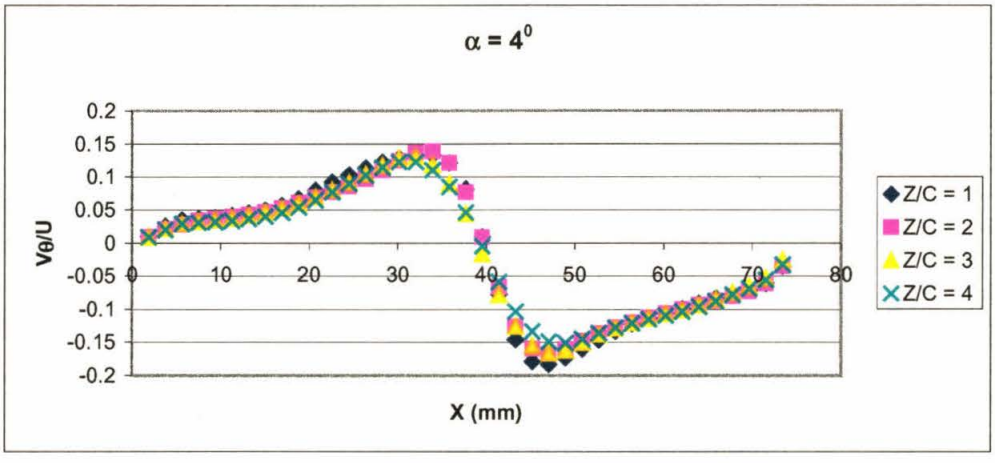

Figure 5.2. Azimuthal velocity profile for $\alpha = 4^0$ case

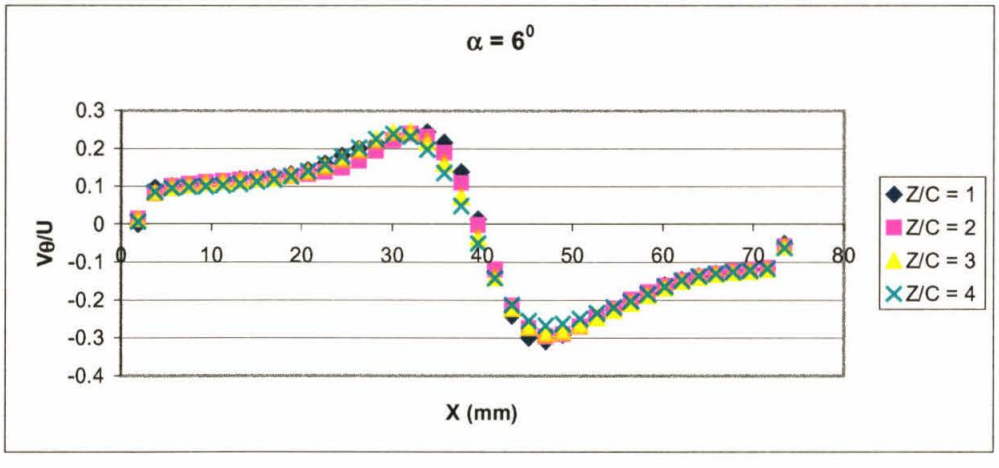

Figure 5.3. Azimuthal velocity profile for $\alpha = 6^0$ case

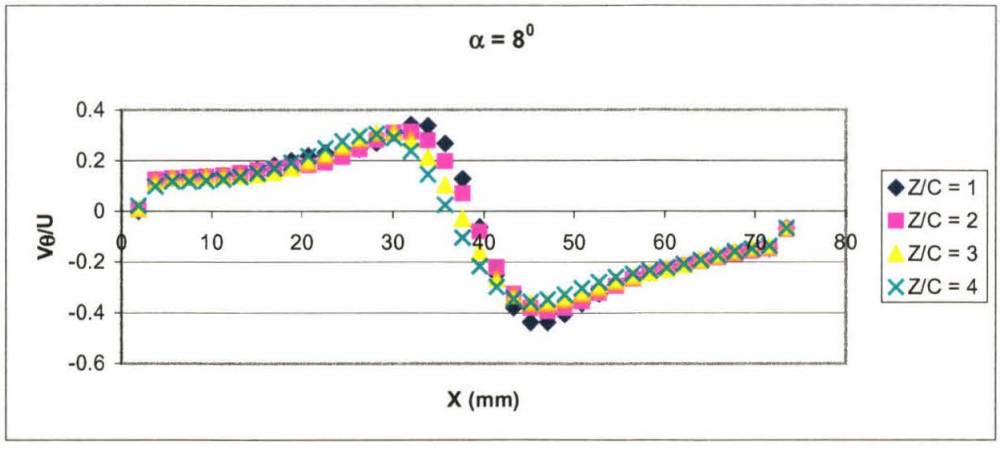

Figure 5.4. Azimuthal velocity profile for $\alpha = 8^0$ case

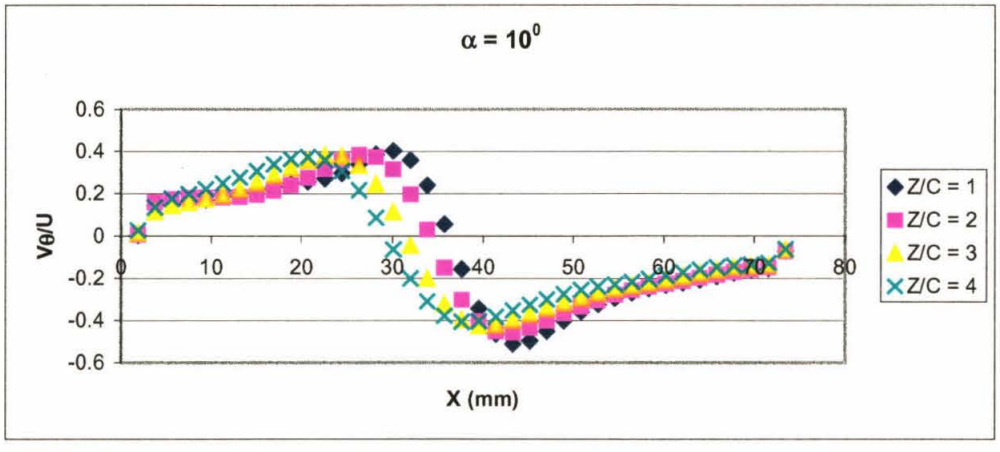

Figure 5.5. Azimuthal velocity profile for $\alpha = 10^0$ case

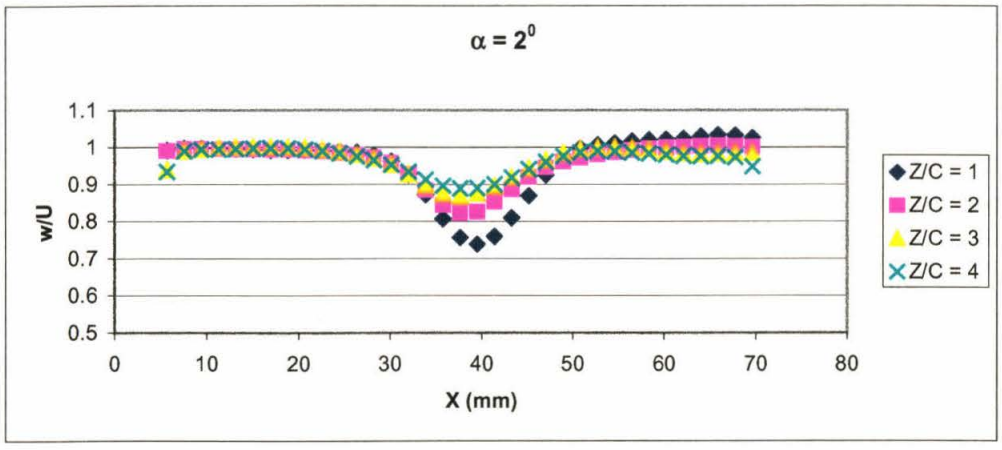

Figure 5.6. Axial velocity profile for $\alpha = 2^0$ case

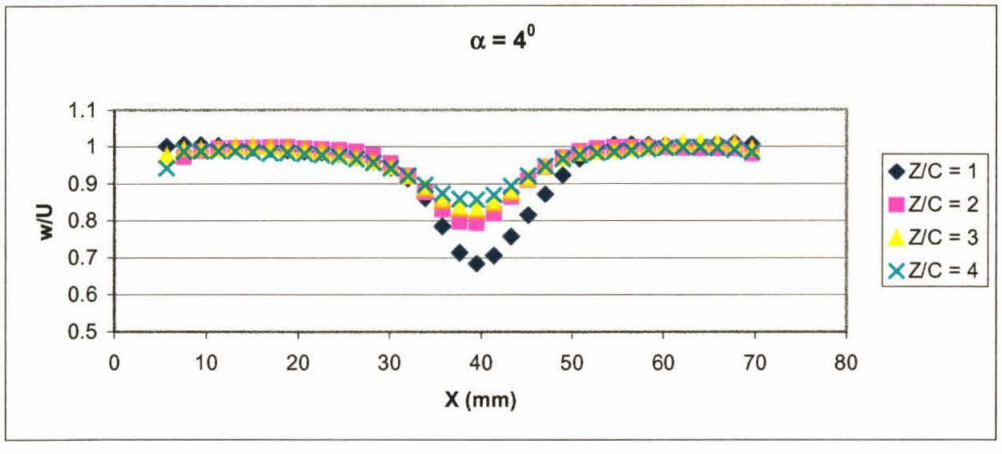

Figure 5.7. Axial velocity profile for $\alpha = 4^0$ case

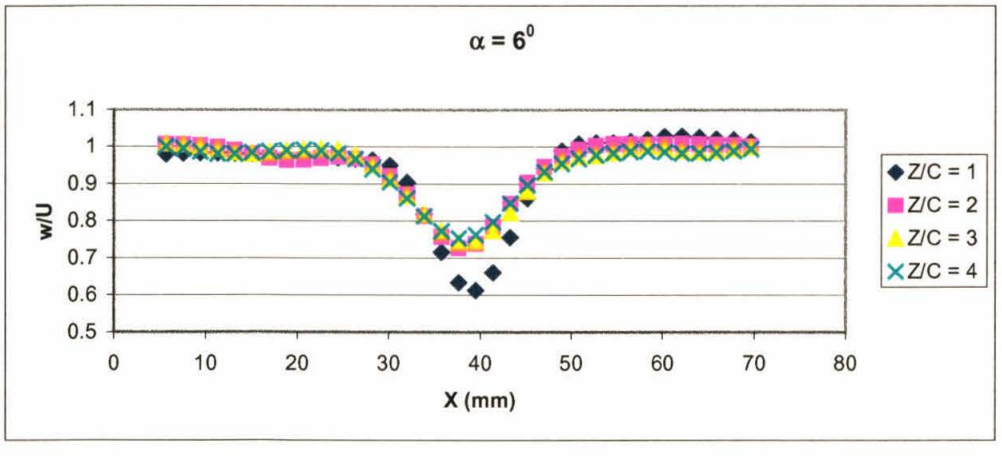

Figure 5.8. Axial velocity profile for $\alpha = 6^0$ case

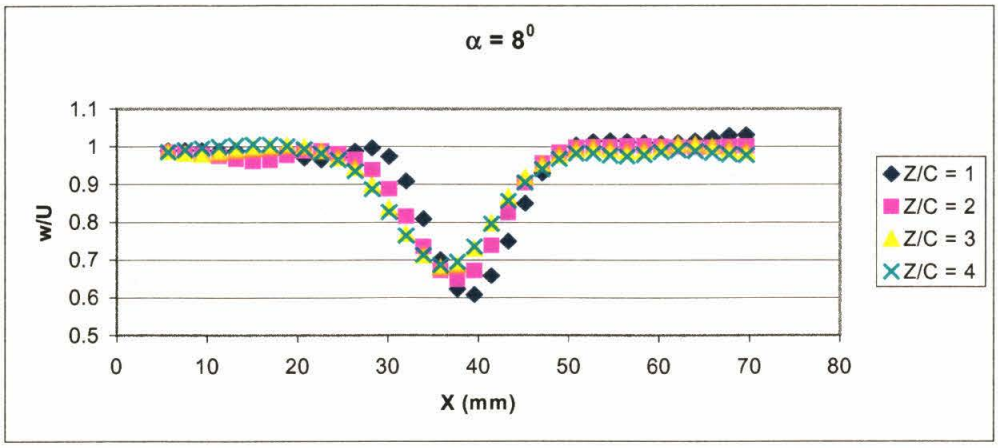

Figure 5.9. Axial velocity profile for $\alpha = 8^0$ case

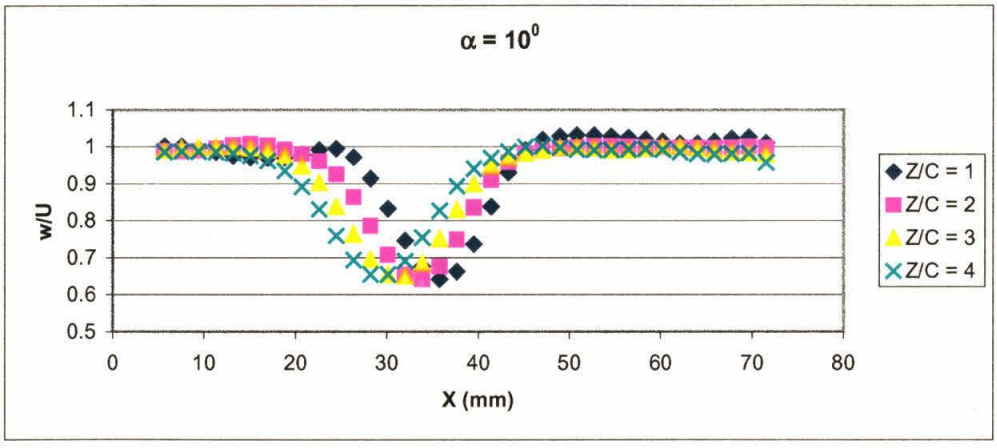

Figure 5.10. Axial velocity profile for $\alpha = 10^0$ case

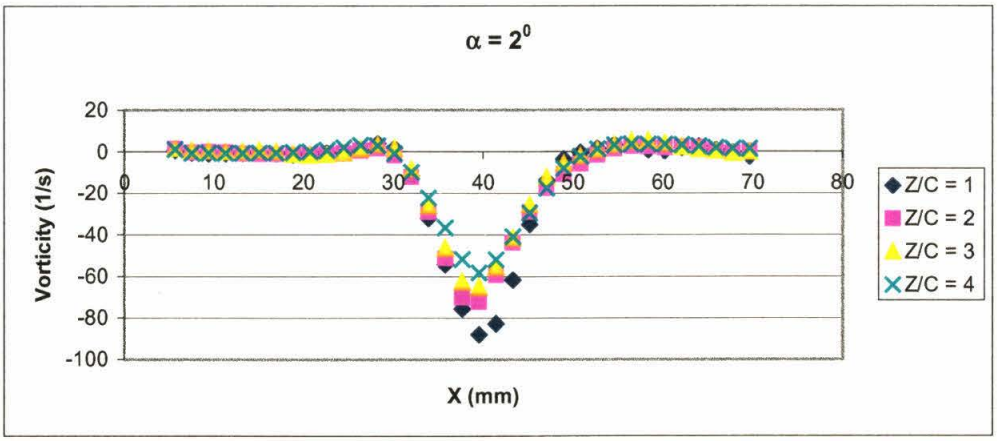

Figure 5.11. Out-of-plane vorticity profile for $\alpha = 2^0$ case

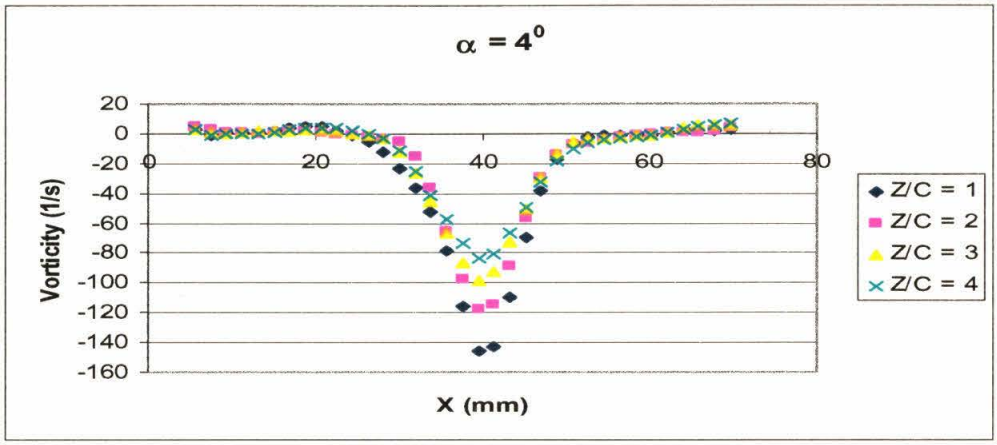

Figure 5.12. Out-of-plane vorticity profile for $\alpha = 4^0$ case

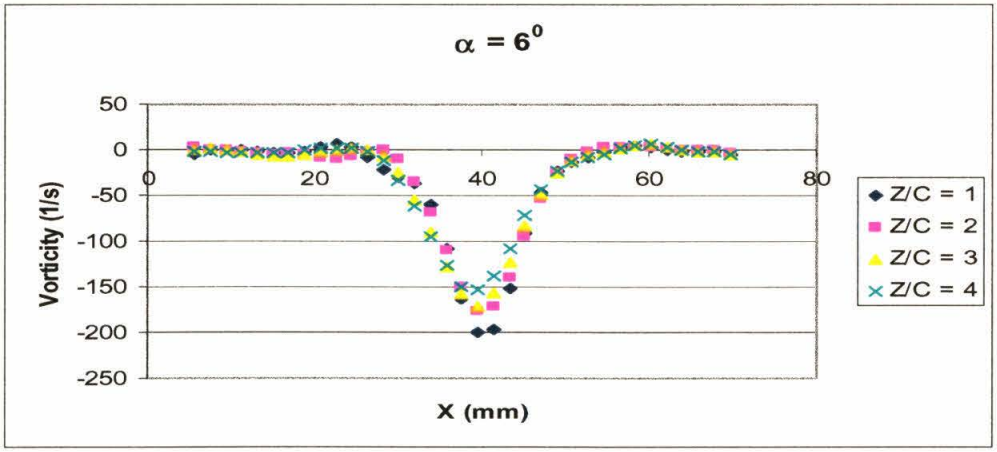

Figure 5.13. Out-of-plane vorticity profile for $\alpha = 6^0$ case

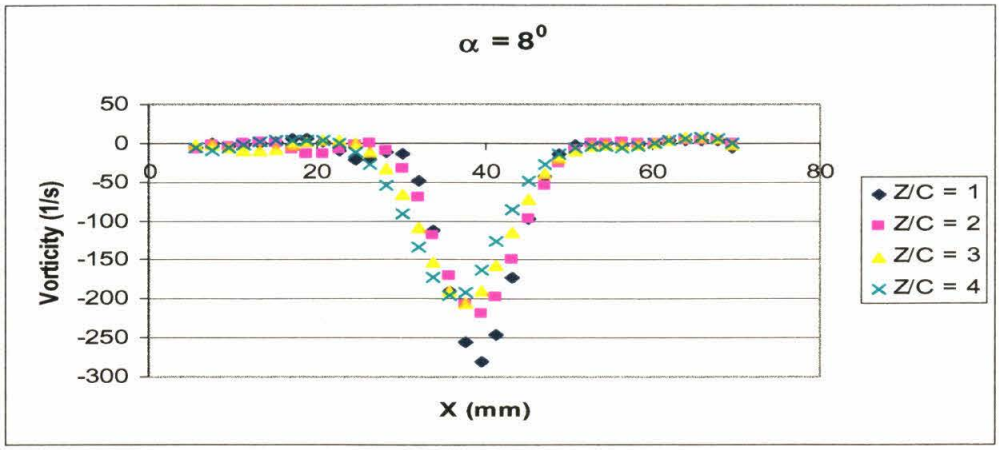

Figure 5.14. Out-of-plane vorticity profile for $\alpha = 8^0$ case

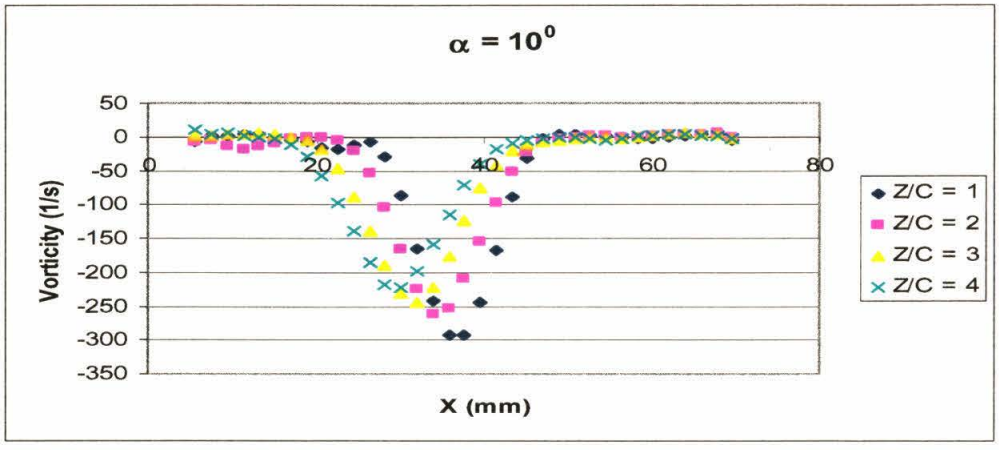

Figure 5.15. Out-of-plane vorticity profile for $\alpha = 10^0$ case

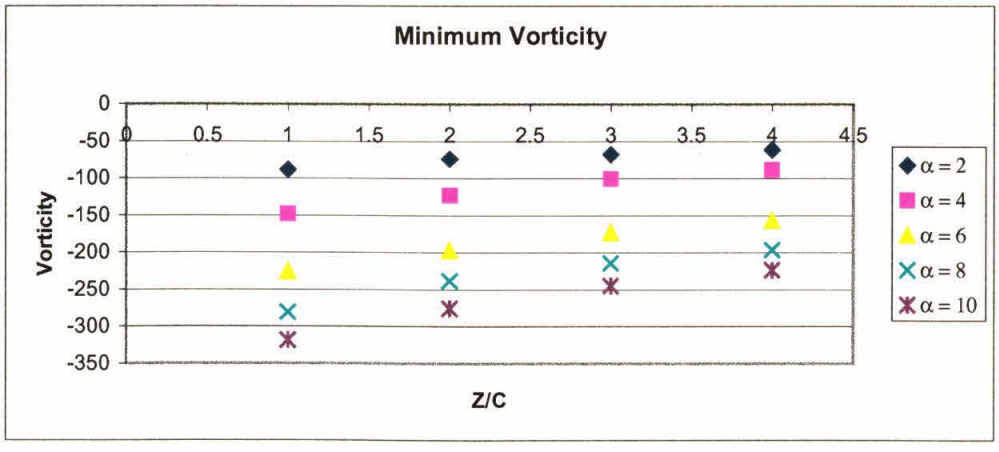

Figure 5.16. Peak vorticity vs. Z/C

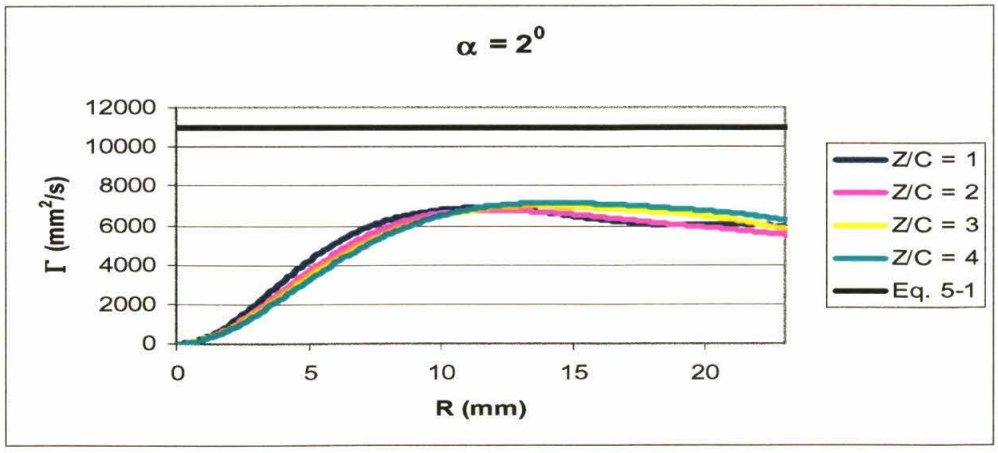

Figure 5.17. Circulation vs. radius for $\alpha = 2^0$ case

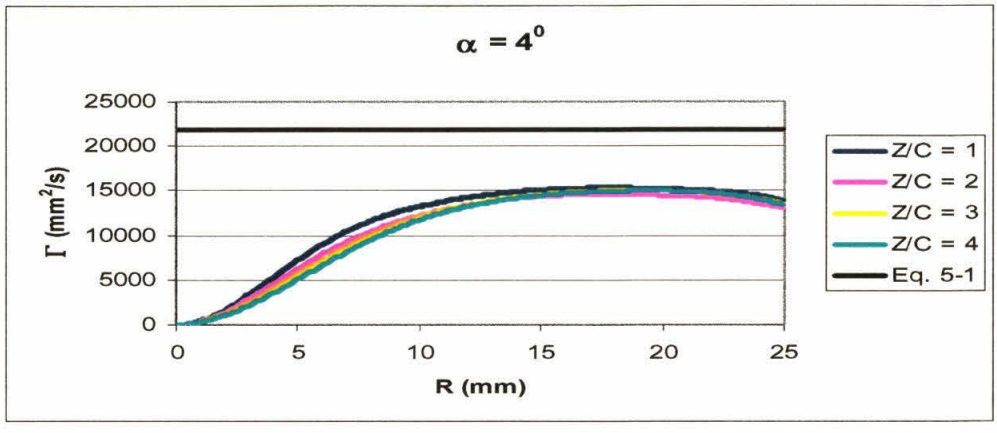

Figure 5.18. Circulation vs. radius for $\alpha = 4^0$ case

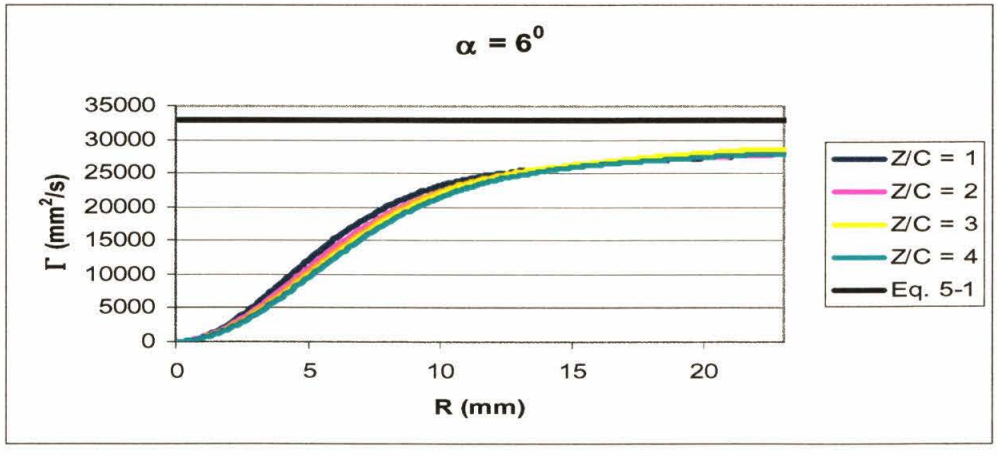

Figure 5.19. Circulation vs. radius for $\alpha = 6^0$ case

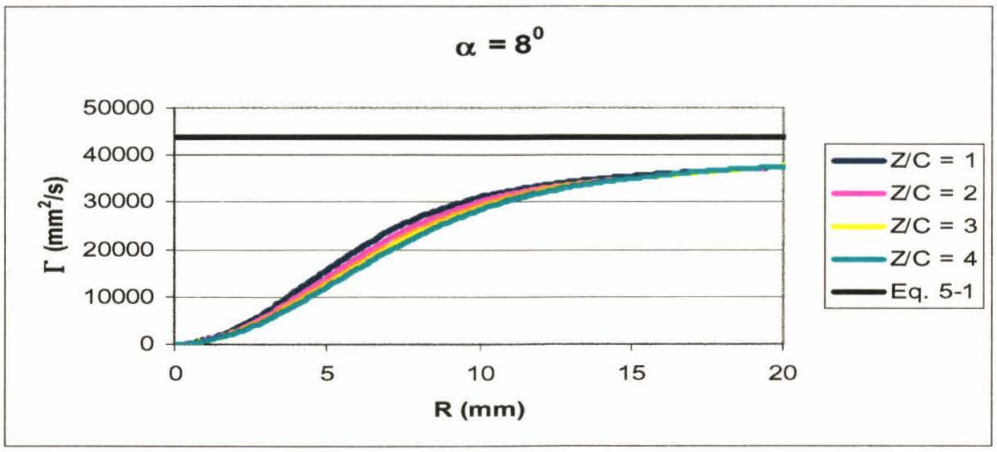

Figure 5.20. Circulation vs. radius for $\alpha = 8^0$ case

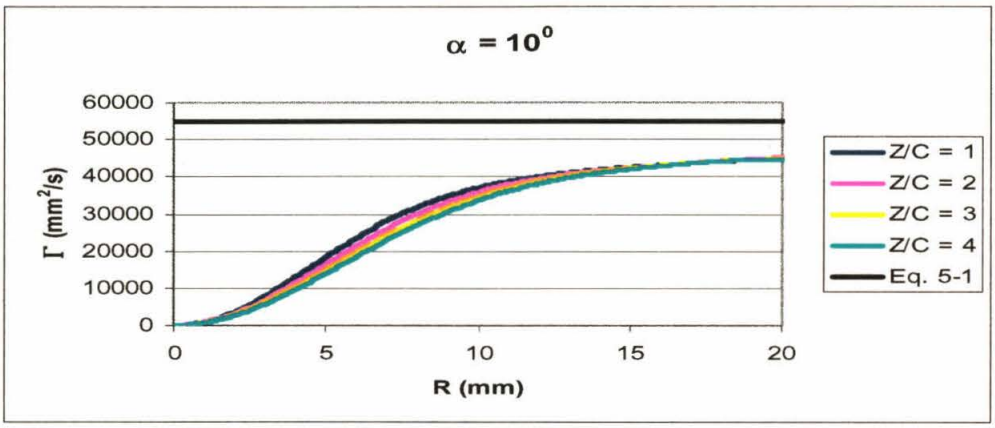

Figure 5.21. Circulation vs. radius for $\alpha = 10^0$ case

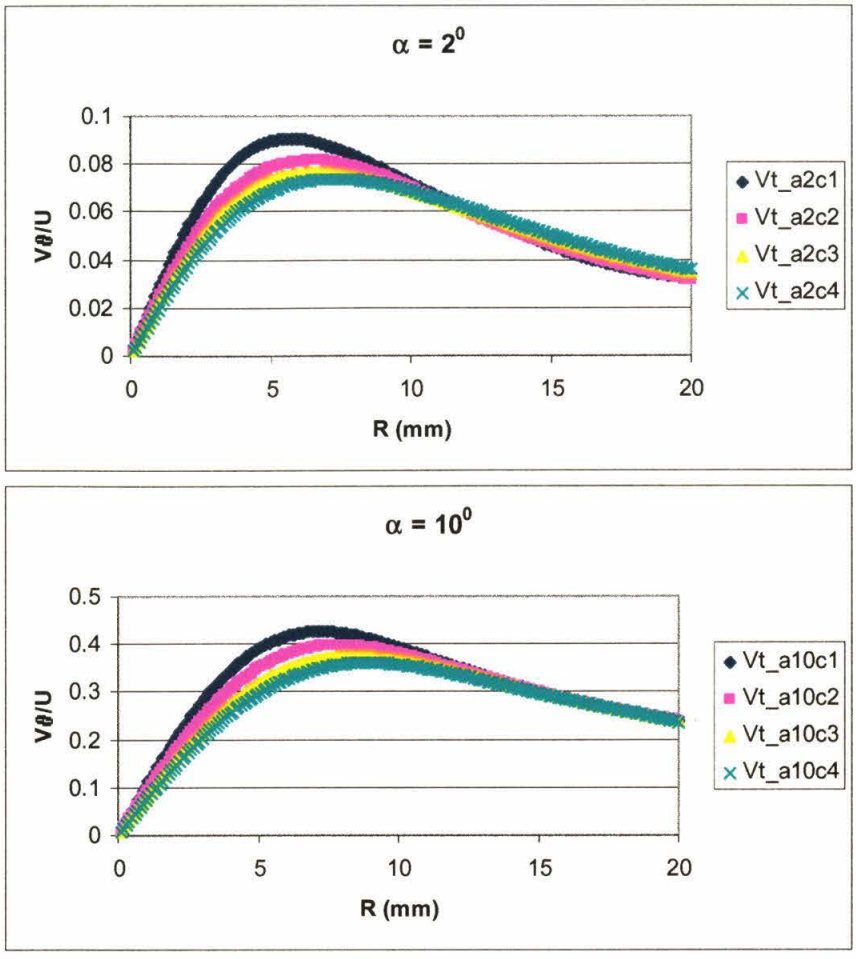

Figure 5.22. Mean V_θ vs. radius

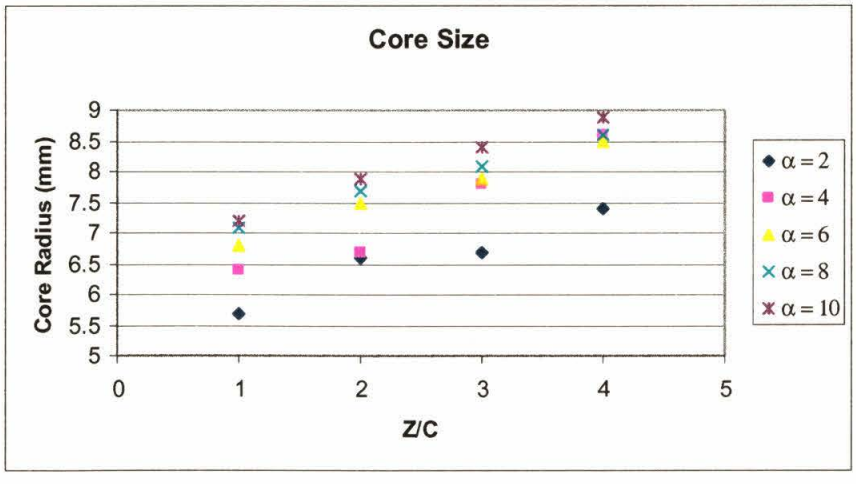

Figure 5.23. Core radius vs. Z/C

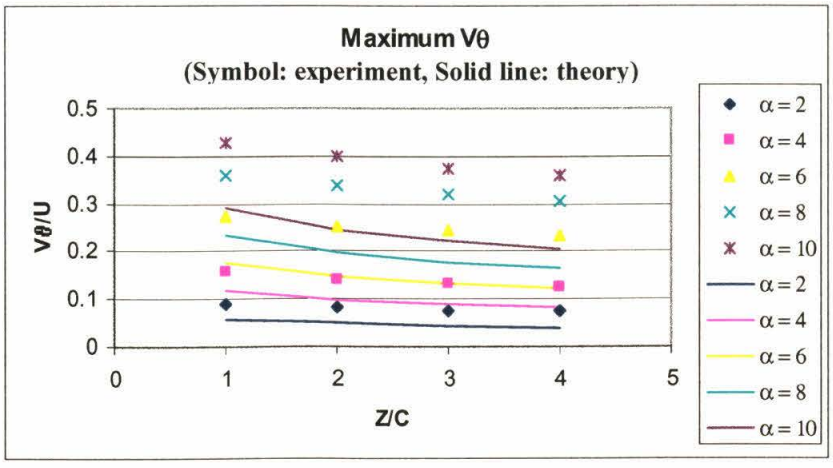

Figure 5.24. Maximum V_θ vs. Z/C

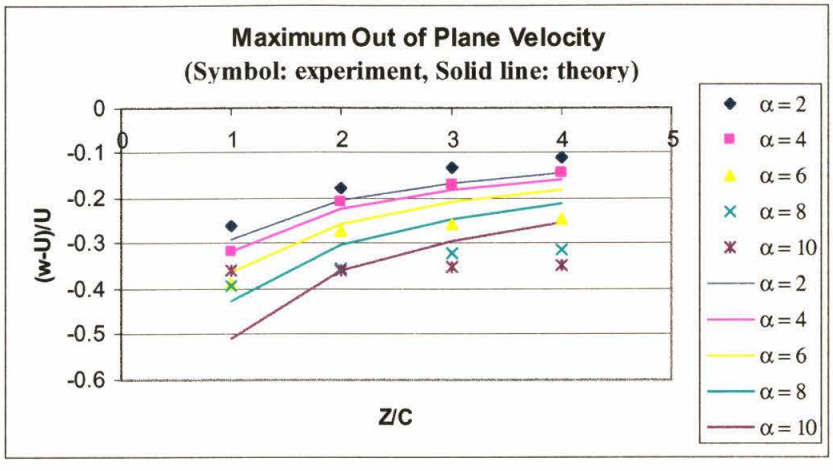

Figure 5.25. Minimum w vs. Z/C

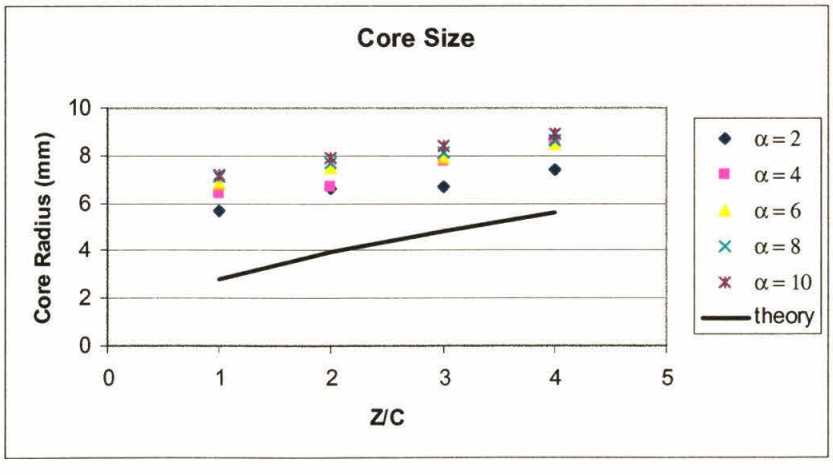

Figure 5.26. Core radius vs. Z/C

CHAPTER 6

Dynamics of the Wing Tip Vortex

6.1 Introduction

The use of SPIV, global measurement technique, in the current work allows us to obtain the out-of-plane vorticity field from the in-plane components of the measured velocity field. The information provided by the vorticity field is certainly valuable in the understanding of the dynamics of the trailing vortex.

From the vorticity field, vortices other than the tip vortex shed by the wing can also be identified. The presence of these vortices obviously affects the motion of the wing tip vortex. In this chapter, we examine how the interactions between vortices influence the dynamics of the trailing vortex.

This chapter begins with the presentation of the average axial vorticity fields at the trailing edge of the wing. The streamwise evolution of the average vorticity field is considered next. The vortex core trajectories identified from the vorticity field are presented. Subsequently, the instantaneous vorticity fields are displayed. Finally, the effect of the instantaneous vorticity distribution on the unsteadiness of the tip vortex is discussed.

6.2 Average Axial Vorticity Distributions

In this section, contours of axial vorticity are presented. The axial vorticity fields are computed from the in-plane components of the average velocity fields presented in Chapter 4. The vorticity fields at the trailing edge of the wing are displayed for all α cases. Vorticity fields at other streamwise stations are given for only the $\alpha = 4^0$ and 10^0 cases, which represent the low and high angle of attack case, respectively. At the end of this section, trajectories of the wing tip vortex core for all α cases are presented. As a reminder, the image of the outboard part of the wing, at $\alpha = 0^0$, with respect to the plots is approximately at X = 40mm with the tip at Y = 41.5mm.

6.2.1 Vorticity Distributions at the Trailing Edge of the Wing

The first case presented in this subsection is the zero angle of attack case. Since the airfoil shape is symmetric, the wing is not expected to generate any lift. The contour of axial vorticity for this case is shown in Figure 6.1. Two vortices of opposite signs are clearly depicted in the figure. The sizes and magnitudes of their strength are approximately the same. The vortices are located very close to the tip on the two different sides of the wing surface.

As the angle of attack is increased to 2^0, the axial vorticity distribution is no longer symmetric (see Figure 6.2). One of the vortices gets stronger while the other vortex of the opposite sign gets much weaker (compare to the $\alpha = 0^0$ case). Also, it seems that the larger vortex is actually composed of at least two vortices. In addition, two weak vortex layers of opposite signs are apparent on the pressure and suction side of the wing, respectively. This picture is much more clear in the plot for the $\alpha = 4^0$ case,

which is shown in Figure 6.3. Here the larger vortex is clearly composed of two smaller vortices. The smaller opposite sign vortex still exists. The two vortex layers are evidently stronger than in the previous case.

The axial vorticity contour for the $\alpha = 6^0$ case (Figure 6.4) looks slightly different from the cases presented above. The smaller vortex is still observed; however, it is much weaker than the larger vortex. Here the larger vortex looks more like a wing tip vortex although with careful observation a very small like-signed vortex can be seen inside the larger vortex. Also, the upper part of the suction side vortex layer breaks away from the rest of the layer.

Figure 6.5 and Figure 6.6 display the contour plots for the $\alpha = 8^0$ and $\alpha = 10^0$ cases, respectively. Here, the vortex layer on the low-pressure side of the wing disappears or almost disappears from the field of view. The larger vortex is no longer composed of two vortices. The smaller vortex still exists although it is much smaller than the larger vortex.

6.2.2 Streamwise Evolution of the Wing Tip Vortex

In this subsection, the axial vorticity distributions at several streamwise stations behind the wing are presented for the $\alpha = 4^0$ and $\alpha = 10^0$ cases. In each figure presented in this section, the $\alpha = 4^0$ case is shown in the upper part and $\alpha = 10^0$ case is shown in the lower part of the figure. To get a better understanding of the evolution of the tip vortex, vorticity fields at two additional streamwise stations, Z/C = 0.5 and Z/C = 1.5, are included.

The axial vorticity distributions at Z/C = 0.5 (behind the wing) for the two α cases are shown in Figure 6.7. For $\alpha = 4^0$ case, the two like-signed vortices inside the large vortex shown in Figure 6.3 are no longer seen. It seems that at this station the two vortices have merged into one single asymmetric vortex. Also, the "pressure side" vortex layer, present at Z/C = 0, has already rolled up into the main vortex. The smaller-opposite-signed vortex is no longer visible in the field of view. However, it must be remembered that the vorticity field shown here is computed from the average velocity field. The remaining part of the "suction side" vortex layer is still visible on the lower part of the plot. The axial vorticity field at this station for $\alpha = 10^0$ case is qualitatively different from the $\alpha = 4^0$ case. The vorticity contour still resembles that at Z/C = 0. The shear layer is still noticeable and the large vortex looks more elliptical.

At Z/C = 1, the shape of the contour lines, for $\alpha = 4^0$ case, in the core region is approximately circular while the shape of the contour lines in the outer region of the vortex is still asymmetric (Figure 6.8). Also, the opposite-signed vortex layer, which is depicted in previous figures, is no longer visible within the measurement plane. The contour for the $\alpha = 10^0$ case still looks very similar to that shown in Figure 6.7. Here, however, the vortex layer is thinner especially near the tip vortex. The wing tip vortices, in both cases, clearly rotates around the Z-axis, which can be observed by comparing the position and the shape of the vortices in Figure 6.8 with the previous figures in this subsection.

Figure 6.9 and Figure 6.10 show the contours of axial vorticity, for the two cases, at Z/C = 1.5 and Z/C = 2, respectively. Here, the shape vorticity contour for the $\alpha = 4^0$

case is more symmetric than before. For the $\alpha = 10^0$ case, more and more portions of the vortex layer roll up into the tip vortex.

At Z/C = 3, the rollup process for the $\alpha = 10^0$ case has stopped and an almost symmetric wing tip vortex has emerged, as depicted in Figure 6.11. For the $\alpha = 4^0$ case, the vortex is qualitatively similar to that at the previous station. The axial vorticity fields at Z/C = 4, shown in Figure 6.12, look qualitatively the same as that depicted in Figure 6.11.

Note that the color of the contour lines in the core region, for both cases, gets lighter (axial vorticity decreases) as Z/C increases, which shows the diffusion of the vorticity as the size of the vortex core increases (as shown in Chapter 5, the size of the vortex core increases while the total circulation stays constant as Z/C increases).

6.2.3 Vortex Core Trajectory

The location of the vortex center can be identified from the average axial vorticity field. By identifying the location of the vortex center, the vortex trajectory can be estimated. The vortex center is found by identifying the location of the peak vorticity in the core region. This method of identifying the vortex center works as long as the wing tip vortex is well defined. As shown in the previous subsection, the wing tip vortex is almost always well defined except for the low angle of attack cases, $\alpha = 2^0$ and 4^0 cases, at the trailing edge. In those two cases, the wing tip vortex (at Z/C = 0) is actually composed of two vortices of the same sign.

The locations of the peak vorticity for all α cases considered in this study are shown in Figure 6.13. Each type of symbol corresponds to an angle of attack case. For

each angle of attack case, the locations of the peak vorticity are given for data collected at a streamwise station of 0 to 4-chord lengths behind the wing. The number next to each data point corresponds to Z/C (streamwise location) at which the data is taken. Each of the dashed lines shown in the figure corresponds the image of the trailing edge of the wing for a given α case.

Data points corresponding to Z/C = 0 show that the locations of the peak vorticity for different angle of attack cases are approximately at the same spanwise location except for the $\alpha = 2^0$ case, where the peak vorticity is found at higher Y. As mentioned before, the wing tip vortex is not yet well defined at this station for $\alpha = 2^0$ case (see Figure 6.2). Therefore, the interpretation of that particular data point should be restricted to the location of the peak vorticity only and not the location of the wing tip vortex center.

For data points corresponding to other streamwise stations, however, the wing tip vortex core is already well defined for all α cases and the points can be interpreted as the location of the center of the tip vortex. As shown in Figure 6.13, the vortex moves inwards (away from the tip toward the root) with increasing Z/C, for all α cases considered in this study. The movement of the vortex in the X direction is different, however, for the lower and the higher angle of attack cases. For the low angle of attack case ($\alpha = 2^0$ and $\alpha = 4^0$), the location of the vortex center fluctuates from one X direction to another as Z/C increases. On the other hand, the vortex center clearly moves downward (toward negative X direction) with increasing Z/C, for $\alpha = 6^0$, 8^0, and 10^0 case.

The inward and downward movement of the wing tip vortex with increasing downstream distance from the wing is similar to the movement observed in a pair of

trailing vortex systems (full wing case). The inward movement is due to the interaction between the wing tip vortex and part of the negative vortex layer which still in the process of rolling up into the tip vortex. This movement stops when the rollup process is completed (e.g., at Z/C = 1 for the lower angle of attack cases). The downward movement observed in this case (the half wing case) is the result of the interaction of the tip vortex with its image.

6.3 Instantaneous Vorticity Distributions

The contour plots presented in Section 6.2 reveal the presence of vortices of opposite signs at the trailing edge of the wing. Downstream of the wing, only like-signed vortices are observed. Obviously, vortices of opposite signs cannot merge. So the disappearance of the other vortices is because they somehow either move outside the measurement plane or remain present but fade away in the averaging process -or a combination of the two. This can be confirmed by considering the instantaneous axial vorticity fields. Also, the instantaneous information helps us understand the interactions between these vortices.

The typical instantaneous vorticity fields at Z/C = 0 for the $\alpha = 4^0$ case are shown in Figure 6.14. The instantaneous plots look very similar to the average vorticity plot presented in Section 6.2. The two like-signed vortices that make up the larger vortex are clearly observed. The difference between this figure and that shown in the last section is the "cat-eye" pattern in the vortex layers, which is not clearly observed in the average vorticity fields. The vortex layer, on the suction side of the wing, looks almost ready to break up into smaller structures.

The evidence of the breaking up of the vortex layer on the suction side is even more clear for the $\alpha = 8^0$ case (Figure 6.15). The suction-side vortex layer is not observed within the field of view in the average vorticity contour shown in the last section. However, the instantaneous vorticity fields at the trailing edge, for this case, indicate that the vortex layer actually breaks up into smaller vortices, which scatter around the main vortex. Notice that there are more "positive vortices" scattered near the main vortex in the $\alpha = 8^0$ case than in the $\alpha = 4^0$ case (the color bar used is the same in both figures). Also, the "cat-eye" pattern in the pressure-side vortex layer is now more evident.

Farther downstream, the smaller vortices continue to satellite around the main vortex. Figure 6.16 shows typical instantaneous vorticity fields, for the $\alpha = 4^0$ case, at 4-chord-length behind the wing. The plots show the main vortex is surrounded by several vortices, mostly of opposite sign. One of the snapshots (e.g., the plot on the upper right corner of Figure 6.16) demonstrates that one of these vortices is comparable in strength to the main vortex. In two of the plots shown in Figure 6.16, two like-signed vortices are observed inside the main vortex. This indicates that, sometimes, the two vortices still have not yet merged at this station. However, they do not appear quite often, even at Z/C = 1. (They appear only in a few instantaneous fields among the 200 fields.) In most cases, the main vortex is composed of only a single vortex.

The situation for the higher angle of attack case is quite similar. Downstream from the wing, the main tip vortex is surrounded by several vortices of opposite sign. Examples for the higher α case are shown in Figure 6.17, where four instantaneous vorticity fields at Z/C = 4 are plotted for the $\alpha = 8^0$ case. Again, as in the $\alpha = 4^0$ case,

one relatively strong satellite vortex emerges. It is important to note that the strength of this relatively strong satellite vortex is approximately the same as that in the $\alpha = 4^0$ case. Also, in this case the relatively strong satellite vortex appears paired with another satellite vortex whose sign is the same as the main vortex. For the high angle of attack cases, whenever the relatively strong satellite vortex is visible within the field of view, it almost always appears in a pair.

In general, the main tip vortex is surrounded by several satellite vortices. The signs of most of these satellite vortices are opposite that of the main vortex. In some of the instantaneous vorticity plots, at least one relatively strong satellite vortex emerges. This strong satellite vortex can be in any location around the wing tip vortex (its location is not fixed). In some α cases, the emergence of this strong satellite vortex is almost periodic. Examples of this are shown in Figure 6.18 and Figure 6.19 where eight sequential instantaneous vorticity fields for the $\alpha = 2^0$ case are plotted (at Z/C = 3). A pair of vortices of opposite sign, comparable in strength and size, is observed on the upper left plot of both figures. The rest of the plots shown on both figures show some resemblance.

The satellite vortices of different sign obviously induce a velocity field, which in turn causes the wing tip vortex to move around (i.e., it fluctuates). The strength of the wing tip vortex is considerably increased at higher α. On the other hand, the strength of the satellite vortices only varies slightly. In this case, the velocity field, induced by the satellite vortices, does not strongly influence the motion of the main vortex as in the lower angle of attack case. Therefore, it is expected that the unsteadiness of the wing tip vortex decreases with the angle of attack. However, the unsteadiness may also depend on

the position of the smaller vortices. If they are too far from the primary wing tip vortex, their induced velocity may be too small to influence the motion of the main vortex.

6.3.1 Instantaneous Core Location

As mentioned before, the existence of smaller satellite vortices should have some effects on the motion of the wing tip vortex. The effectiveness of the satellite vortices to cause the unsteadiness of the main vortex can be detected by observing the path followed by the wing tip vortex in each instant. The instantaneous position of the wing tip vortex is found by identifying the location of its center. The method of identifying the location of the core is the same as described in Section 6.2.3. For each PIV realization, the location of the core of the instantaneously captured main vortex was identified.

The results are shown in Figure 6.20, where the instantaneous locations of the vortex center are presented for the $\alpha = 4^0$ and $\alpha = 8^0$ cases. For each plot in the figure, the crossflow plane is located at a particular streamwise station. Each data point is normalized by the average location of the vortex center for the corresponding case, which is presented in Section 6.2.3. (For each case, point (1,1) corresponds to the average position of the vortex center.) The figure shows that at each downstream station, the level of unsteadiness of the wing tip vortex is higher for the $\alpha = 4^0$ case.

In general, the level of unsteadiness is higher for the low angle of attack case. This can be seen from the plot of the rms of radial distance from the average position ($\mathbf{r}$-$\mathbf{r}_{avg}$) vs. Z/C, shown in Figure 6.21. In the figure, the Y-axis is normalized by the chord length. Each symbol represents data points for a particular α case. As exhibited in the figure, the radial fluctuation can be as high as 8% of the chord length for the low angle of

attack case ($\alpha = 2^0$, Z/C = 4). For most of the data, the radial fluctuations are in the range of 1 to 4% of the chord length (C = 9.1 cm). Note that the diameters of the vortex core are in the range of 1 to 2 cm (see Chapter 5).

As can be seen from Figure 6.21, there is no general trend of decreasing or increasing fluctuations with increasing Z/C for a given α case. The radial fluctuations for the higher angle of attack cases are approximately constant over the range of the streamwise station considered. As shown in Chapter 5, the total circulation for these cases is also approximately constant. On the other hand, at a given streamwise station, the fluctuations do not always decrease with increasing angle of attack, even though the strength of the wing tip vortex clearly increases with increasing α. Therefore, there seems to be no direct link between the strength of the trailing vortex and the unsteady motion of the trailing vortex. (The stronger tip vortex is not always more steady than the weaker tip vortex.) However, there seems to be a correlation between the level of fluctuation and the frequency of appearance of the strong satellite vortices in the field of view. For example at Z/C = 5, the fluctuations are higher for the $\alpha = 10^0$ case than for $\alpha = 8^0$ or $\alpha = 6^0$. It is also observed that the strong satellite vortices appear more frequently within the field of view in the $\alpha = 10^0$ case than in $\alpha = 8^0$ or $\alpha = 6^0$. This indicates that in the case when the field, produced by the system of vortices, is such that the strong satellite vortices frequently move closer to the main vortex, the level of fluctuations is higher.

6.4 Summary

In this chapter, the interactions between vortices produced by the wing are examined. Both average and instantaneous axial vorticity fields, at various streamwise locations behind the wing, are presented. The average trajectories of the wing tip vortex in the crossflow plane, for all cases considered in this study, are revealed. The level of fluctuation of the wing tip vortex position is examined.

A brief listing of important results presented in this chapter is as follows:

1. Vortices of various sign are observed at the trailing edge of the wing. A smaller vortex, with an opposite sense of rotation, is observed next to the main vortex. Two opposite sign vortex layers, one on each side of the wing, are detected in the low angle of attack cases. One of the layers (the one on the suction side) breaks up into smaller vortices when the wing incident is set at a higher angle of attack.
2. Downstream of the wing, only the rolling up of the pressure-side vortex layer into the main vortex is observed in the average fields. The vortices, with signs opposite to the main vortex, are not detected in the average fields.
3. The instantaneous fields reveal that the main vortex is surrounded by several satellite vortices. The sign of most of these satellite vortices is opposite that of the main vortex. At least one relatively strong satellite vortex appears in some of the instantaneous fields. For the high angle of attack case this strong satellite vortex appears paired with another vortex of opposite sign in some of the instantaneous fields.
4. There is some evidence to suggest that the unsteadiness of the motion of the wing tip vortex depends on the "orbital path" of the strong satellite vortices.

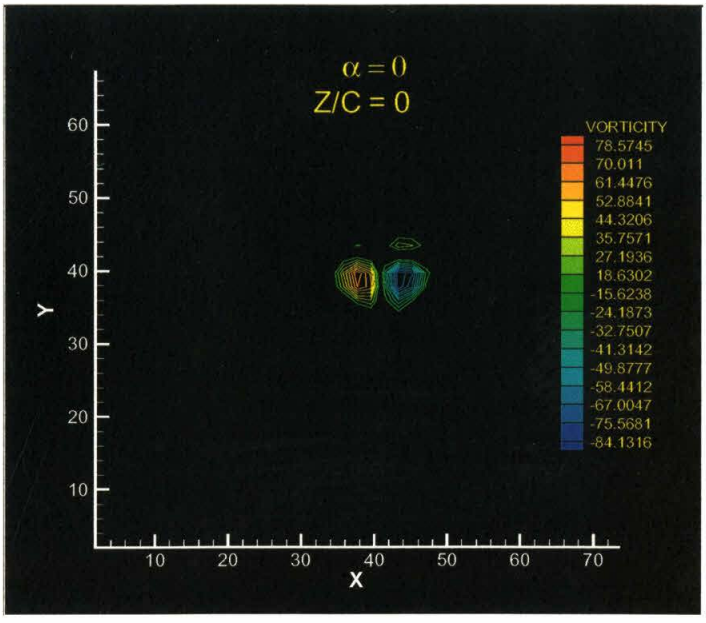

Figure 6.1. Axial vorticity field, $\alpha = 0^0$, Z/C = 0

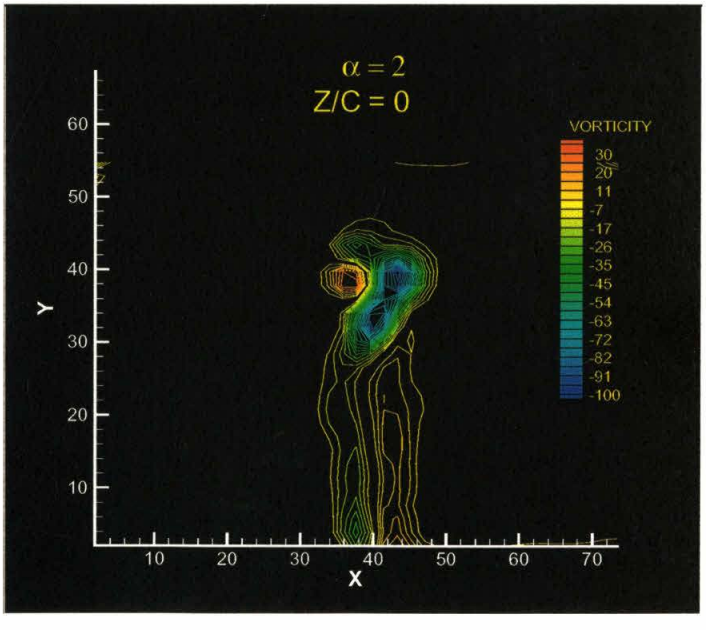

Figure 6.2. Axial vorticity field, $\alpha = 2^0$, Z/C = 0

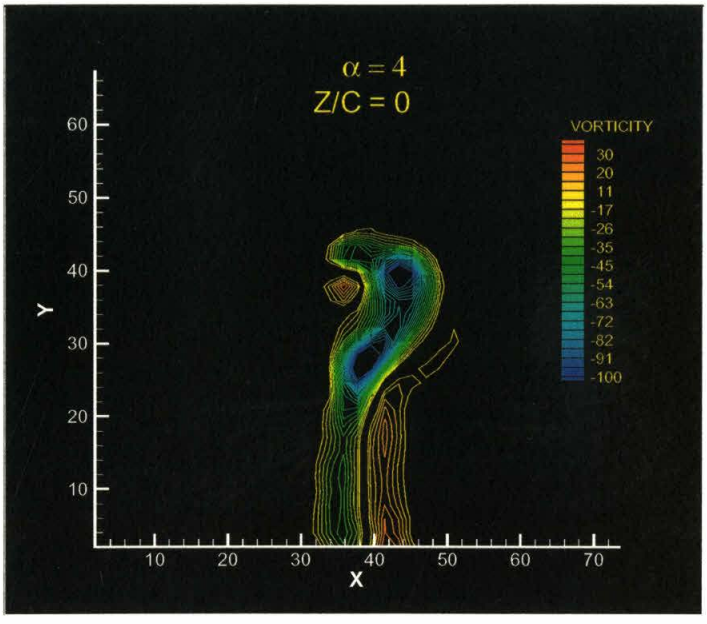

Figure 6.3. Axial vorticity field, $\alpha = 4^0$, Z/C = 0

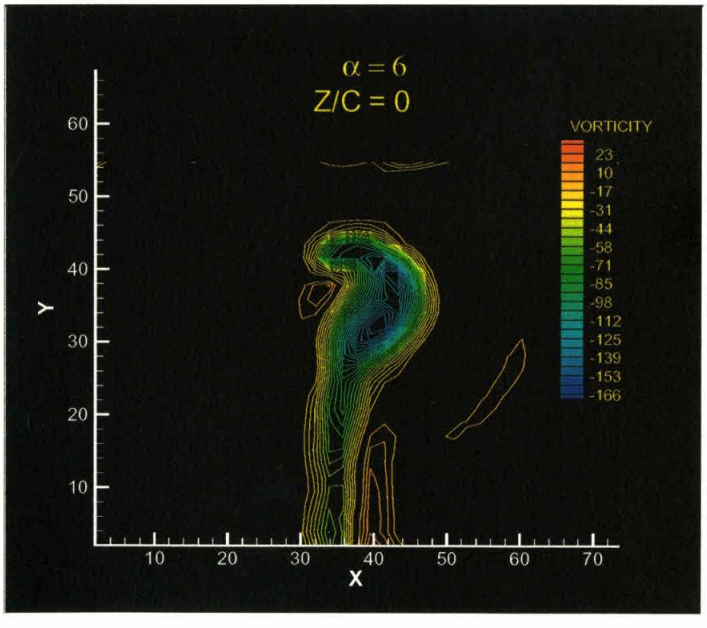

Figure 6.4. Axial vorticity field, $\alpha = 6^0$, Z/C = 0

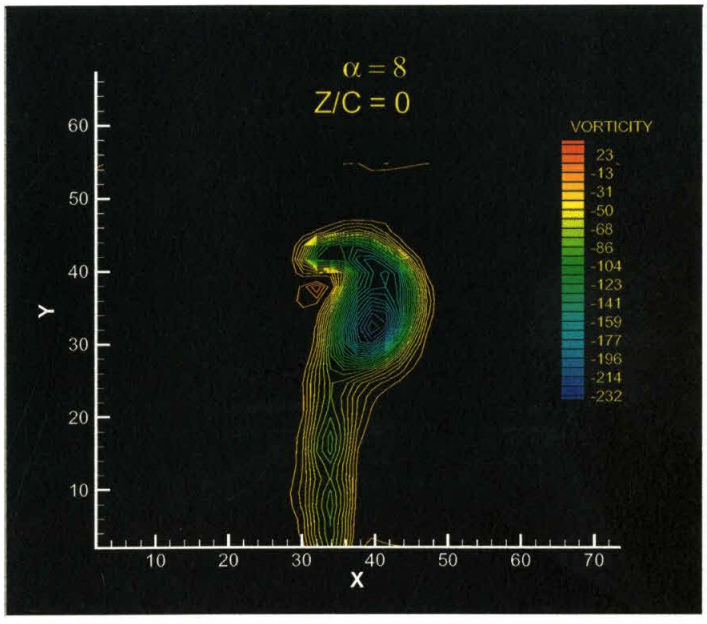

Figure 6.5. Axial vorticity field, $\alpha = 8^0$, Z/C = 0

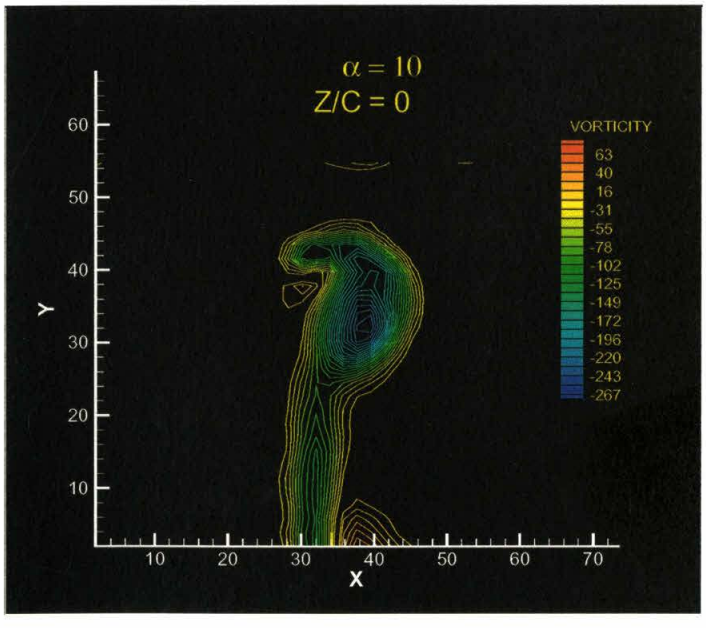

Figure 6.6. Axial vorticity field, $\alpha = 10^0$, Z/C = 0

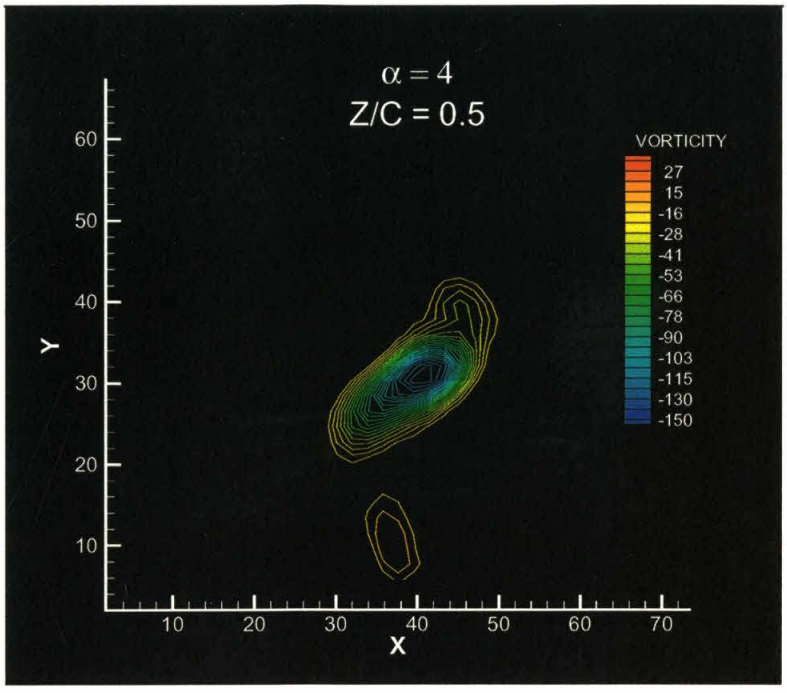

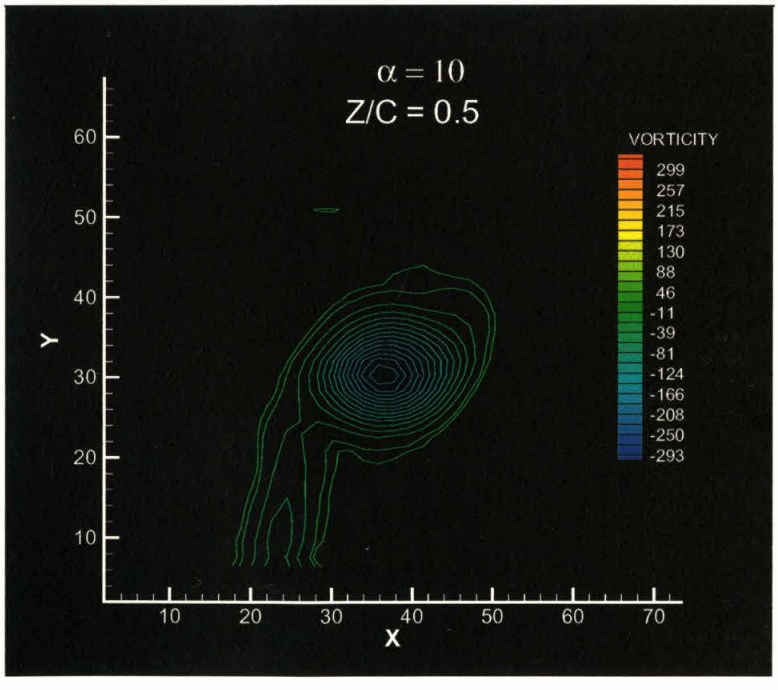

Figure 6.7. Axial vorticity fields at Z/C = 0.5

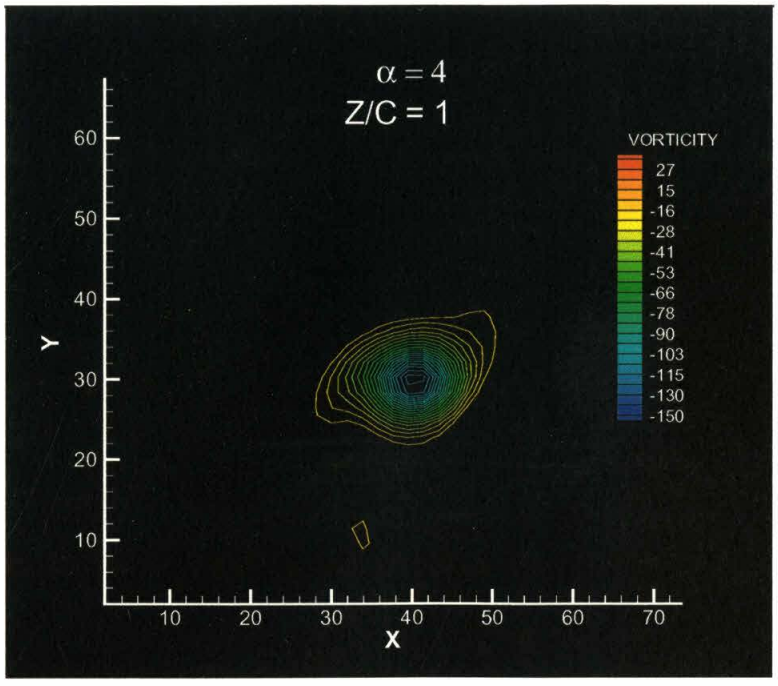

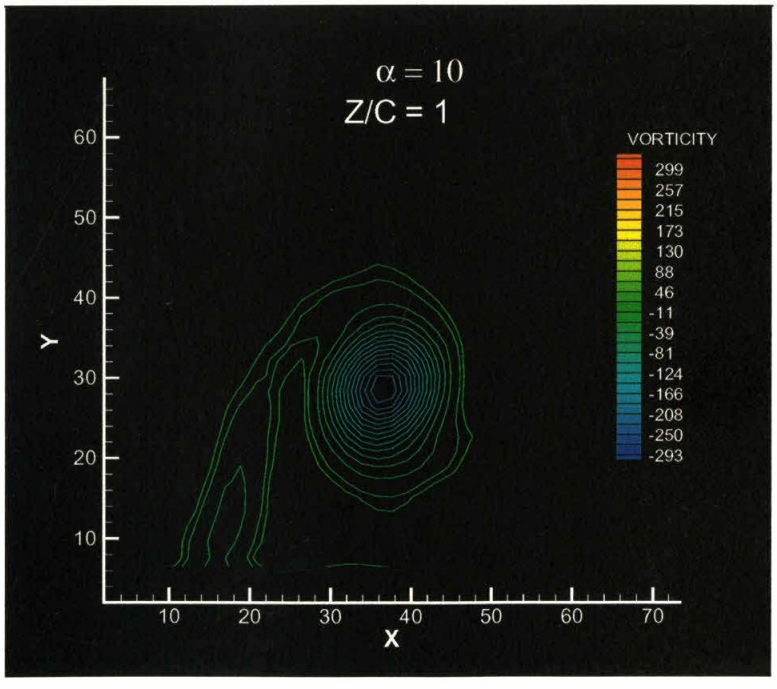

Figure 6.8. Axial vorticity fields at Z/C = 1

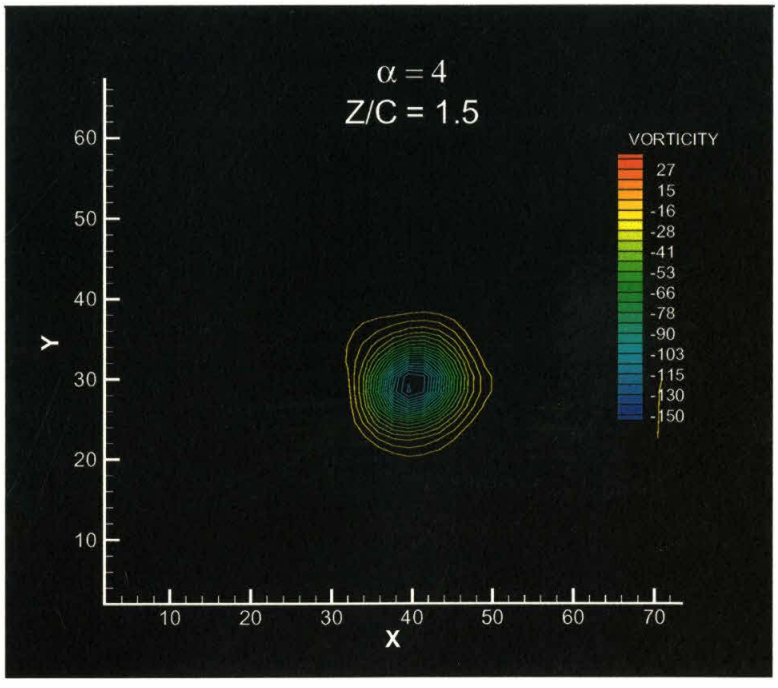

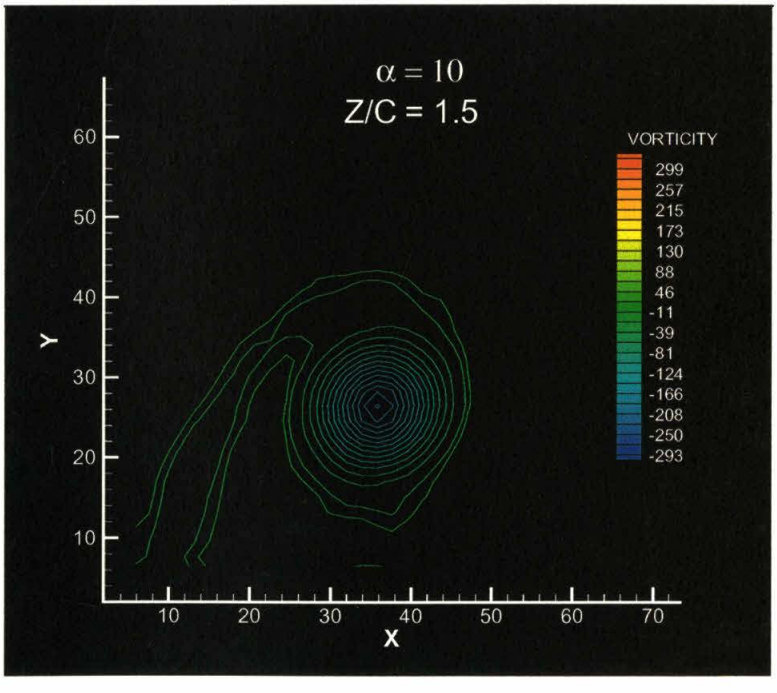

Figure 6.9. Axial vorticity fields at Z/C = 1.5

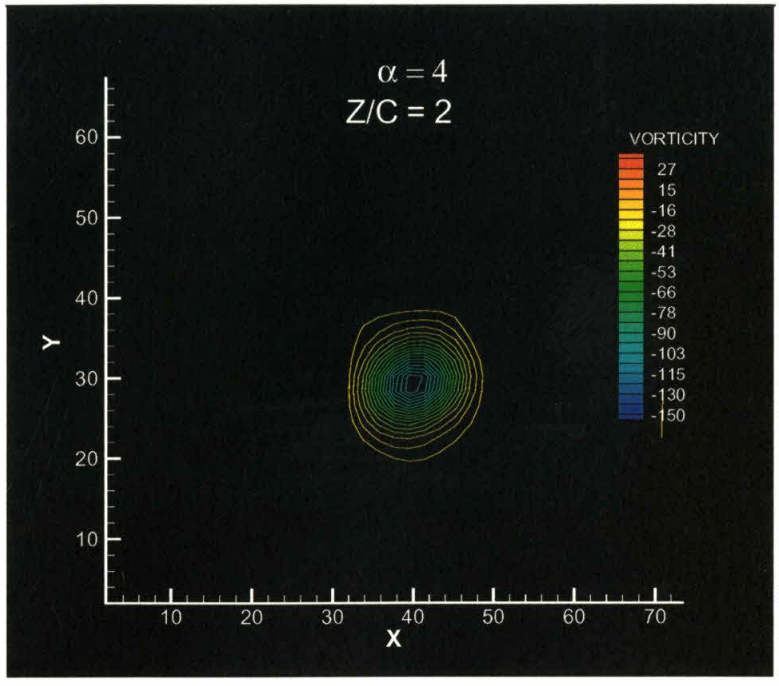

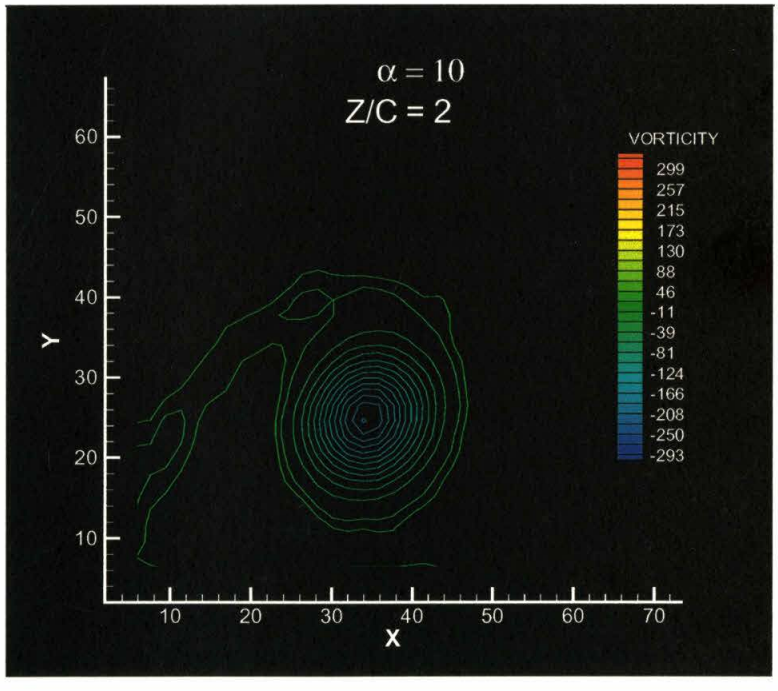

Figure 6.10. Axial vorticity fields at Z/C = 2

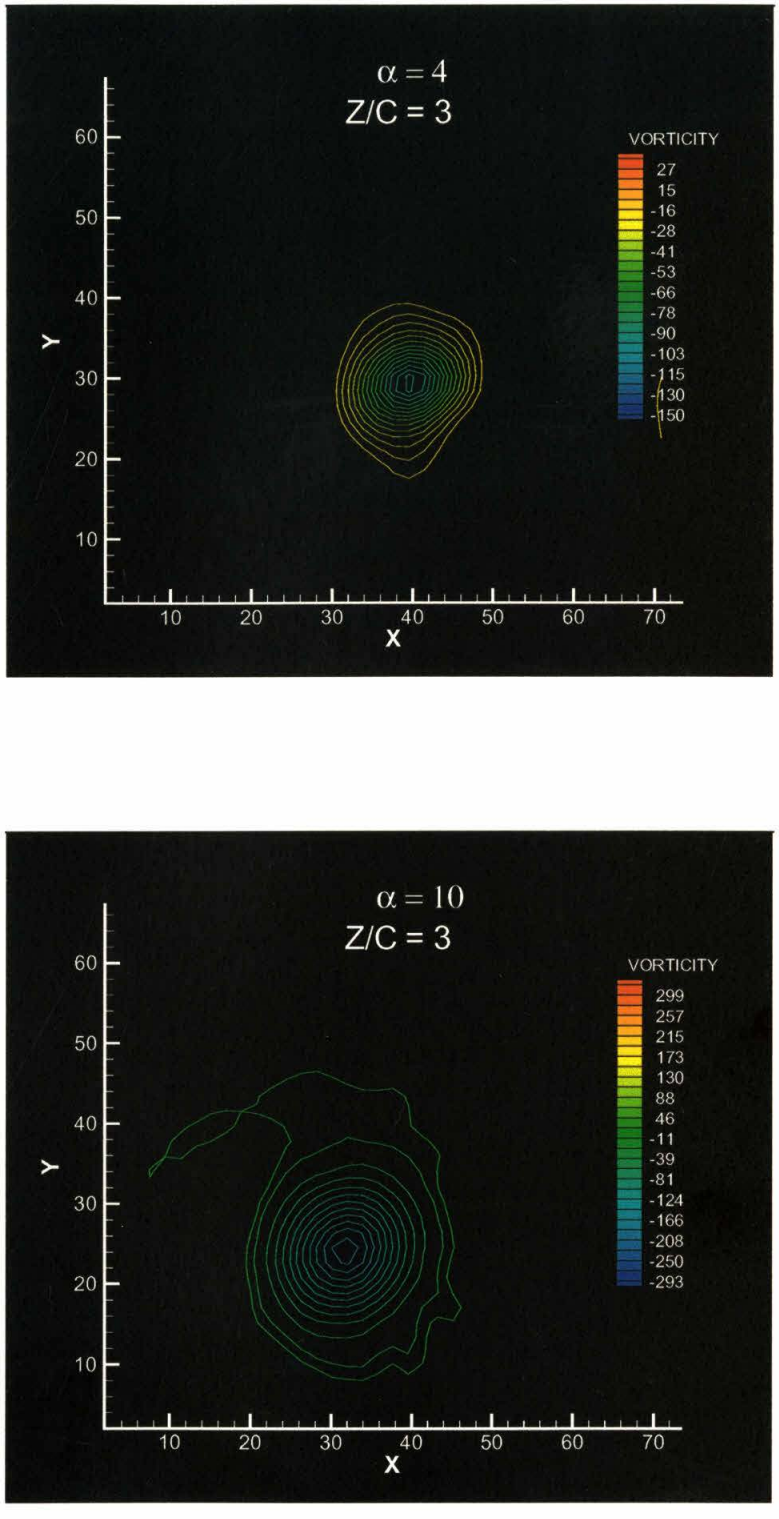

Figure 6.11. Axial vorticity fields at Z/C = 3

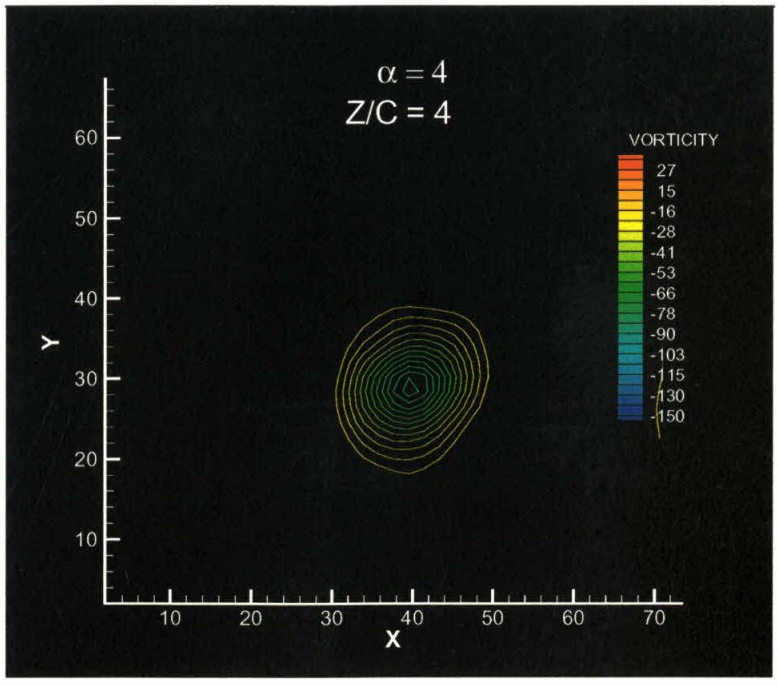

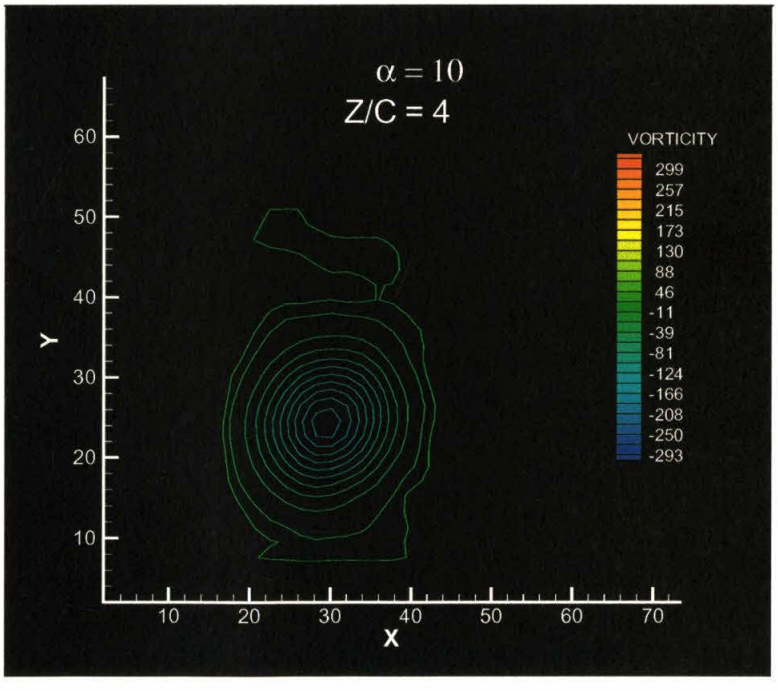

Figure 6.12. Axial vorticity fields at Z/C = 4

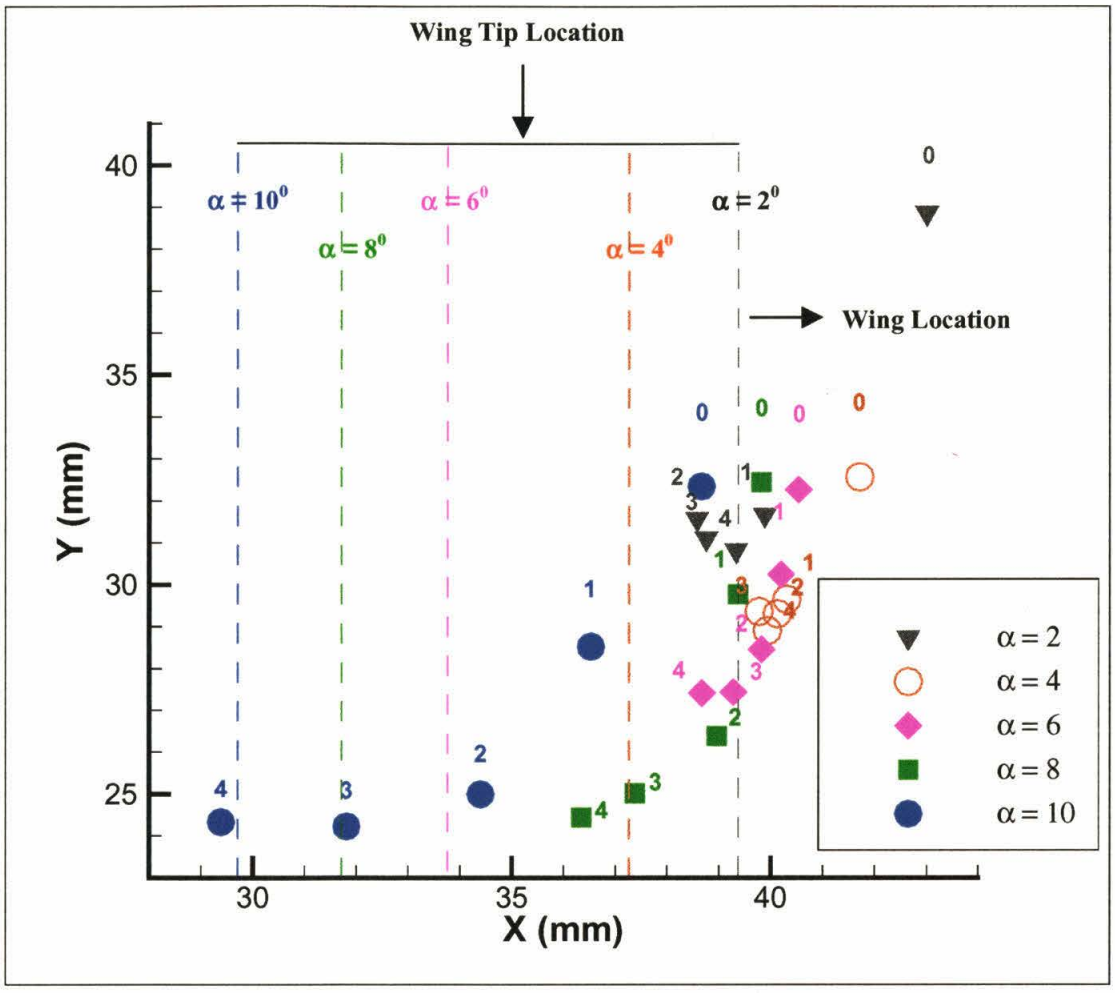

Figure 6.13. Average core trajectories

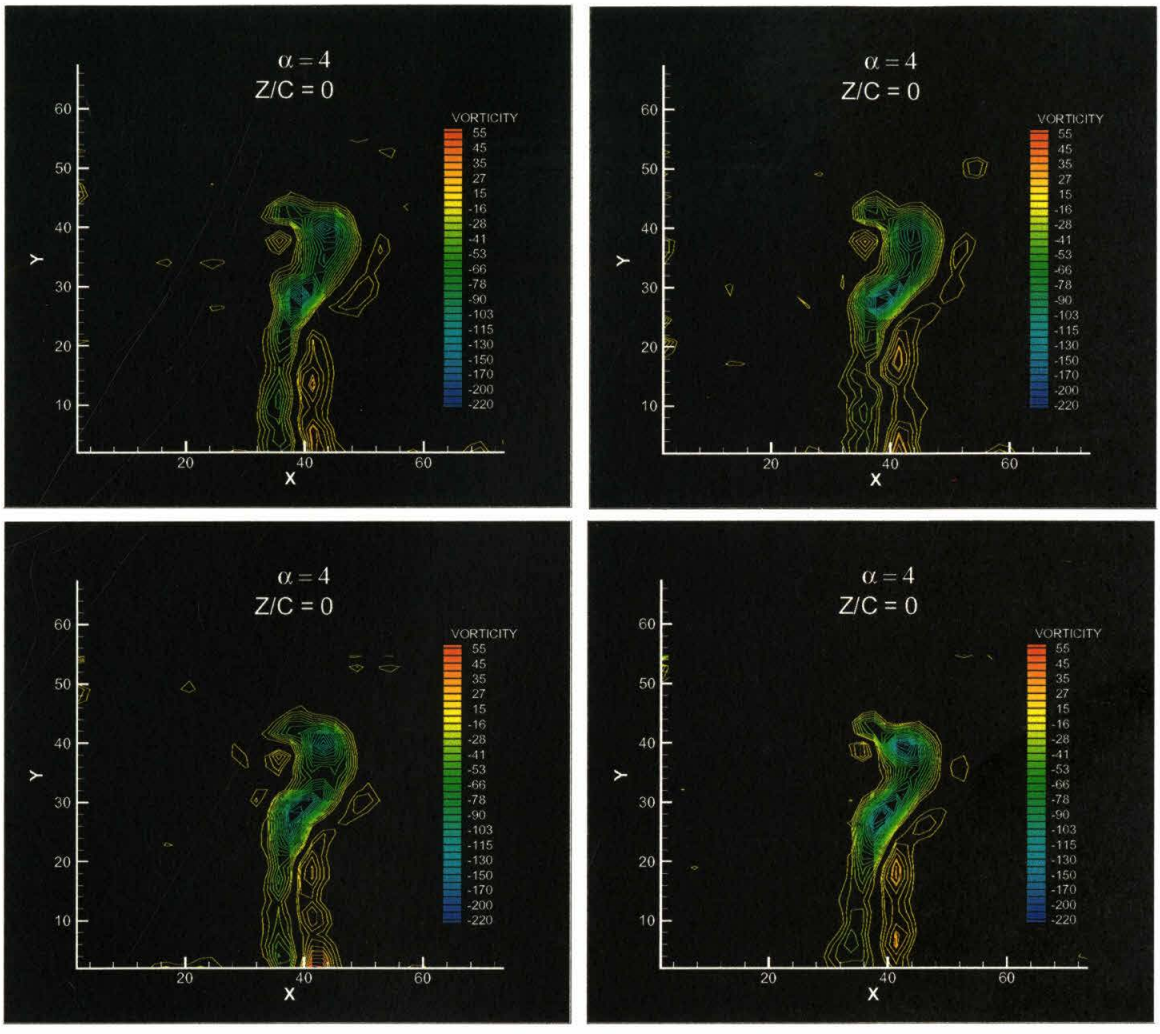

Figure 6.14. Instantaneous vorticity fields, $\alpha = 4^0$, Z/C = 0

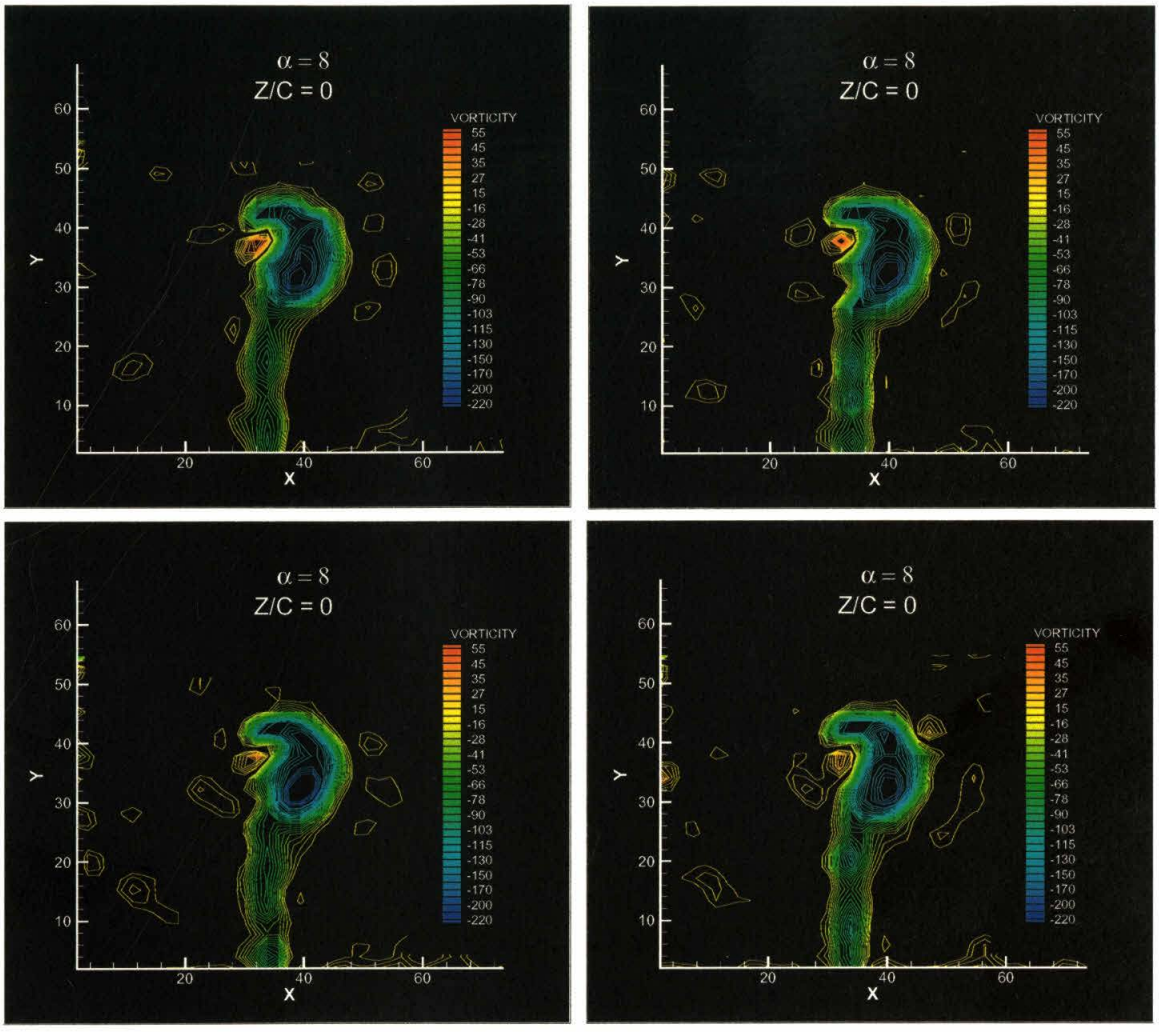

Figure 6.15. Instantaneous vorticity fields, $\alpha = 8^0$, Z/C = 0

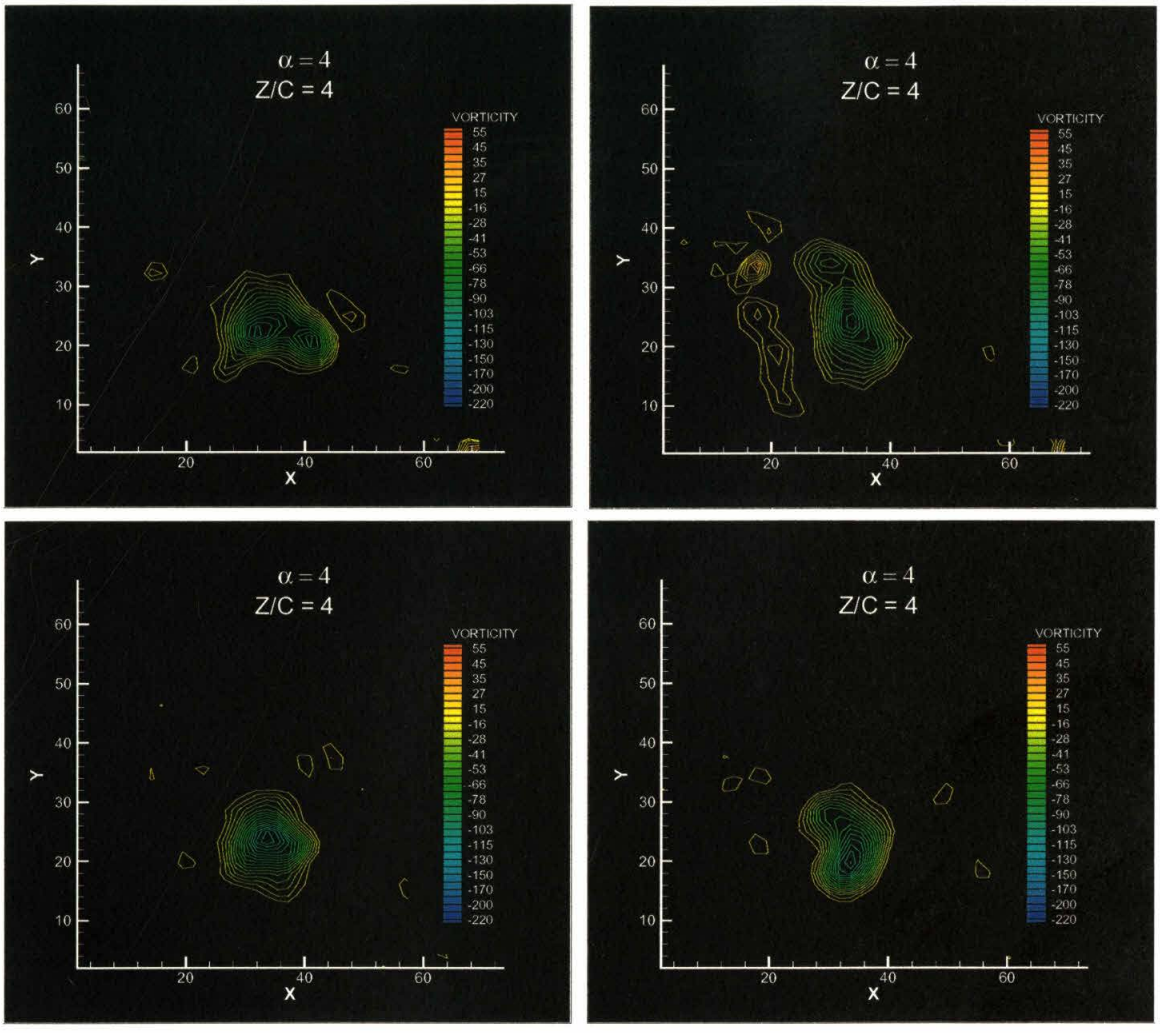

Figure 6.16. Instantaneous vorticity fields, $\alpha = 4^0$, Z/C = 4

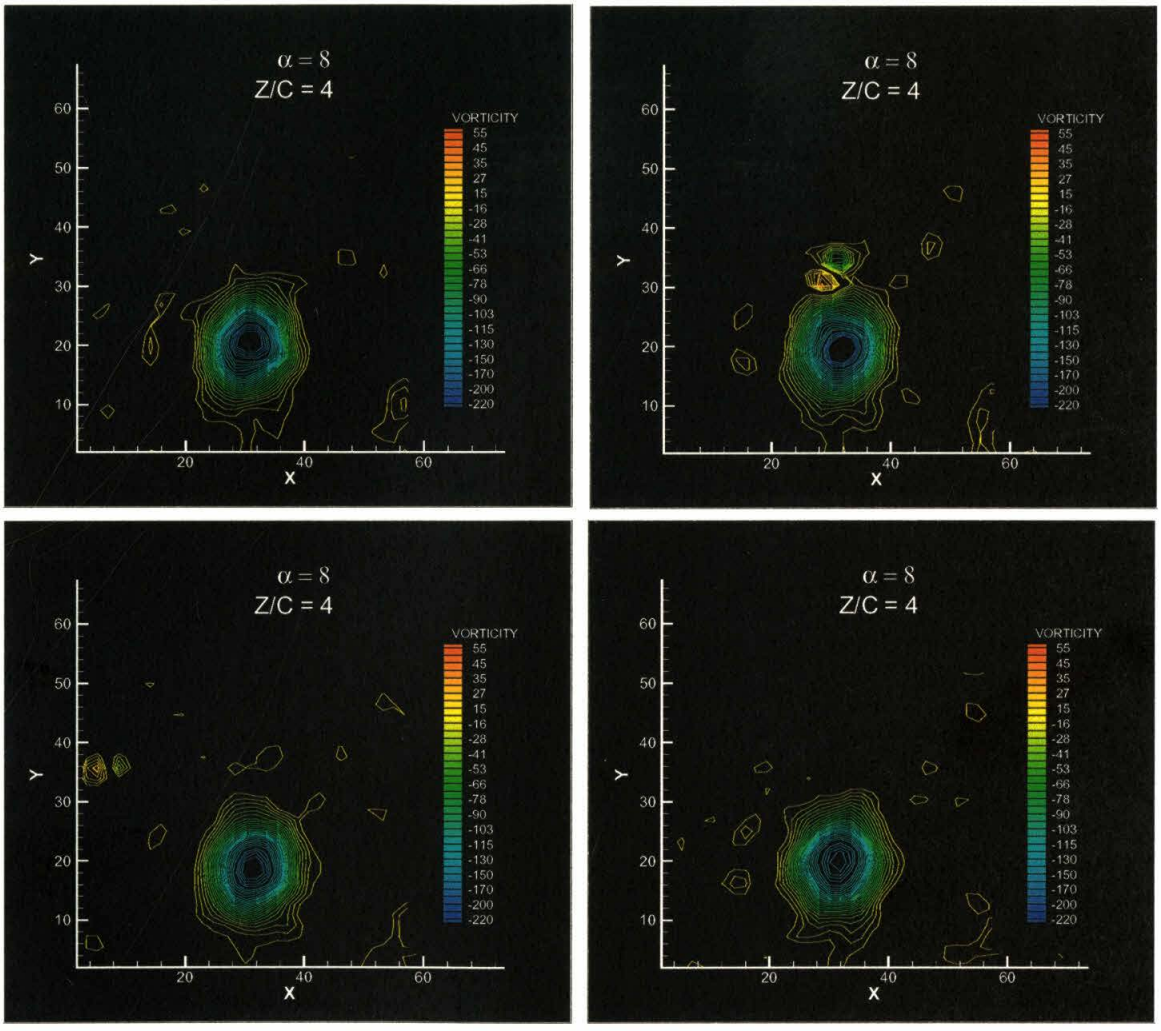

Figure 6.17. Instantaneous vorticity fields, $\alpha = 8^0$, Z/C = 4

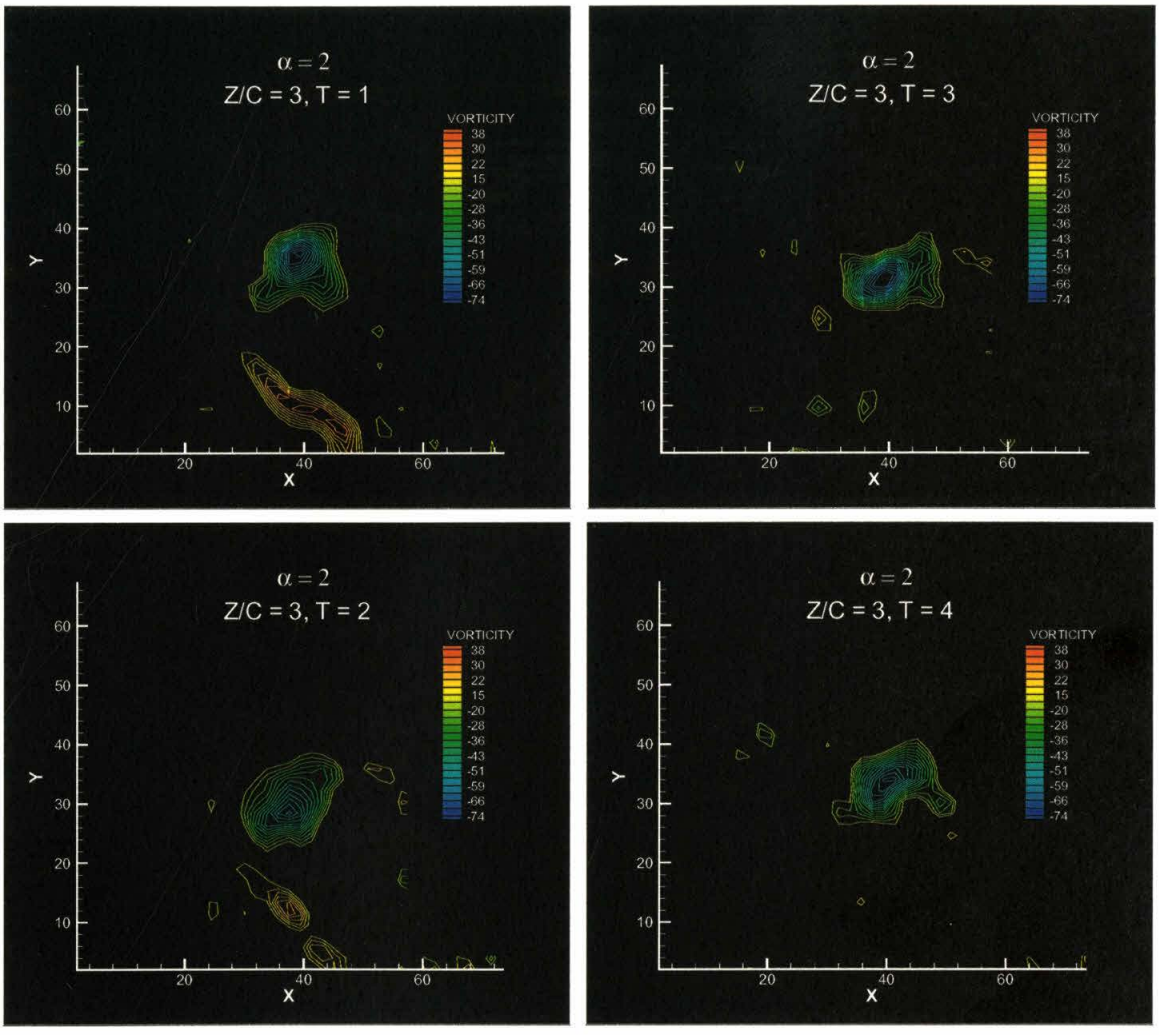

Figure 6.18. Instantaneous vorticity fields, $\alpha = 2^0$, Z/C = 3

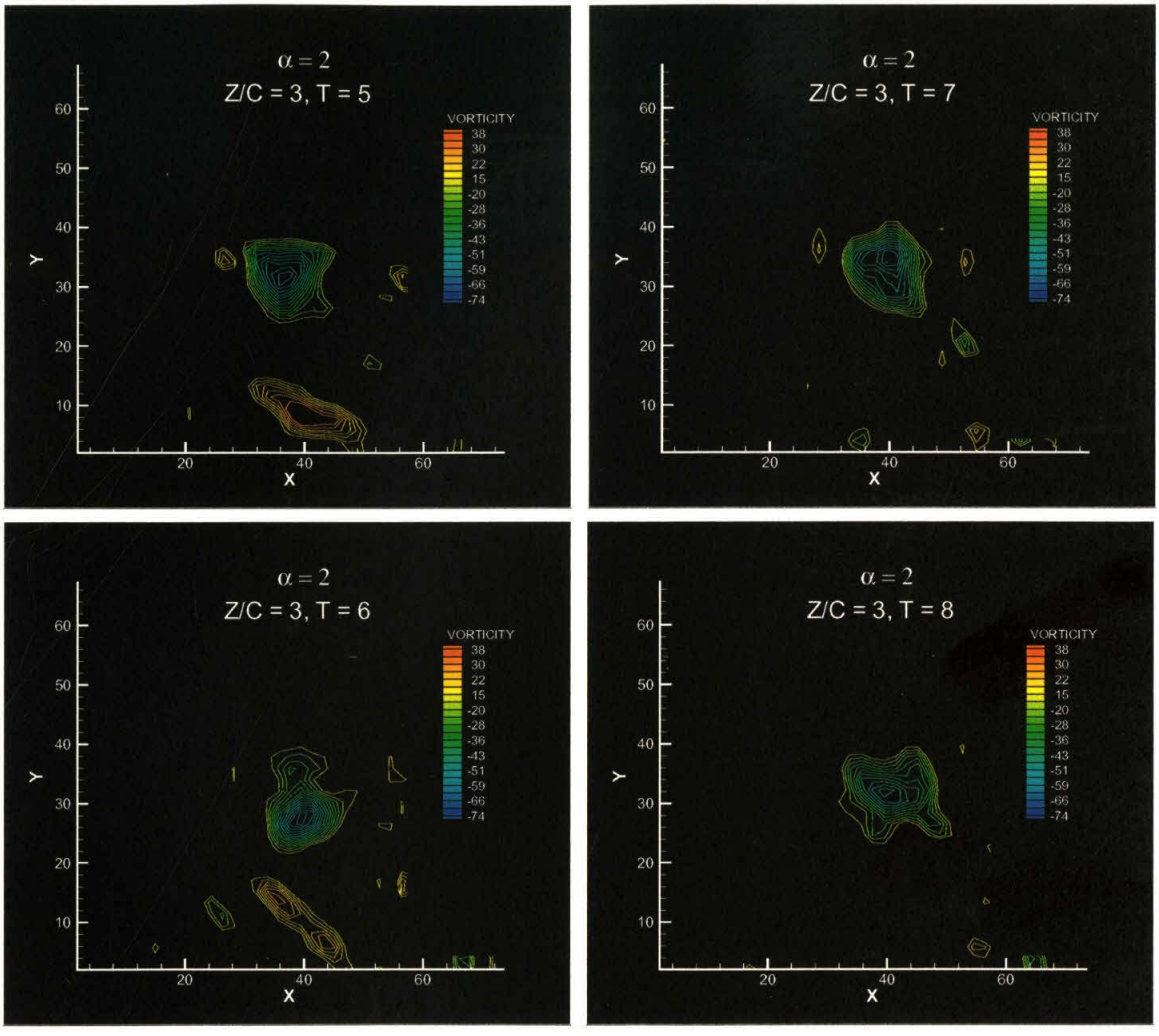

Figure 6.19. Instantaneous vorticity fields, $\alpha = 2^0$, Z/C = 3

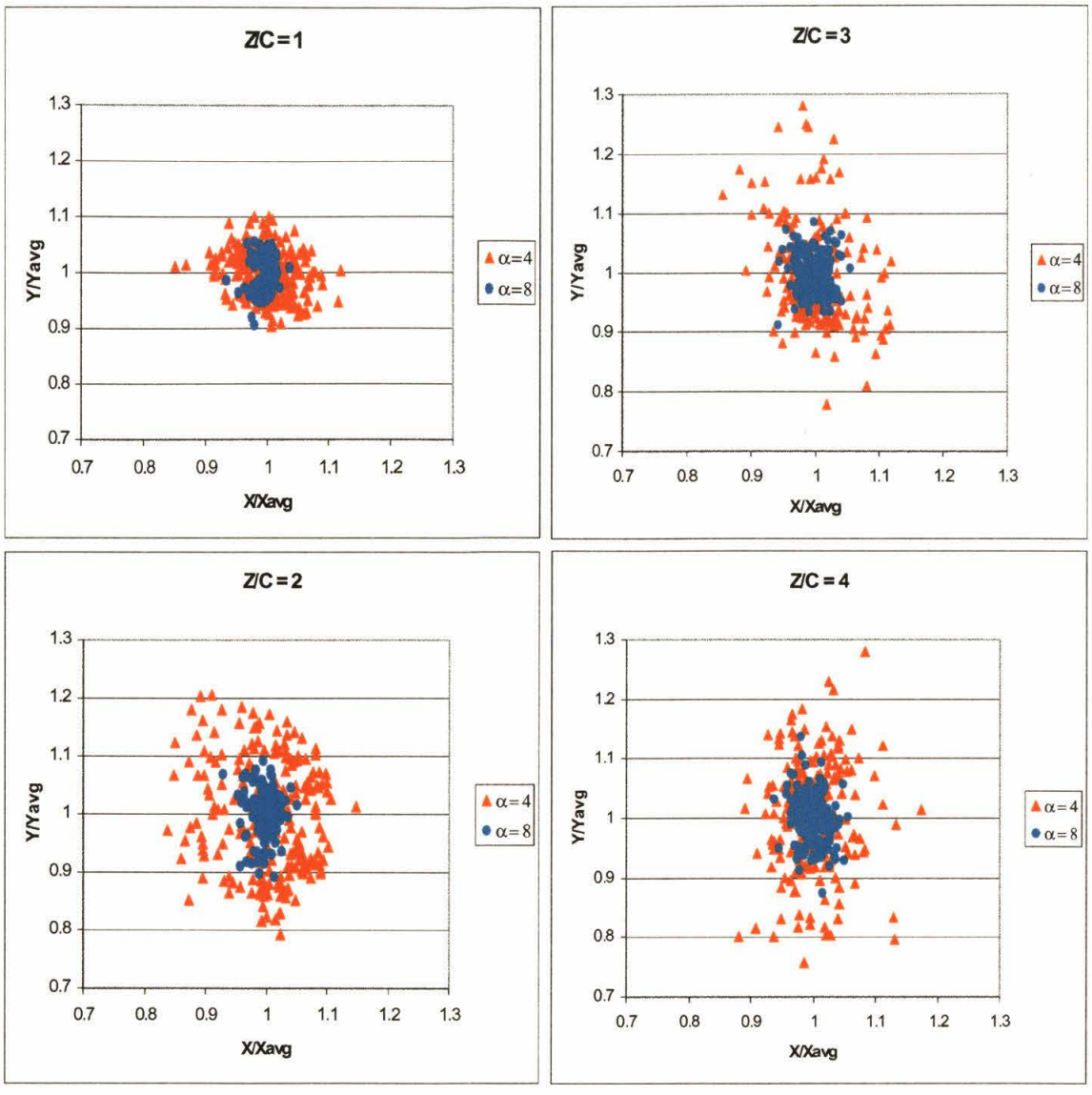

Figure 6.20. Instantaneous locations of the vortex core

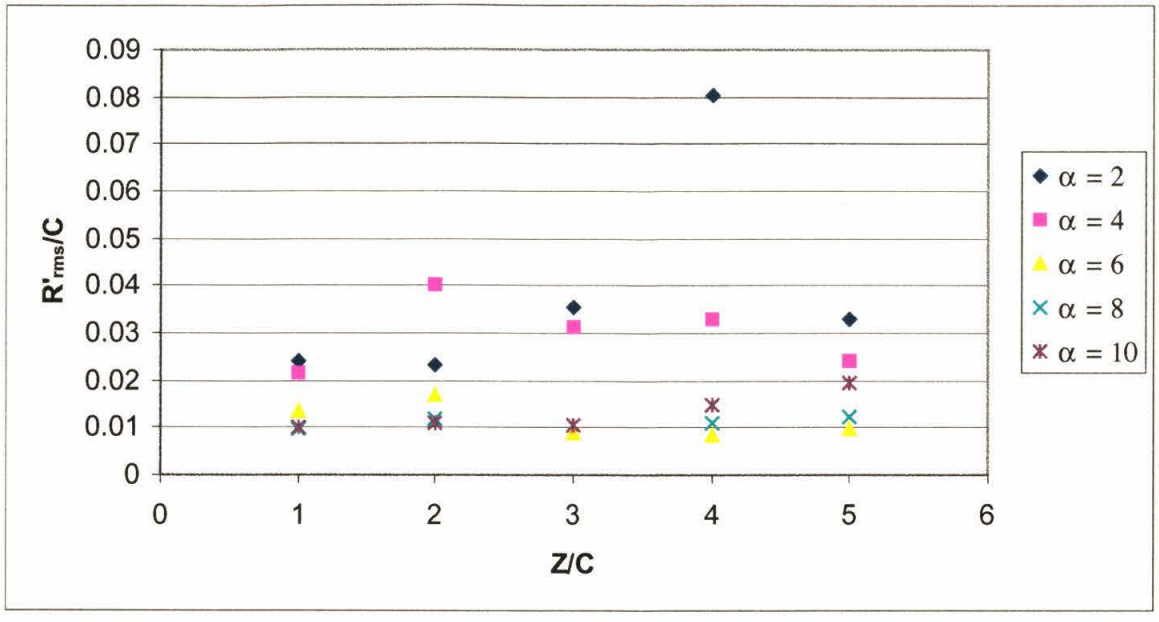

Figure 6.21. Rms vs. Z/C

CHAPTER 7

Formation of the Wing Tip Vortex

7.1 Introduction

In the preceding chapter, we presented the axial vorticity fields at the trailing edge of the wing. The axial vorticity fields, for all α cases, reveal the existence of several regions of concentrated vorticity. The vorticity observed at the trailing edge is obviously produced somewhere on the wing surface. To trace the origin of these vortices, a set of planar DPIV measurements was performed in several crossflow planes intersecting the wing surface.

The results of the measurements are presented in this chapter. The experimental conditions at which the measurements were made are described in the next subsection. Next, the results for the $\alpha = 0^0$ and $\alpha = 4^0$ cases are presented and discussed.

7.2 Experimental Conditions

For reasons mentioned in Chapters 2 and 3, 2D DPIV is used in the present experiments to measure velocity fields around the wing tip. The schematic showing the position of the light sheet with respect to the wing is depicted in Figure 7.1. The velocity measurements are taken at 5 streamwise stations. The locations are approximately as follows: right ahead of the leading edge, between the leading edge and the point where

thickness of the airfoil is maximum, the point where thickness of the airfoil is maximum, middle of the chord, and near the trailing edge. Data is taken at two different angles of attack: 0^0 and 4^0. As in the previous experiment, the freestream velocity of the wind tunnel is set at 1.5 m/s. This corresponds to a Reynolds number, based on the chord length of the wing model, of approximately 9040.

It is worth to mention that the position of the measurement plane with respect to the wing is not the same as in the previous experiment. In order to focus on the tip region, the measurement plane in the current experiment is moved slightly outboard. (It is located at higher Y with respect to the origin of the coordinate system used in the previous experiment.) Therefore, the coordinate points, shown in the figures presented in this chapter, are not the same as those in the previous chapter.

7.3 Velocity and Vorticity Fields Around the Wing Tip

In this section, average velocity and vorticity fields are presented. Each average velocity field is computed from 200 instantaneous fields, using the first method described in Section 4.3. The mean vorticity fields are computed from the corresponding average velocity fields. Again, only in-plane velocity components can be obtained from 2D DPIV measurements.

A rectangular box is drawn in each of the plots presented in this section. This box corresponds approximately to the surface of the wing model as viewed from the camera. As mentioned in Chapter 3, the measurement plane is viewed with a camera that is basically located downstream of the wing. Due to the thickness of the airfoil and the position of the wing when it is set at some angle of attack, the rectangular box in most

cases does not correspond to the actual profile of the wing surface at that particular measurement station. Also, the rectangular box is drawn slightly larger than the actual wing surface as seen from the camera.

In each figure, the velocity field is shown on the top while the vorticity field is shown on the bottom part of the figure. The colorbar legend for vector plots (velocity fields) given in this section is with respect to the total in-plane velocity magnitude.

7.3.1 $\alpha = 0^0$ Case

The five streamwise locations, at which PIV measurements were made for $\alpha = 0^0$ case, are shown in Figure 7.2. As shown in the figure, the letter N labels each of the streamwise locations at which the measurements were made.

The first set of measurements is taken at the leading edge of the wing. At the leading edge, the pressure is higher (stagnation point) than in any other regions. Therefore, fluid near the wing surface would have a tendency to move away from the leading edge toward a region of lower pressure. Figure 7.3 shows the average in-plane velocity and axial vorticity fields at this station. As can be seen in Figure 7.3, the velocity vectors point away from the wing in the entire field of view. This in-plane motion is symmetric with respect to the wing. The magnitude of the in-plane velocity is higher in the region surrounding the wing surface. In the lower region of the velocity vector field, the vectors are pointing outward (in the X direction) as the fluid follows the shape of the wing surface and the flow is two-dimensional in the XZ plane. On the tip surface, the vectors are pointing outboard (along the positive Y direction). Near the tip corners, there is a transition region, where the directions of the velocity vectors change from pointing along the X-axis to the Y-axis. This three-dimensional flow in the

transition region is generated by the pressure gradient between the airfoil and the tip surfaces. The corresponding vorticity field shows two opposite-signed vortices on each side of the wing surface ("pressure" and "suction" side of the wing) near the tip corner, where the velocity vectors change their directions.

The mean in-plane velocity field at a streamwise station of 1 cm behind the leading edge is shown in Figure 7.4. Here, the vector field looks qualitatively similar to that at the leading edge. Notice that the magnitude of this in-plane motion is lower than that at the leading edge, in particular in the region above the tip. In fact, above the tip the in-plane velocity is practically zero. At this station, the strength and the size of the two opposite-signed vortices have increased, as shown in the vorticity contour.

The in-plane motion is significantly reduced at the streamwise station corresponding to the place where the airfoil section reaches its maximum thickness (Figure 7.5). Here, only very small in-plane motion is detected everywhere. Looking at the shape of the airfoil at this station, the flow is expected to be almost perpendicular to the plane of the light sheet. There is still a small velocity gradient on each side of the wing surface near the tip corner. The two opposite-signed vortices are still observed in the vorticity plot. However, they are not as strong as in the preceding streamwise station.

The flow near the wing seems to change direction at the mid-chord (Figure 7.6). Here, vectors near the wing are pointing inboard parallel to the wing surface, indicating a small in-plane motion toward the root of the wing. The two vortices, observed earlier, are no longer detected in the corresponding vorticity field.

The average in-plane motion near the trailing edge is shown in Figure 7.7. At this streamwise station, the in-plane flow is seen to be coming from the region "above" the tip

toward the wing root (inboard). Relatively strong circulating motion is visible in the region near the tip. The corresponding vorticity field exhibits two opposite-signed vortices. However, the sign of these vortices is just the opposite of the sign of the two vortices observed at earlier stations. This is the counter-rotating pair of vortices observed at the trailing edge, which are apparent in the vorticity field presented in Chapter 6. A more detailed discussion about the flow around the tip for the zero angle of attack case will be given in Section 8.3.3.

7.3.2 $\alpha = 4^0$ Case

The five streamwise locations, at which PIV measurements were made for $\alpha = 4^0$ case, is shown in Figure 7.8. As in the previous subsection, the letter N labels each of the streamwise location.

The average in-plane velocity field at the leading edge for the $\alpha = 4^0$ case is shown in Figure 7.9. Similar to the vector field at this station for the $\alpha = 0^0$ case, the vectors are everywhere directed away from the wing. However, here the in-plane motion is no longer symmetric like in the $\alpha = 0^0$ case. The magnitude of the velocity on the suction side is clearly higher than that on the pressure side. The corresponding vorticity plot shows some resemblance to that for the $\alpha = 0^0$ case, where two vortices of opposite sign are observed on the wing surface near the tip.

At 0.5 cm behind the leading edge, the in-plane vector field is qualitatively similar to that at the leading edge as shown in Figure 7.10. As in the $\alpha = 0^0$ case, the two vortices have grown in size and strength at this station. However, another region of

negative vorticity is observed in the region adjacent to the tip, in addition to the two opposite-signed vortices.

The in-plane motion looks quite different at the streamwise station corresponding to the place where the airfoil section reaches its maximum thickness (Figure 7.11). Here, the velocity magnitude on the pressure side is higher than on the suction side. At this streamwise location the flow moves from the pressure side toward the tip. It seems that the flow coming from the high-pressure region cannot work its way toward the suction side. Instead, air from the pressure side continues to move outward. The flow near the tip surface is evidently moving toward the suction side creating a small circulating region around the right corner of the tip. The corresponding vorticity field shows a region of relatively high axial vorticity surrounding the tip, from the pressure side to suction side.

The flow continues to move from the high to the low-pressure side at the mid-chord as evident from the plot shown in Figure 7.12. Unlike at the earlier measurement station, here the air from the pressure side can negotiate the sharp tip corner and flow around the tip toward the suction side. Now, a strong vortex is observed on the suction side near the tip. In addition, region where the vorticity is of opposite sign is also detected on the suction side next to the stronger vortex.

At the final measurement station near the trailing edge, there is approximately no in-plane motion on the pressure side as apparent from the vector plot shown in Figure 7.13. Air coming from region above the tip, which is driven by the low-pressure region on the suction side, separates at the right-tip-corner and re-attached somewhere inboard of the suction side. As shown in the vorticity field, the size of the vortex has clearly

increased. This relatively large structure is the one that would develop into the wing tip vortex farther downstream.

7.4 Summary

In this chapter, results from planar DPIV measurements of velocity fields on the wing surface near the tip are presented. The measurements are made at two different angles of attack: 0^0 and 4^0. Both average and instantaneous axial vorticity fields at five streamwise locations on the wing are presented.

A brief listing of important observations presented in this chapter are as follows:

1. In the front part of the wing up to the streamwise location where the airfoil thickness is at maximum, the flow, for both α cases, is directed away from the wing surface. Away from the tip, the flow is two-dimensional in the XZ plane just like the flow over a 2-D airfoil. In region near the tip, the flow becomes three-dimensional and vortices of opposite sign are observed, for both α cases.
2. At the streamwise station corresponding to the place where the airfoil section reaches its maximum thickness, the in-plane motion is very small everywhere, for the $\alpha = 0^0$ case. For the $\alpha = 4^0$ case, the pressure difference on the "pressure" and "suction" sides of the wing surface start to drive the flow of air from the high-pressure side to the low-pressure side.
3. For the $\alpha = 0^0$ case, the two opposite-signed vortices disappear near the mid-chord, as the flow near the tip changes its direction (vectors are directed inboard). Another pair of vortices is observed near the trailing edge. However, the sign of the pair is now just the opposite of the sign of the pair observed earlier.

4. For the $\alpha = 4^0$ case, the fluid continues to move around the tip from the high-pressure region to the low-pressure region, downstream from the location where the airfoil is at its maximum thickness. A structure that closely resembles a "wing tip" vortex is first observed on the suction side of the wing near the tip at the mid-chord.

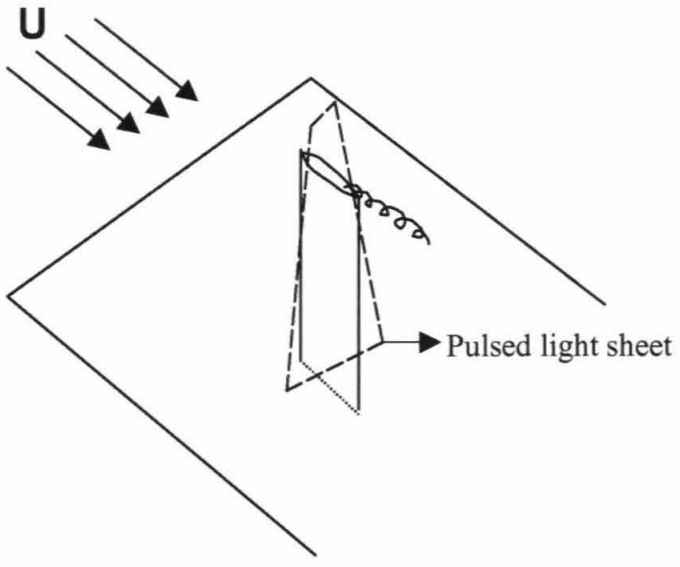

Figure 7.1. Schematic of the experimental setup

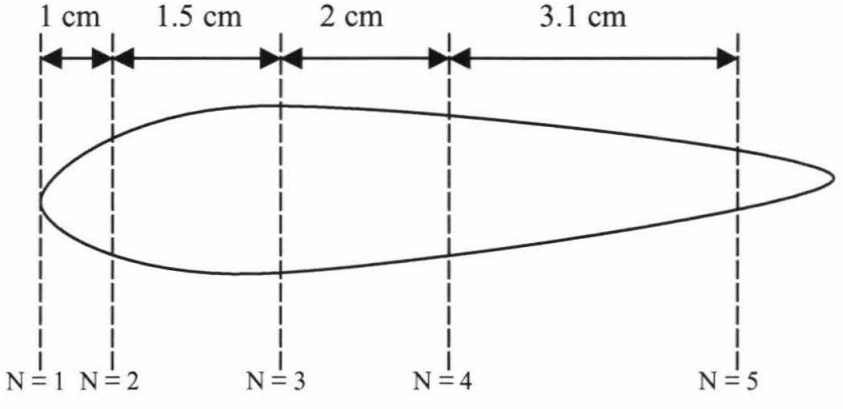

Figure 7.2. Measurement plane locations for $\alpha = 0^0$ case

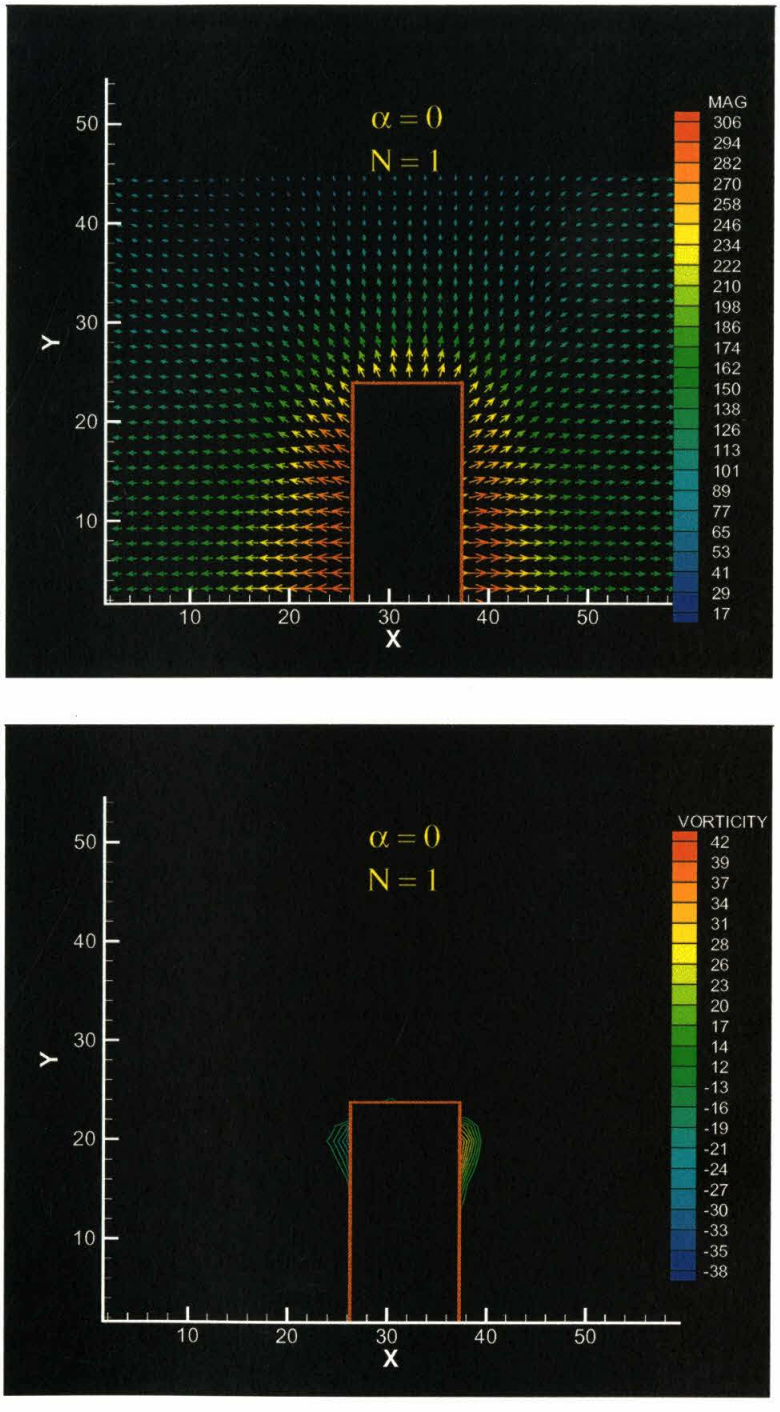

Figure 7.3. Axial vorticity field, N = 1, $\alpha = 0^0$

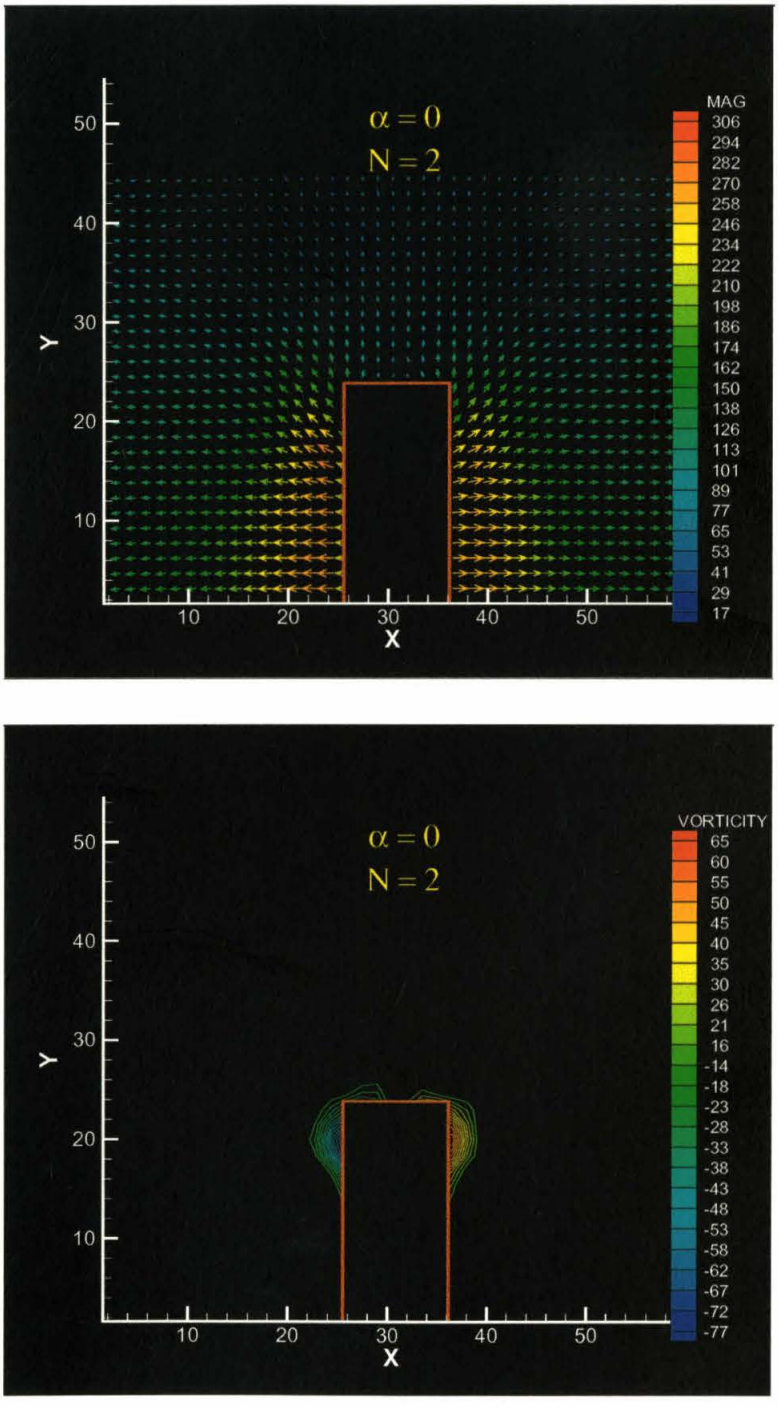

Figure 7.4. Axial vorticity field, N = 2, $\alpha = 0^0$

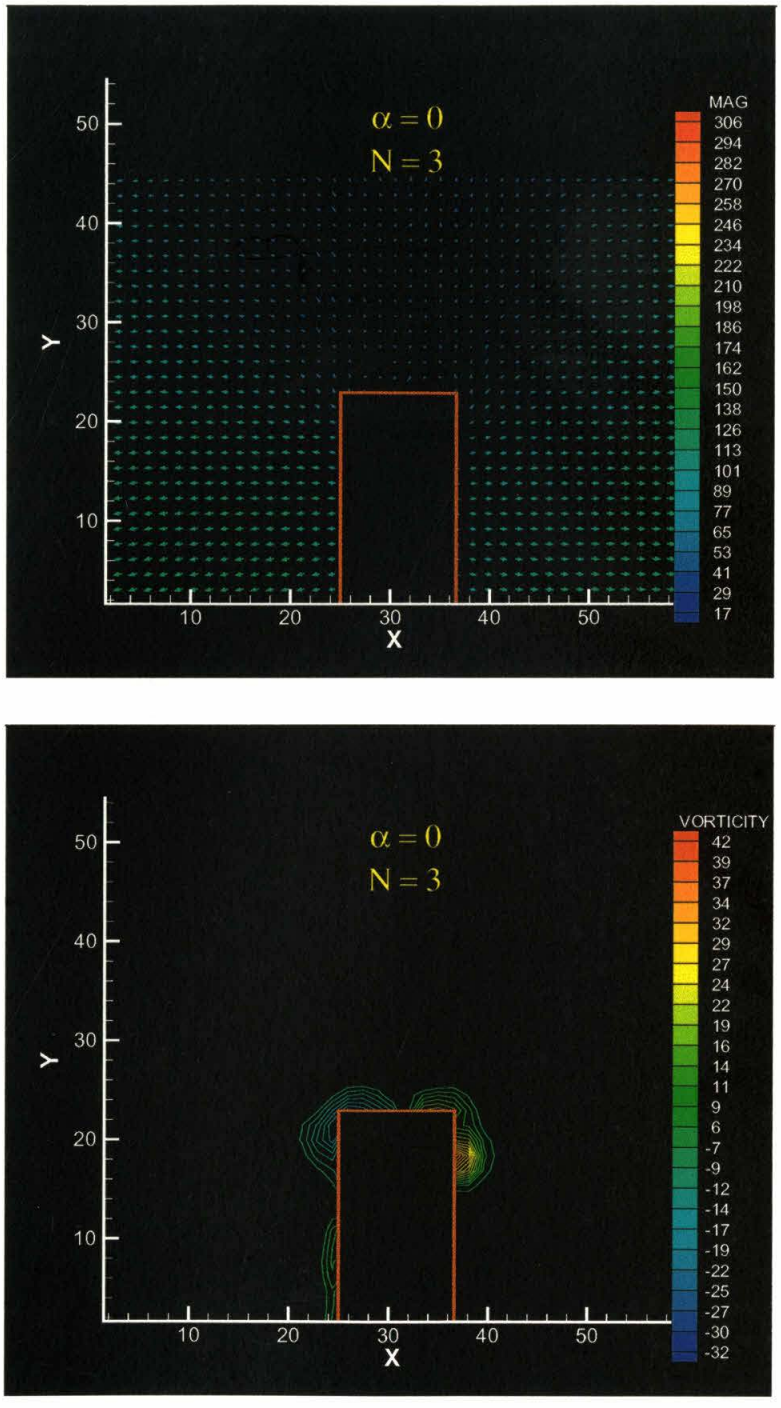

Figure 7.5. Axial vorticity field, N = 3, $\alpha = 0^0$

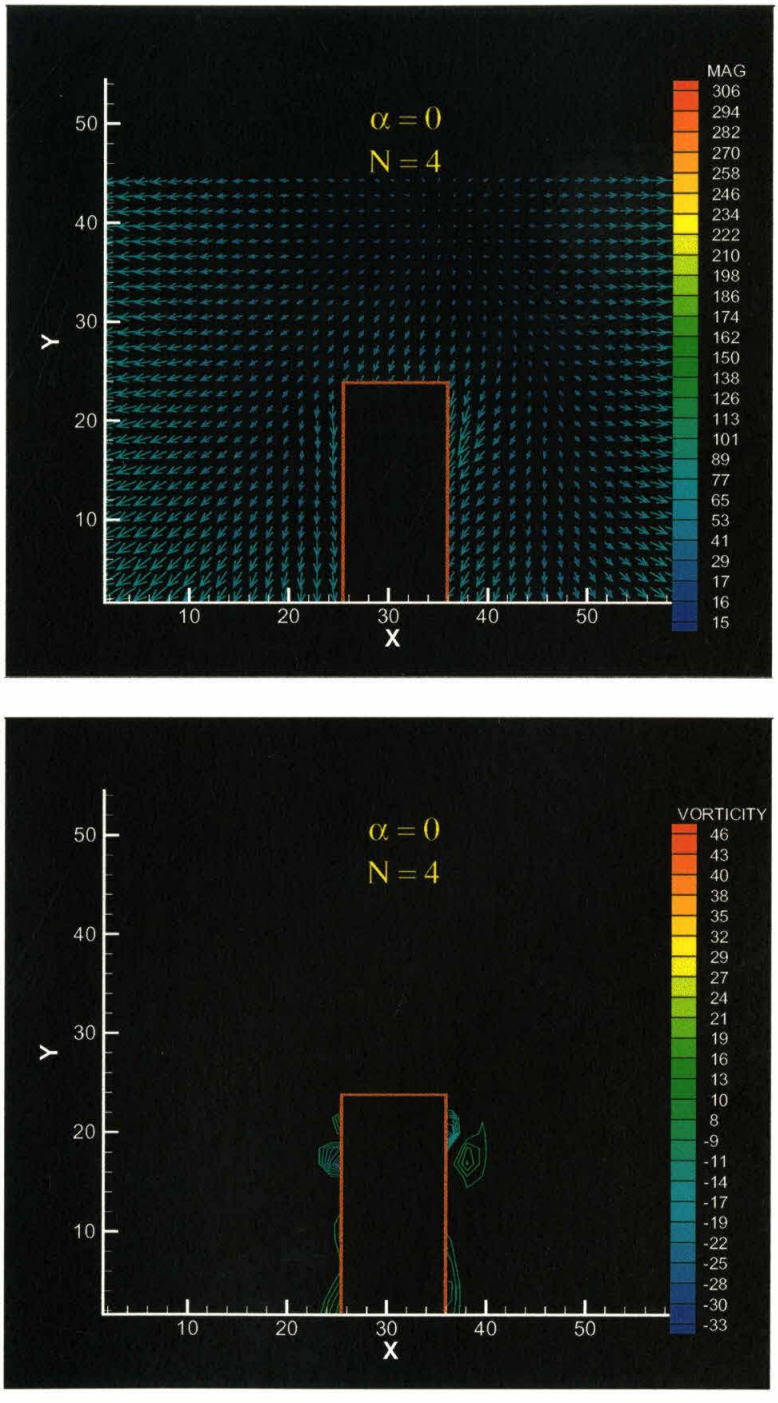

Figure 7.6. Axial vorticity field, N = 4, $\alpha = 0^0$

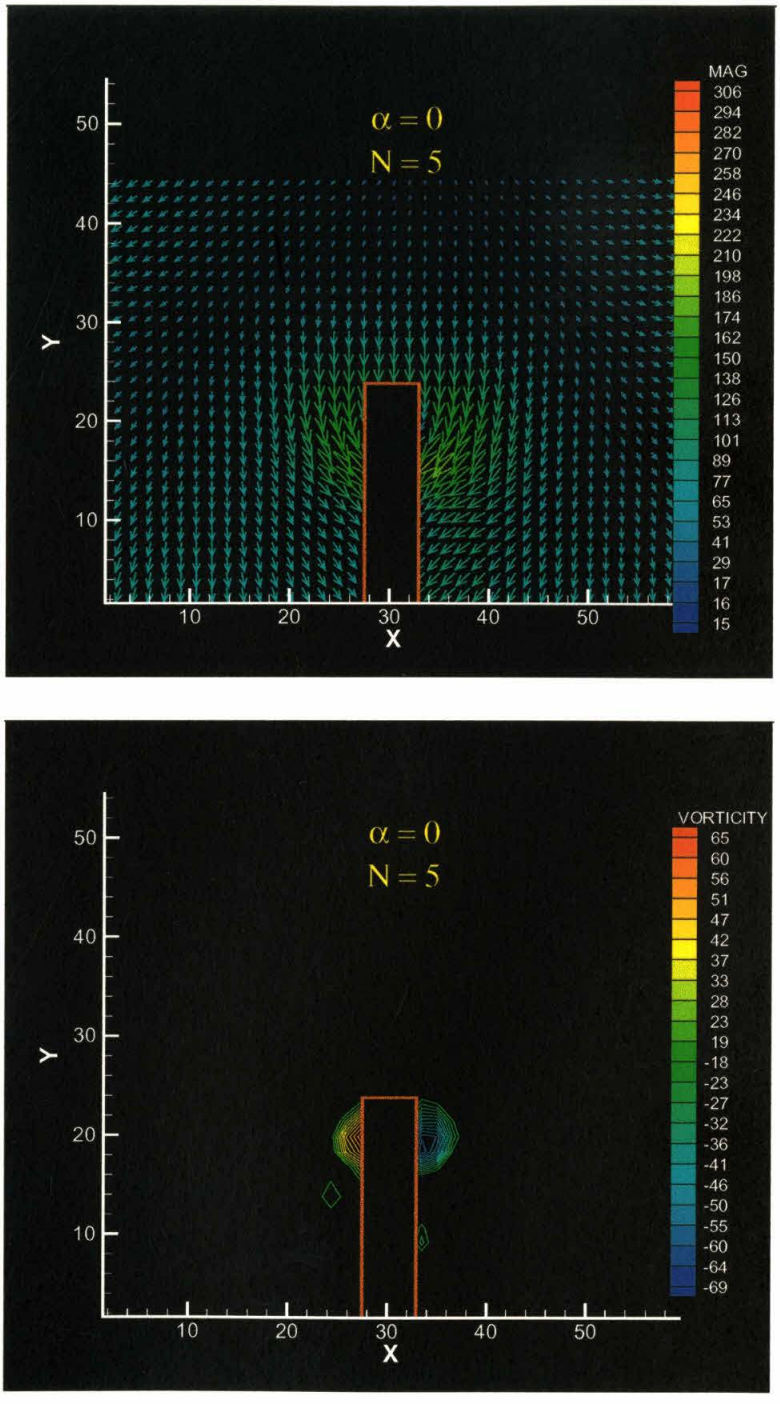

Figure 7.7. Axial vorticity field, N = 5, $\alpha = 0^0$

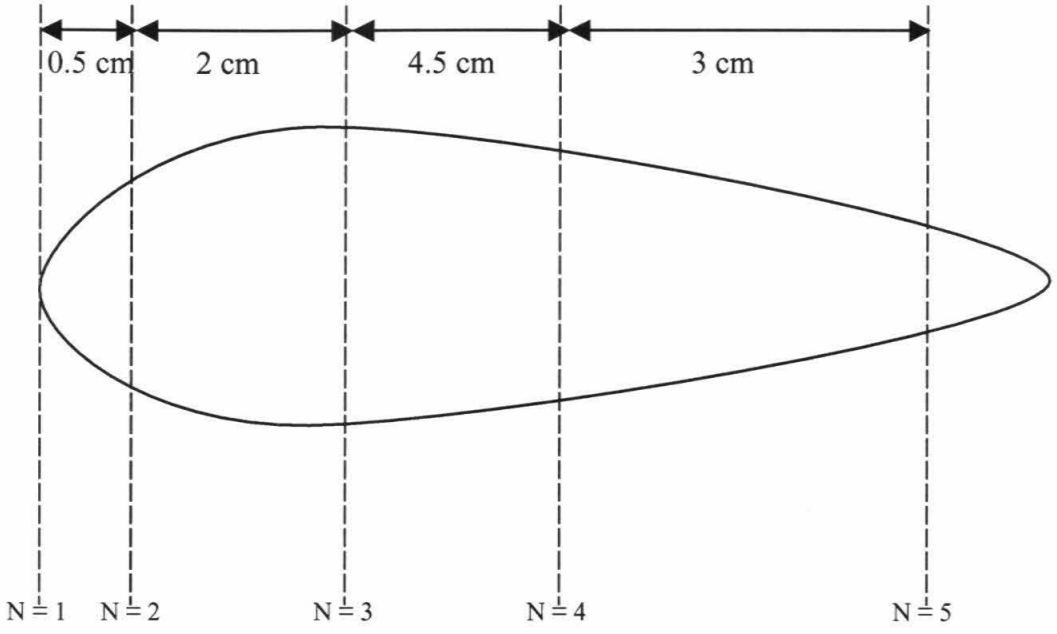

Figure 7.8. Measurement plane locations for $\alpha = 4^0$ case

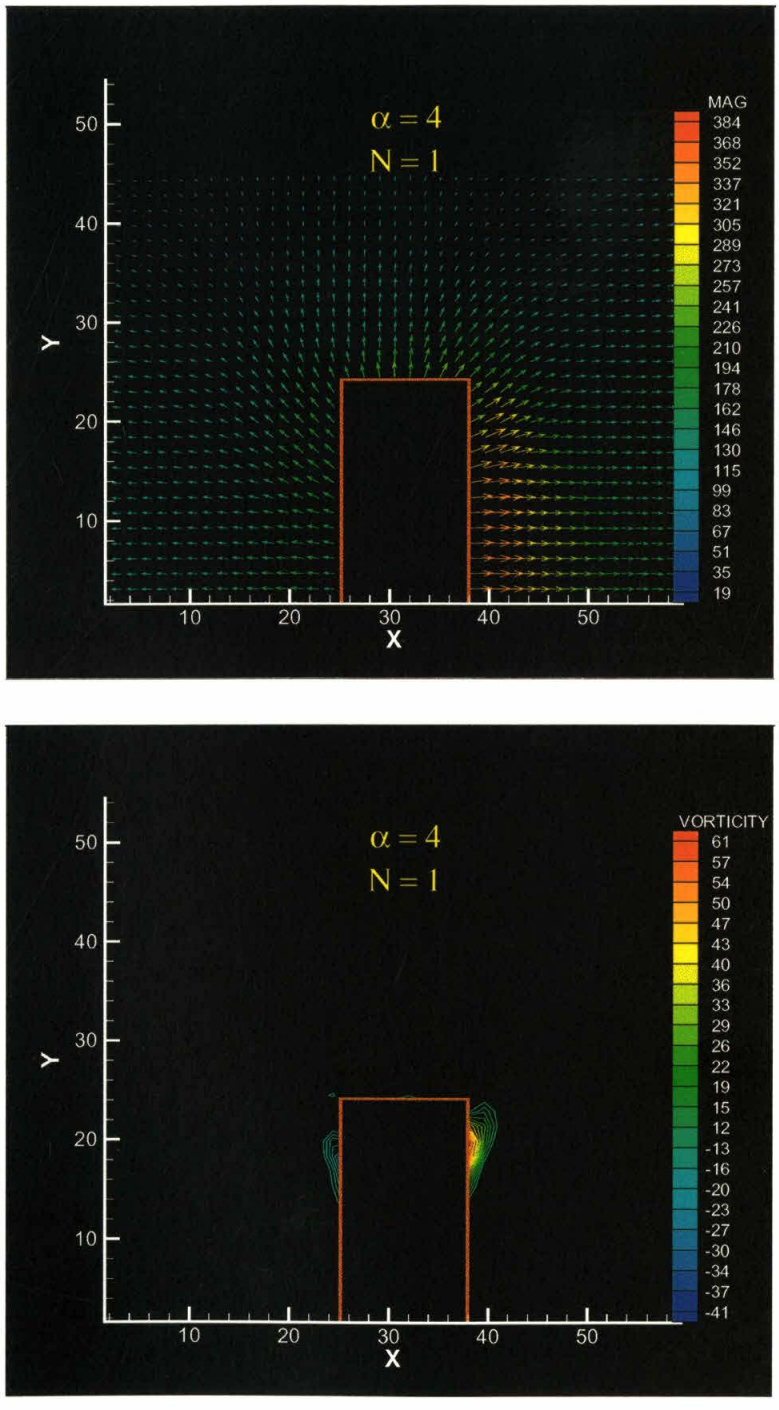

Figure 7.9. Axial vorticity field, N = 1, $\alpha = 4^0$

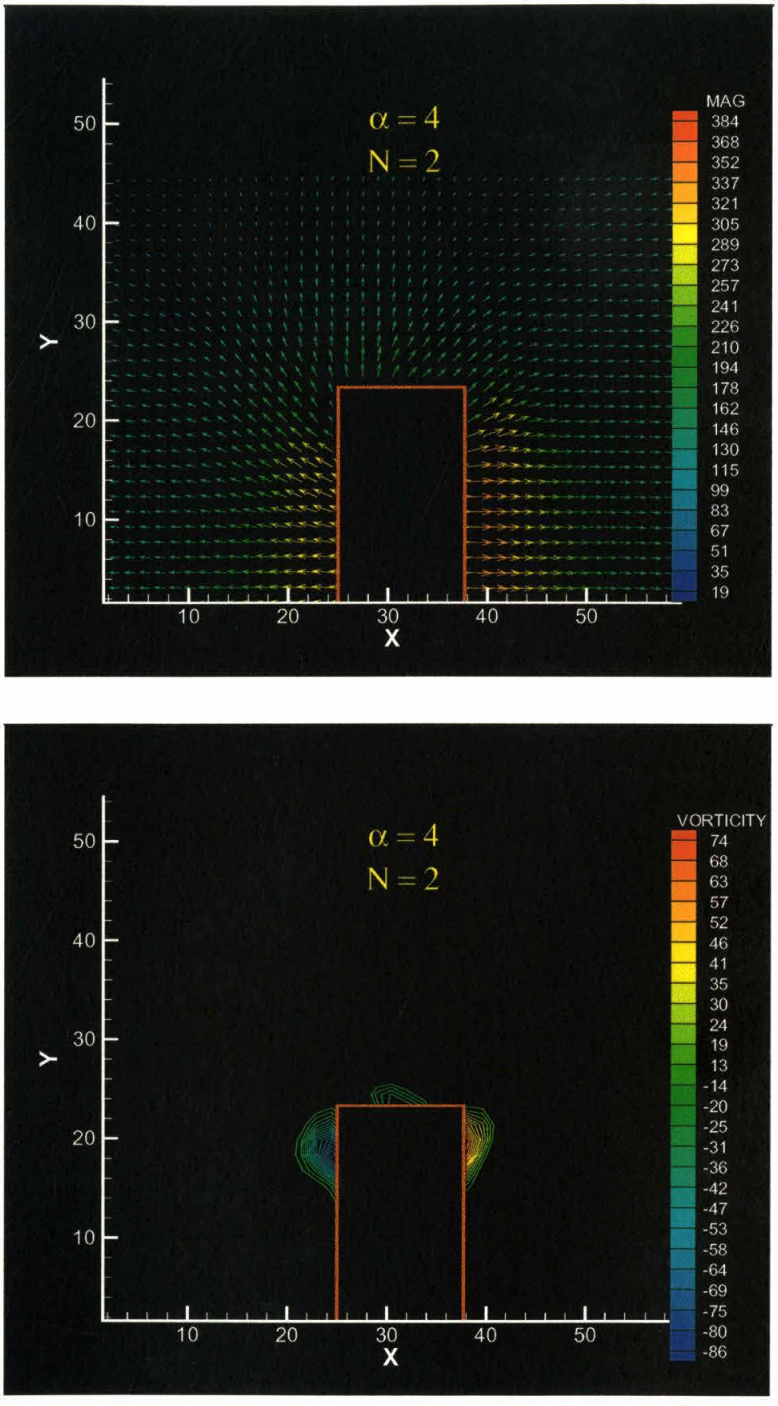

Figure 7.10. Axial vorticity field, N = 2, $\alpha = 4^0$

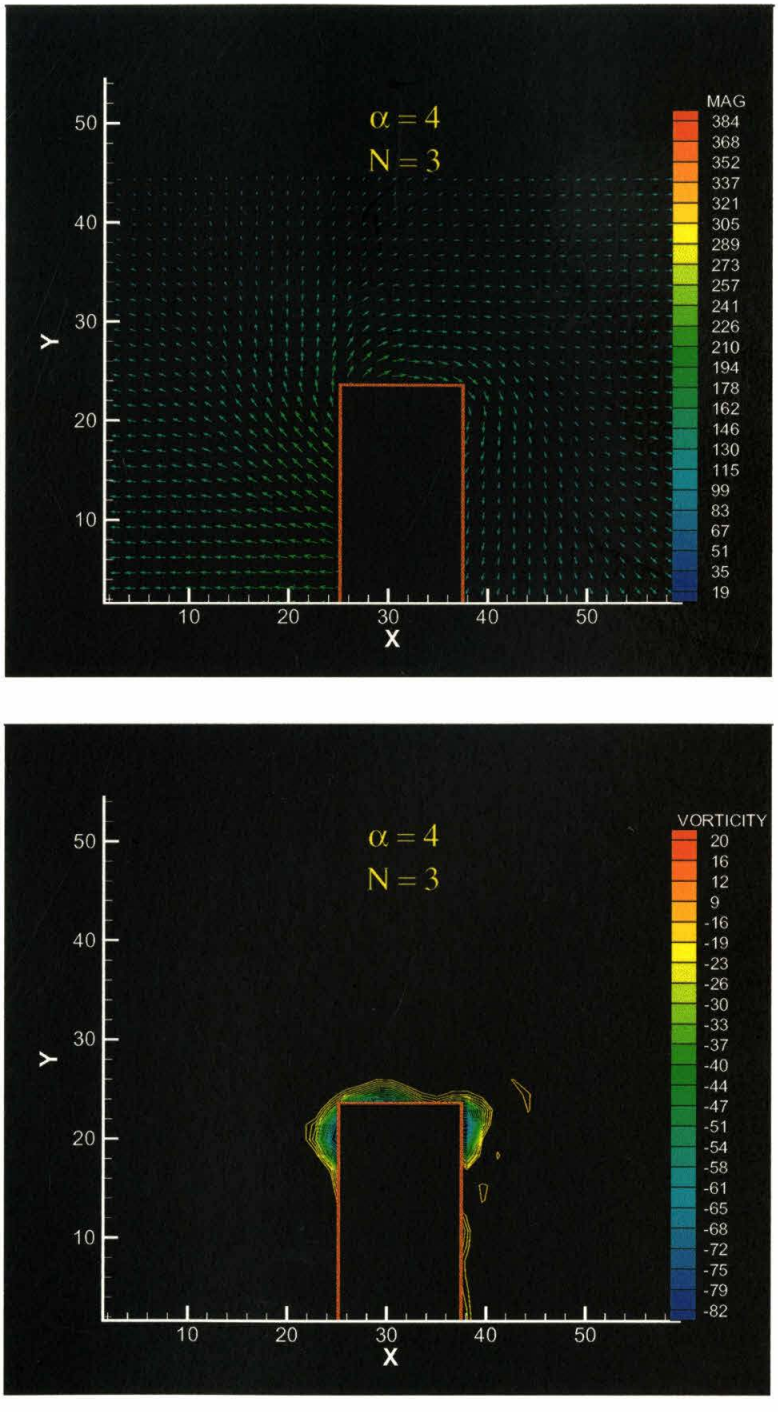

Figure 7.11. Axial vorticity field, N = 3, $\alpha = 4^0$

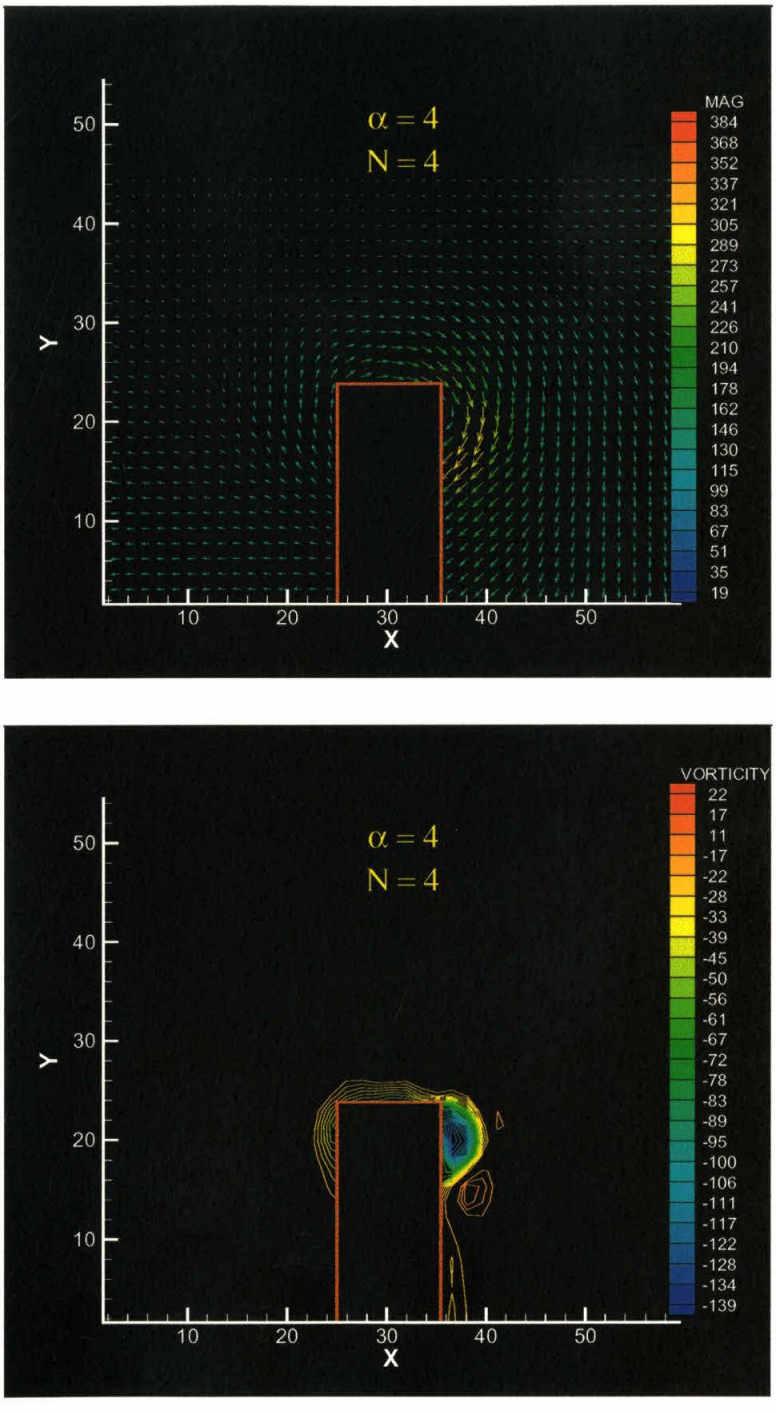

Figure 7.12. Axial vorticity field, N = 4, $\alpha = 4^0$

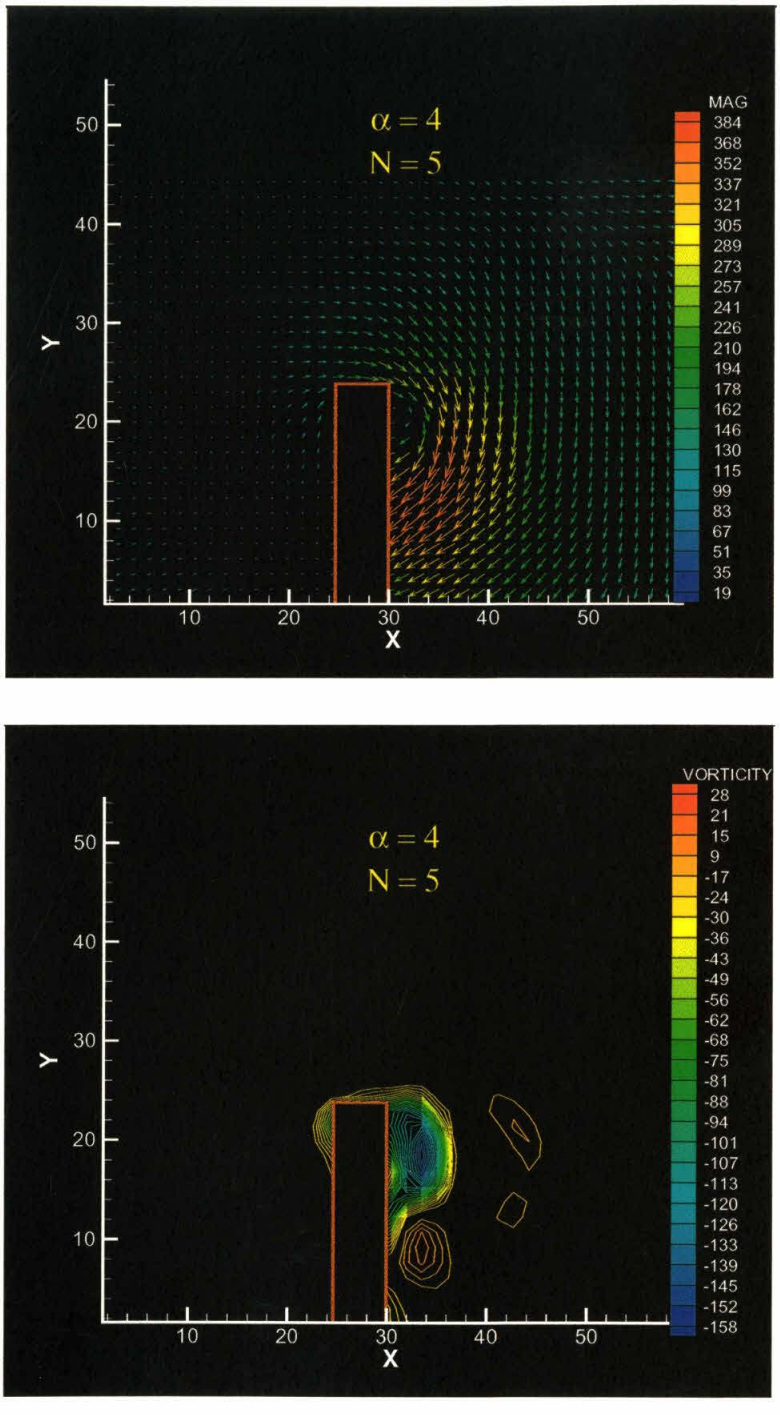

Figure 7.13. Axial vorticity field, N = 5, $\alpha = 4^0$

CHAPTER 8

Effects of Boundary Layer and Tip Geometry

8.1 Introduction

Results presented in Chapter 6 suggest a possibility that the unsteady motion of the wing tip vortex is a result of the interactions of the main vortex with other vortices. In this chapter, we examine this possibility further by changing the axial vorticity distribution on the wing.

In the current study, two sets of measurements are made to accomplish this task. In the first set of measurements, the boundary layer on the suction side is modified by introducing a trip wire. In the second set of measurements, the tip geometry is modified from the basic rectangular geometry to alternatives geometries. With these modifications, it was hoped that the axial vorticity distribution at the trailing edge could be changed with only a slight change in the strength of the main tip vortex. Thereafter, the effect of the satellite vortices on the motion of the main vortex could be studied.

This chapter begins with the detailed description of the two modifications mentioned above. Next, the axial vorticity fields obtained from the measurements are presented. The structure of the vortex core is compared to that of the basic rectangular case. Finally, the instantaneous locations of the vortex center are compared with that of

the original case to study the result of the modifications on the unsteady motion of the wing tip vortex.

8.2 Experimental Conditions

As in the previous experiments, the freestream velocity of the wind tunnel is set at 1.5 m/s for all measurements presented in this chapter. Again, this corresponds to a Reynolds number, based on the chord length, of approximately 9040. The wing model is exactly the same wing used in the previous experiments (NACA 0012 profile). However, in the current experiments, the wing is slightly modified. The modifications made are described in the following subsections. Results presented in this chapter were obtained from measurements of the velocity field by using stereoscopic PIV.

8.2.1 Boundary Layer Modification

For the boundary layer modification, a trip wire is introduced on the suction side of the wing. The wire is placed spanwise between the leading edge and the point where the thickness of airfoil is at a maximum (approximately in the middle of the two points). The position of the trip wire with respect to the wing is sketched in Figure 8.1.a. The wire is very thin and has a diameter of 1mm. All measurements are made with the wing incident set at $\alpha = 4^0$.

8.2 2 Wing Tip Modifications

Three types of wing tip geometries are tested in the experiments presented in this chapter. The three tip geometries are shown in Figure 8.1.b. The modifications are achieved by placing additional surface, made from clay, on the original rectangular tip

surface. In the first two geometries, "ramp up" and "ramp down", the surface of the tip is still flat as before. As depicted in Figure 8.1.b., the tip is rounded in both the streamwise direction and the XY-plane, for the "rounded" tip case. The majority of the measurement results presented in this chapter are for the rounded tip geometry. For the "ramp up" and "ramp down" tip geometry, measurements are only made for the $\alpha = 0^0$ case at Z/C = 0.

8.3 Vorticity Distributions

In this section, contours of axial vorticity are presented. The axial vorticity fields presented are computed from the in-plane components of the average velocity fields.

8.3.1 Boundary Layer Modification

As mentioned before, the boundary layer is modified by placing a trip wire on the suction side of the wing. At the Reynolds number considered in this experiment (Re ~ 9000), the effect of the trip wire is not to transform the laminar boundary layer into a turbulent boundary layer. The purpose of introducing the trip wire is to eliminate the suction side vortex layer (the sign of the vorticity in this layer is opposite that of the wing tip vortex) without significantly changing the strength and the distribution of the other vortices. In particular, we want to examine the contribution of the suction side vortex layer to the unsteady motion of the primary vortex. In this subsection, the axial vorticity fields for the $\alpha = 4^0$ case obtained in this case, at various streamwise stations, are presented and compared with the fields shown in Chapter 6. The vorticity field for the current case (hereafter referred to as case B) is shown in the upper portion of each figure

while the vorticity field for the original rectangular tip case (hereafter referred to as case A) is depicted in the lower portion.

The vorticity fields at Z/C = 0 (trailing edge) are shown in Figure 8.2. As can be seen in the upper plot, the suction-side vortex layer is no longer observed. Consequently, the trip wire has successfully broken up the vorticity in the layer into smaller scale (a similar situation is observed in Chapter 6 for the higher α case). However, the presence of the wire changes not only the vorticity distribution on the suction side but also changes the distribution on the other regions. Now, there are two smaller vortices in the vicinity of the large vortex. Also, unlike in case A, the large vortex in case B is composed of only a single vortex. The peak vorticity of the large vortex in case B is clearly higher than that in case A. Also note that the vortex layer in case B is wider and stronger than the corresponding layer in case A. The changes in the strength of the vortices, other than the smaller vortex, are unavoidable. Due to the placement of the trip wire along the span, the pressure distributions on the suction side are modified. The change in the pressure distribution leads to the alteration of the total circulation of the wing and, hence, the change in the strength of the vortices.

The difference between the two cases is even more visible in Figure 8.3, where the vorticity contours for the two cases at Z/C = 1 are plotted. In case A, the rollup process is almost completed at this station. However, in case B the vorticity layer is still rolling up into the tip vortex at Z/C = 1. Also, the vortex core in case B is clearly stronger than in case A.

The comparisons between the vorticity fields of the two cases at streamwise stations farther downstream are shown in Figure 8.4, Figure 8.5, and Figure 8.6. From

these figures, it is clear that, in case B, the rollup continues up to the streamwise station of 4-chord length behind the wing.

8.3.2 Wing Tip Modification (Rounded Tip Geometry)

In this subsection, the effect of wing tip geometry is examined. In the last subsection, the purpose of the modification was to study the effect of the vortex layers. The modification in this subsection is intended to study the effect of the "smaller" vortices to the dynamics of the main vortex. In the experiment presented here, the wing tip is rounded, as described in Section 8.2.

As in the preceding subsection, the axial vorticity fields for the $\alpha = 4^0$ case, at various streamwise stations, are presented and compared with the fields presented in Chapter 6. The figures, in this subsection, are organized as in Section 8.3.1. The vorticity field for the current case (hereafter referred to as case C) is shown in the upper portion of each figure while the vorticity field for the original rectangular tip case is depicted in the lower portion.

The vorticity field at the trailing edge for the rounded tip case is shown at the top of Figure 8.7. As in case B, two smaller vortices are observed near the main vortex. However, here the two vortices are larger and stronger than in case B. The shape of the main vortex is also changed. It seems that the main vortex is stretched by the two smaller vortices. The two opposite-signed vortex layers are visible. They look qualitatively the same as in case A. Therefore, changing the shape of the tip does not affect the layers significantly, as intended.

The downstream evolutions of these vortices are shown in Figure 8.8 to Figure 8.11. Comparing the top (case C) and the bottom (case A) part of Figure 8.8 to Figure 8.11, it is clear that there are no significant differences observed in plots for the two cases, except for the appearances of very weak opposite-signed vortices in the plots for case C. This is not surprising because, as discussed in Chapter 6, the "smaller" vortices are orbiting around the main vortex. Therefore, they should "disappear" in the averaging process.

Although there are no qualitative differences observed between case A and case C, it is expected that the existence of the extra "smaller" vortex, in case C, would have some effect on the motion of the wing tip vortex. The effect is examined in Section 8.4.

8.3.3 Comparison Between Different Types of Wing Tip Geometry

In Section 8.3.2, we see that the vorticity field is qualitatively altered when the tip geometry is changed. In this subsection, we examine further the effect of tip geometry by considering the zero-angle-of-attack vorticity fields at the trailing edge for four different types of tip geometries. The first two are the rectangular and the rounded tip cases, which have been discussed previously. The others are the "ramp up" and "ramp down" cases, which are mentioned in Section 8.2. Hereafter, the "ramp down" and "ramp up" are referred to as case D and case E, respectively.

The vorticity fields ($\alpha = 0^0$, Z/C = 0) for the 4 different cases are depicted in Figure 8.12. As shown in the figure, two pairs of opposite sign vortices visible in the vorticity field for the case C. The signs of the lower pair are similar to the original rectangular tip case (case A). The signs of the upper pair are just the opposite. The

shapes of the vortices are more elliptical in this case compared to the vortices in case A. The strength of the upper pair is slightly higher than that of the lower pair.

The vorticity field for case D is very similar to that for case C; two pairs of vortices are observed. Here, the upper pair is stronger than in case C while the lower pair is weaker. Two pairs of vortices are also observed in the vorticity field corresponding to case E. However, the upper pair is not as symmetric as the lower pair. Also, now the lower pair is stronger than the upper pair.

As shown in Figure 8.12, the alteration of the tip geometry leads to the change in the axial vorticity distribution at the trailing edge. In particular, the appearance of an additional counter-rotating pair of vortices is observed in cases C, D, and E. One possible explanation for this observation is depicted in Figure 8.13, where the flow in the region near the wing tip, for $\alpha = 0^0$ case, is sketched for two of the four cases considered in this subsection (rectangular and rounded tip case). The first sketch, shown in the upper part of the figure, corresponds to the rectangular tip case. As discussed in Chapter 7, the flow in regions near the tip is driven by the pressure difference between the tip surface (flat surface) and the two sides of the wing where the surface has the shape of NACA 0012 airfoil. At the leading edge, the pressure on the wing surface (stagnation pressure) is higher than in the region near the tip surface. In the region around leading edge near the tip, the flow separates and reattaches creating a small separation bubble, which leads to the appearance of two counter-rotating vortices (see Figure 8.13). Somewhere downstream of this region, the pressure on the wing surface becomes lower than on tip surface. In this region, the fluid moves from the tip surface toward both sides of the wing. The flow separates at the sharp tip corners and rolls up into another counter-

rotating vortices. Explanation in terms of the vortex lines is also given in the figure. In the region near the leading edge, the vortex lines coming from the leading edge separation bubble merge with some of the vortex lines (with opposite sense of rotation) coming from the wing surface boundary layers. These opposite sign vortex lines annihilate each other somewhere near the mid-chord. (Note that the argument regarding the annihilation of the vortex lines is consistent with the result presented in Section 7.3.1. In that section, it was shown that the counter rotating vortices, which were originally observed at the leading edge, disappeared in the region around the mid-chord.) The rest of the vortex lines originating from the boundary layers are redirected in the spanwise direction resulting in the appearance of the two counter rotating vortices at the trailing edge.

The flow in regions near the wing tip is somewhat different when the tip is rounded. A speculation about the flow near the tip for this case is shown in the lower part of Figure 8.13. Here, the flow near the tip is effectively the flow around a slender body. In the front part of the wing, the flow is attached to the slender body unlike the rectangular tip case where the flow separates and reattaches. Somewhere downstream, the flow starts to separate from the body. It is speculated that two open separations occur, one on each side of the symmetry line (see Figure 8.13), forming two vortex sheets. Subsequently, the two vortex sheets roll up into two pairs of counter-rotating vortices observed in Figure 8.12. In terms of vortex lines, the lower pair is due to the redirection of the vortex lines, originating from the wing surface boundary layers, in the streamwise direction. In contrast, the upper pair is the result of the redirection of the vortex lines originating from the tip surface boundary layer (see Figure 8.13).

8.4 Structure of the Vortex Core

Results presented in Section 8.3 indicate that modification of the boundary layer and tip geometry alters the structure of the trailing vortex. In this section, the consequence of such modifications in altering the wing tip vortex structure is examined. In particular, the axial velocity profiles and circulation profiles ($\alpha = 4^0$ case) are presented. These profiles are obtained from average velocity fields.

The axial velocity profiles along a cut through the vortex center, parallel to the X-axis, are shown in Figure 8.14. Each plot in the figure corresponds to axial velocity profiles at a particular Z/C. Each symbol in the plot denotes each of the three different cases considered in Section 8.3.1 and Section 8.3.2 (case A, case B, and case C). The vertical axis, in each plot, shows the axial velocity values normalized by the freestream velocity. The plots show that the axial velocity within the vortex core is less than the freestream velocity for all cases. The peak axial velocity deficit is the highest for the case in which a trip wire is placed on the suction side (case B) and the lowest for the rectangular tip case (case A). The values of the peak axial velocity deficit, for case C (rounded tip case), are always between that for case A and case B. This is true in all plots shown in Figure 8.14. These results suggest that the axial velocity, within the vortex core, strongly depends on the boundary layer and tip geometry.

The plots for the values of circulation as a function of radial distance from the vortex center are shown in Figure 8.15 (the plots are arranged as before). Again, the circulation profiles in each plot exhibit similar trend. The value of the peak circulation is always the highest for case B and the lowest for case C. The peak circulation for case A

is always in between the other two cases (note that the order is different from that of the peak axial velocity). However, the differences between the values of the peak circulation for cases A and C are very small. The reason for much higher values of the peak circulation for case B is already mentioned in the preceding section. In case B, the trip wire is placed along the span of the wing. Hence, the pressure distributions on the suction side are significantly modified. Therefore, the total circulation of the wing increases and so does the circulation of the trailing vortex.

As can be seen from the vorticity plots at the trailing edge, presented in the previous section, the strength of the "small" vortex increases when the tip geometry is changed from the basic rectangular to the rounded one. The estimated values of circulation of the "left-small" vortex (Γ_s) at the trailing edge, for the three different cases, are presented in Table 8.1. As a reminder, the "left-small" vortex appears in all three cases considered, including the original rectangular tip case. Also, the values of the "left-small" vortex circulation at the trailing edge are compared with the estimated values of the maximum circulation at stations farther downstream (Γ_{max}). As presented in the table, the circulation of the smaller vortex is much higher for the rounded tip case than for the basic rectangular tip case. The circulation of the smaller vortex is approximately 2.6 % of Γ_{max} for cases A and B. For the rounded tip case, the circulation of the smaller vortex is at roughly 13.6 % of Γ_{max}.

CASE	Γ_s (mm^2/s)	Γ_{max} (mm^2/s)	Γ_s / Γ_{max}
A (Rectangular tip)	373	14552	0.026
B (Trip Wire)	544	21110	0.026
C (Rounded Tip)	1834	13460	0.136

Table 8.1. Circulation of the small opposite-signed vortex

The results presented in this section reveal that the structure of the wing tip vortex strongly depends on the condition of the boundary layer and the tip geometry. As a reminder, all measurements were conducted at the same freestream velocity. Also, the same wing model, with the modifications mentioned above, is used in all measurements.

8.5 Instantaneous Core Location

As shown in previous sections, boundary layer and tip geometry modifications altered the structure of the main vortex and changed the axial vorticity distribution in general. Therefore, it is expected that the modifications would also change the interactions between the vortices. Therefore, the instantaneous motion of the wing tip vortex would also be affected.

The effect of the vortex interactions on the motion of the main trailing vortex can be detected by observing the path followed by the wing tip vortex at each instant. As in Chapter 6, the instantaneous position of the wing tip vortex is found by identifying the location of its center, with the method described in Chapter 6.

The instantaneous locations of the vortex center for the three different cases, considered in the previous subsections, are shown in Figure 8.16. For each plot in the figure, the crossflow plane is located at a particular streamwise station. As in Chapter 6, each data point is normalized by the average location of the vortex center for the corresponding case (point (1,1) corresponds the average position of the vortex center). As visible from the figure, the fluctuation at all Z/C considered is the lowest for the rounded tip case (case C). The level of unsteadiness of the vortex center, for case B (trip wire case), is lower than that for the rectangular tip case up to Z/C = 2. However, farther downstream the fluctuation for case C increases. At Z/C = 4, the fluctuation is as high as, or, perhaps, even higher than that for the rectangular tip case.

The results from the current experiments confirm the conclusion made in Chapter 6. The results presented above show that the unsteadiness of the wing tip vortex does not depend solely on the strength of the primary wing tip vortex. Results from previous section show that the circulation of the wing tip vortex is the highest for case B and is the lowest for case C. Also, the strength of the wing tip vortex in case C is almost the same as in case A. However, in Figure 8.16, it is clear that case C has the lowest fluctuations among the three cases considered. In fact, at Z/C = 4 the level of fluctuation for case B is higher than the other two cases.

As presented in Section 8.3, the three different cases considered also have different axial vorticity distributions at the trailing edge (Z/C = 0). The suction side vortex layer vanishes when the trip wire is introduced. The strength of the smaller opposite-signed vortex increases when the tip is rounded. Additionally, both modifications introduce another vortex adjacent to the primary vortex, with an opposite

sense of rotation. The results presented in Figure 8.16 show that the levels of unsteadiness are altered with such modifications. In case C, the strength of the smaller vortices is approximately 13.6 % of the strength of the primary vortex and the radial fluctuations, for this case, are the lowest among all the cases considered. In case B, the ratio of the strength of the smaller vortex to the strength of the primary vortex is approximately the same as in case A. The fluctuations for these two cases are roughly the same, although initially the fluctuations for case B are slightly lower than for case A, perhaps because of the difference in the initial vorticity distribution.

Because of the appearance of the extra smaller vortex, it is not clear whether the vortex layer or the smaller vortex has a more significant effect on the motion of the main tip vortex. However, the results presented in this section strongly suggest that the unsteady motion of the tip vortex is a result of interactions between the tip vortex and the satellite vortices. It is important to mention that some of the measurements are repeated at least twice. In general, the results are always in agreement with those presented above.

8.6 Summary

In this chapter, the effect of the boundary layer and wing tip geometry are examined. The boundary layer is modified by placing a thin trip wire on the suction side of the wing surface. There are three tip geometries considered in this study. Among these three alternative tip geometries, the rounded tip is studied most extensively. The measurement results from the boundary layer and the tip geometry (rounded tip) modification are compared with the basic rectangular tip case.

A brief listing of important results presented in this chapter are as follows:

1. The axial vorticity fields are altered by the modifications. The trip wire breaks up the vorticity layer on the suction-side into smaller vortices and introduces an additional "small" opposite-signed vortex. Also, the introduction of the trip wire delays the rollup process farther downstream. The rounded tip geometry also introduces an additional "small" vortex. Both modifications change the strength and the shape of the main vortex.
2. The core structure of the tip vortex, downstream of the wing, is also affected by the modifications. The peak axial velocity deficit is the highest for the case in which a trip wire is placed on the suction side and the lowest for the rectangular tip case. The value of the peak circulation is always the highest for the case with the trip wire and the lowest for the rounded tip case.
3. The effect of the modifications is also observed in the instantaneous location of the vortex center. The observations of the instantaneous location of the vortex core suggest that the unsteady motion of the wing tip vortex does not depend on the strength of the tip vortex alone (stronger tip vortex is not always more steady than the weaker vortex), but depends on the ratio of the strength of the smaller vortex to the wing tip vortex. The results support the statement made at the end of Chapter 6 that the unsteady motion of the wing tip vortex is a result of the wing tip vortex interactions with the satellite vortices.

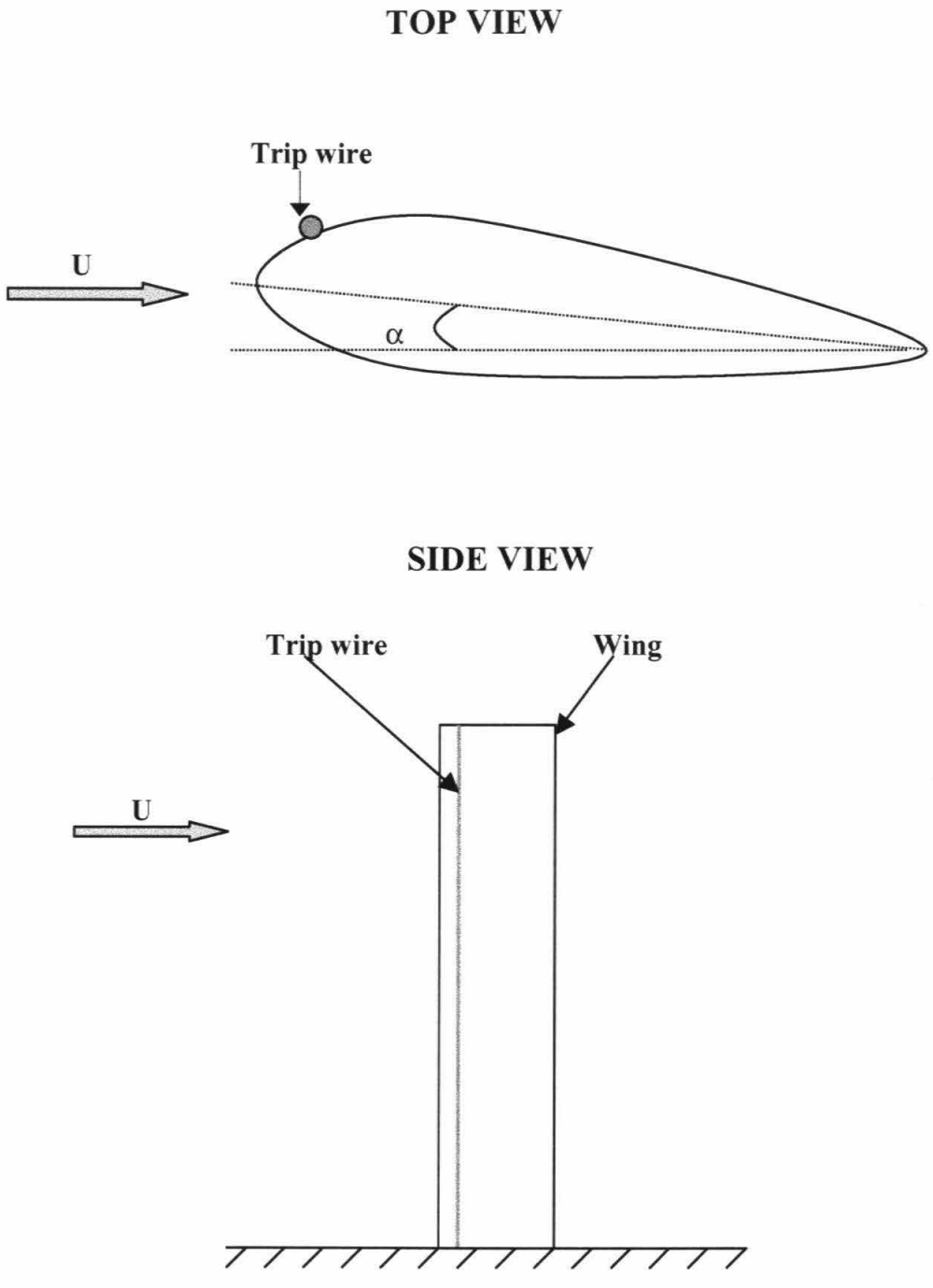

Figure 8.1.a. Location of the trip wire

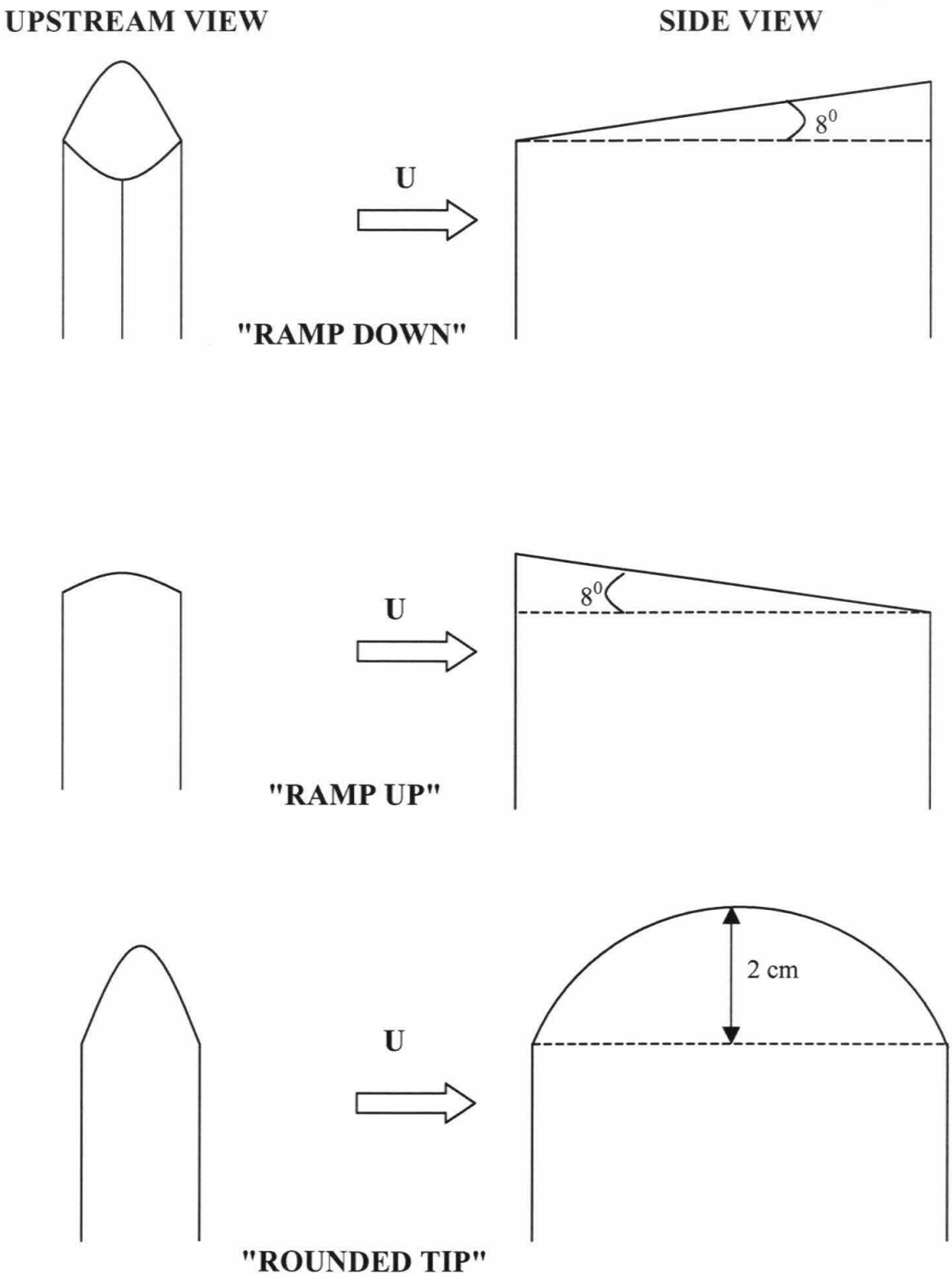

Figure 8.1.b. Modified wing tip geometries

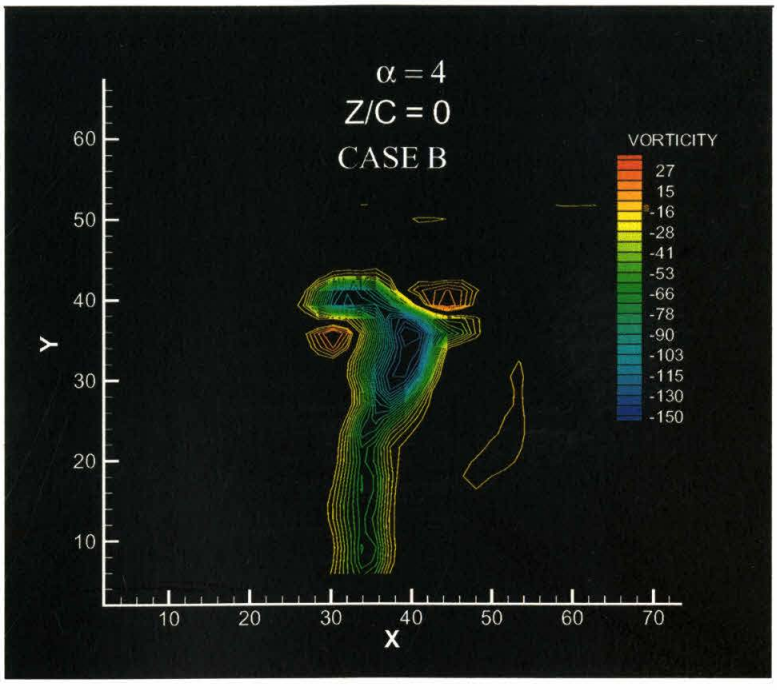

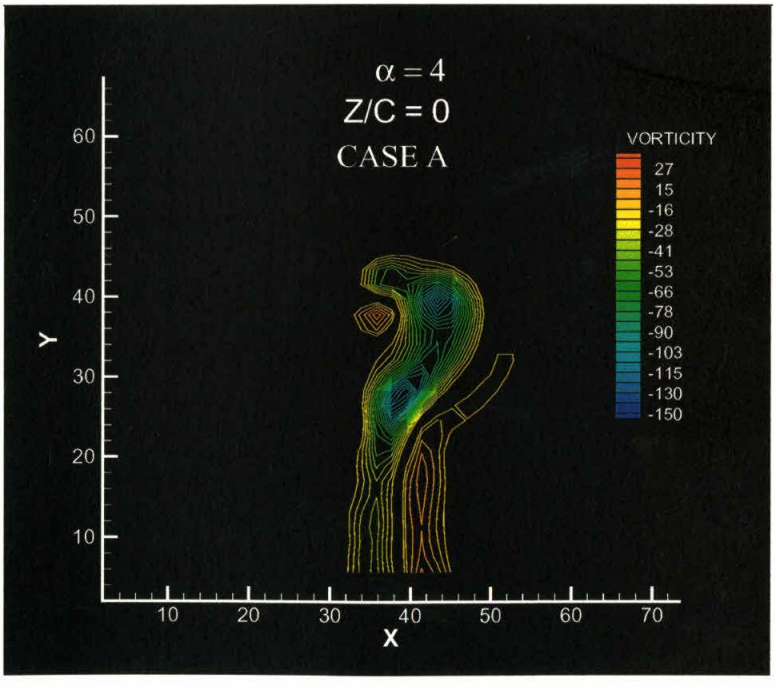

Figure 8.2. Boundary layer modification, axial vorticity field, $\alpha = 4^0$, Z/C = 0

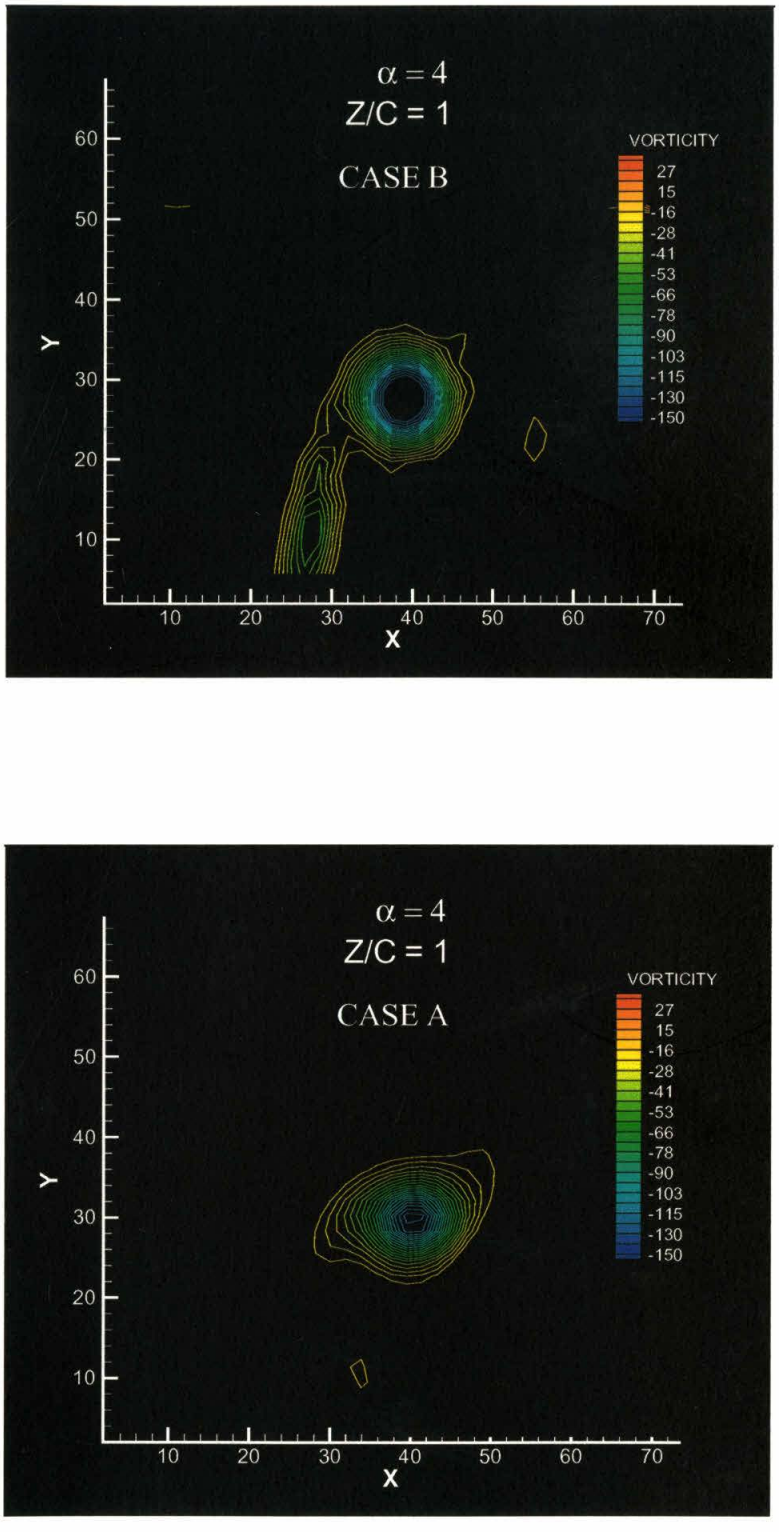

Figure 8.3. Boundary layer modification, axial vorticity field, $\alpha = 4^0$, Z/C = 1

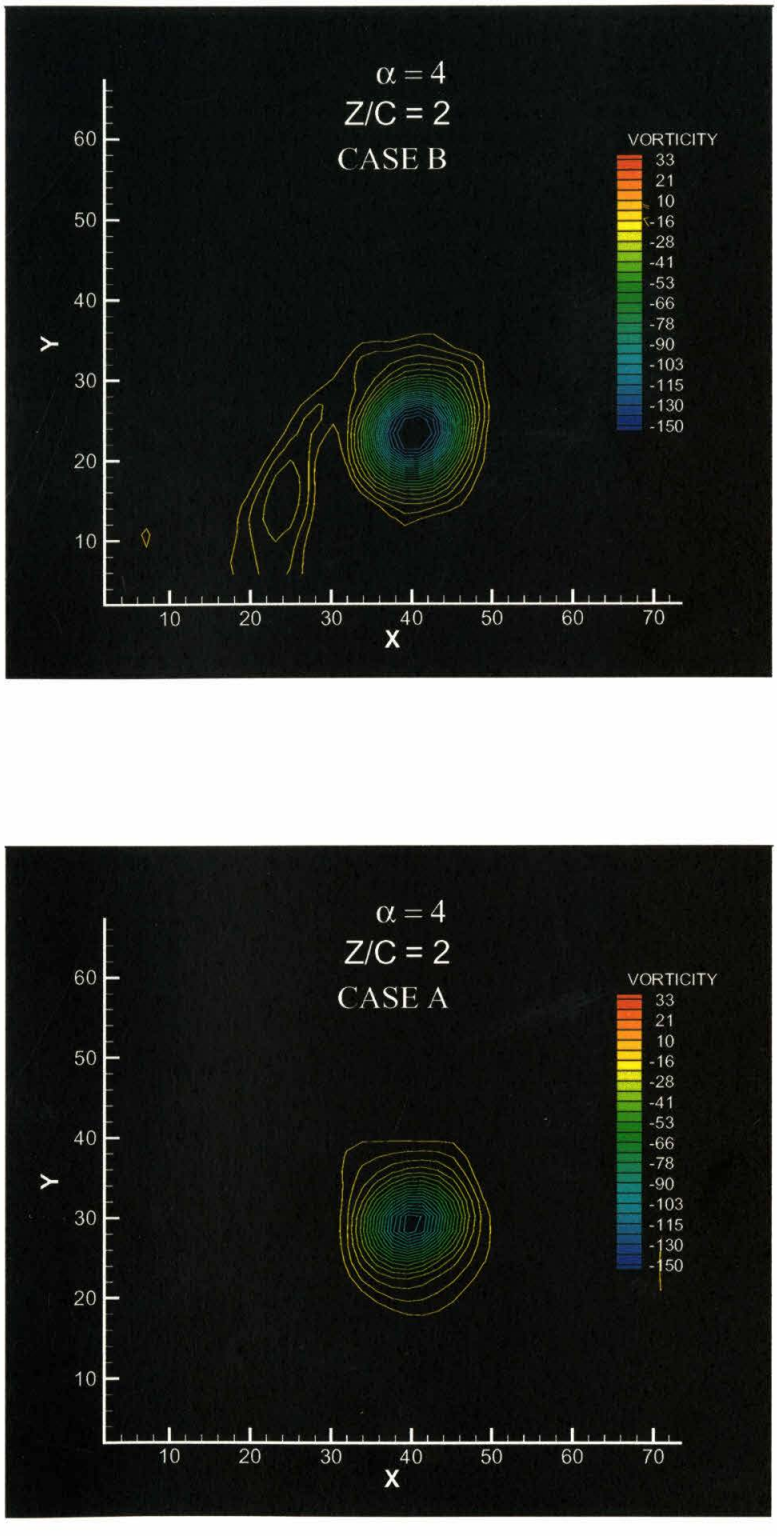

Figure 8.4. Boundary layer modification, axial vorticity field, $\alpha = 4^0$, Z/C = 2

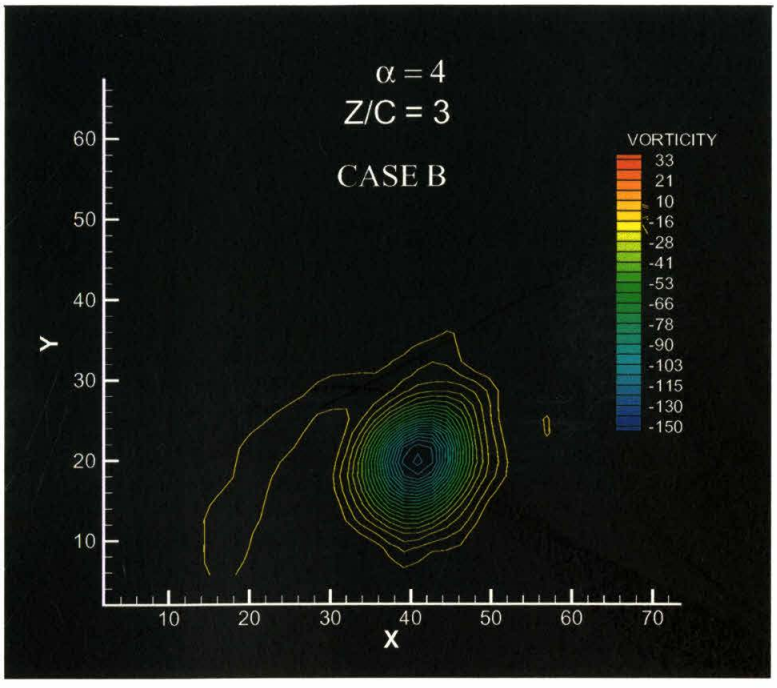

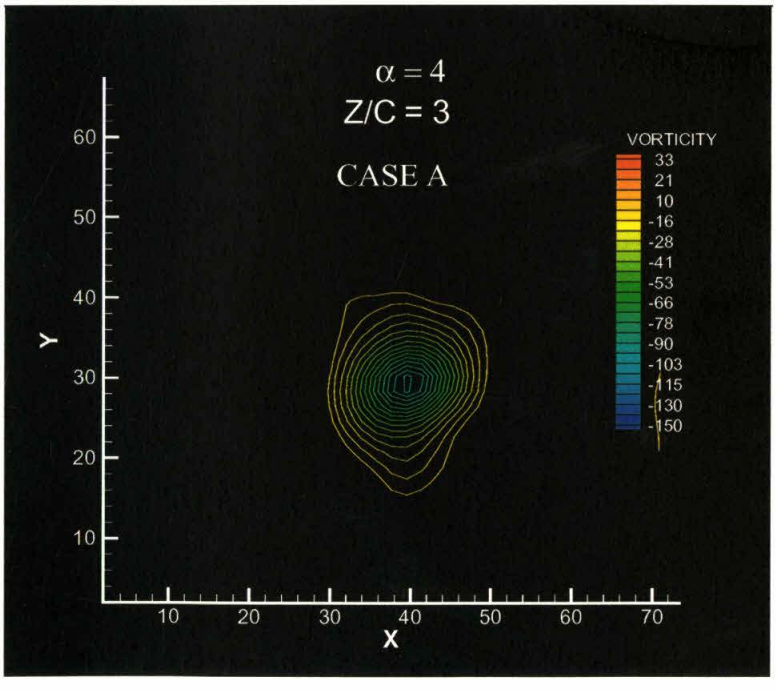

Figure 8.5. Boundary layer modification, axial vorticity field, $\alpha = 4^0$, Z/C = 3

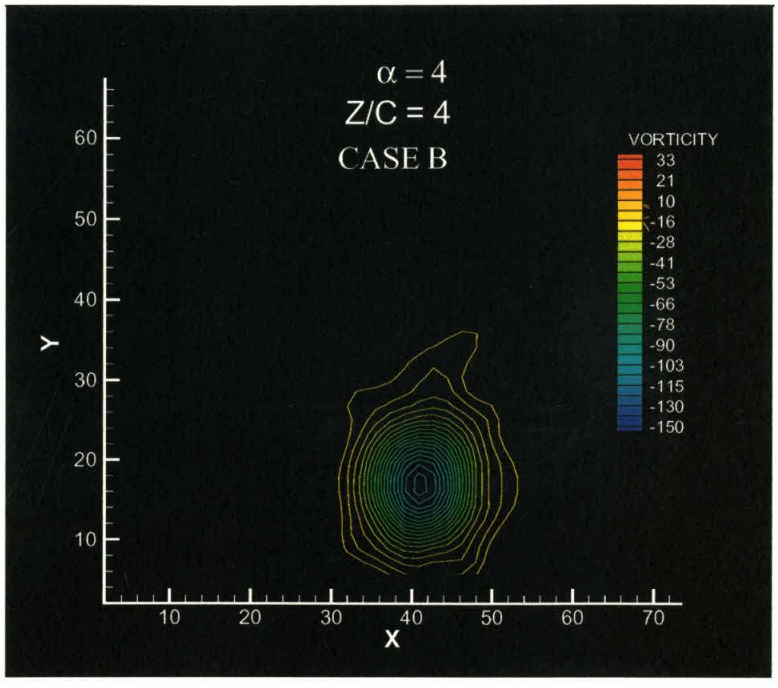

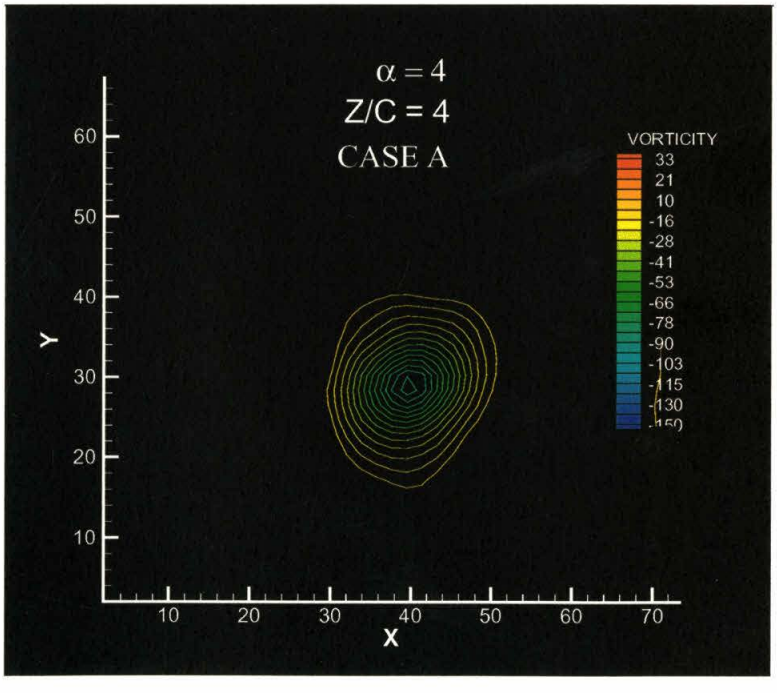

Figure 8.6. Boundary layer modification, axial vorticity field, $\alpha = 4^0$, Z/C = 4

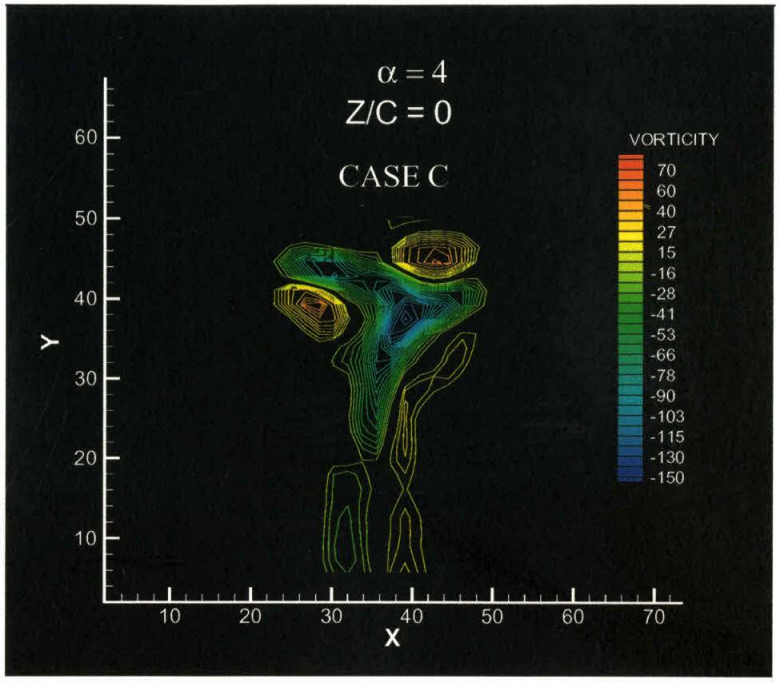

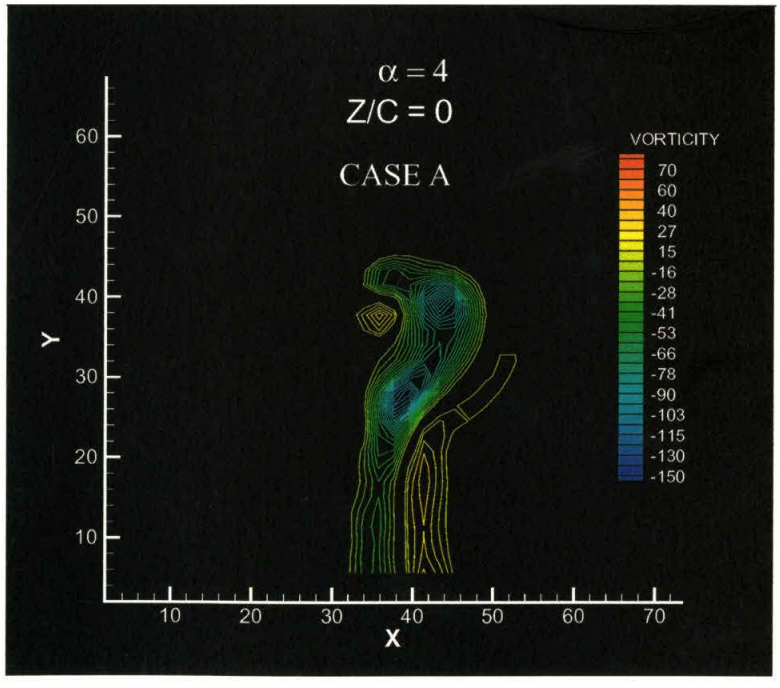

Figure 8.7. Tip geometry modification, axial vorticity field, $\alpha = 4^0$, Z/C = 0

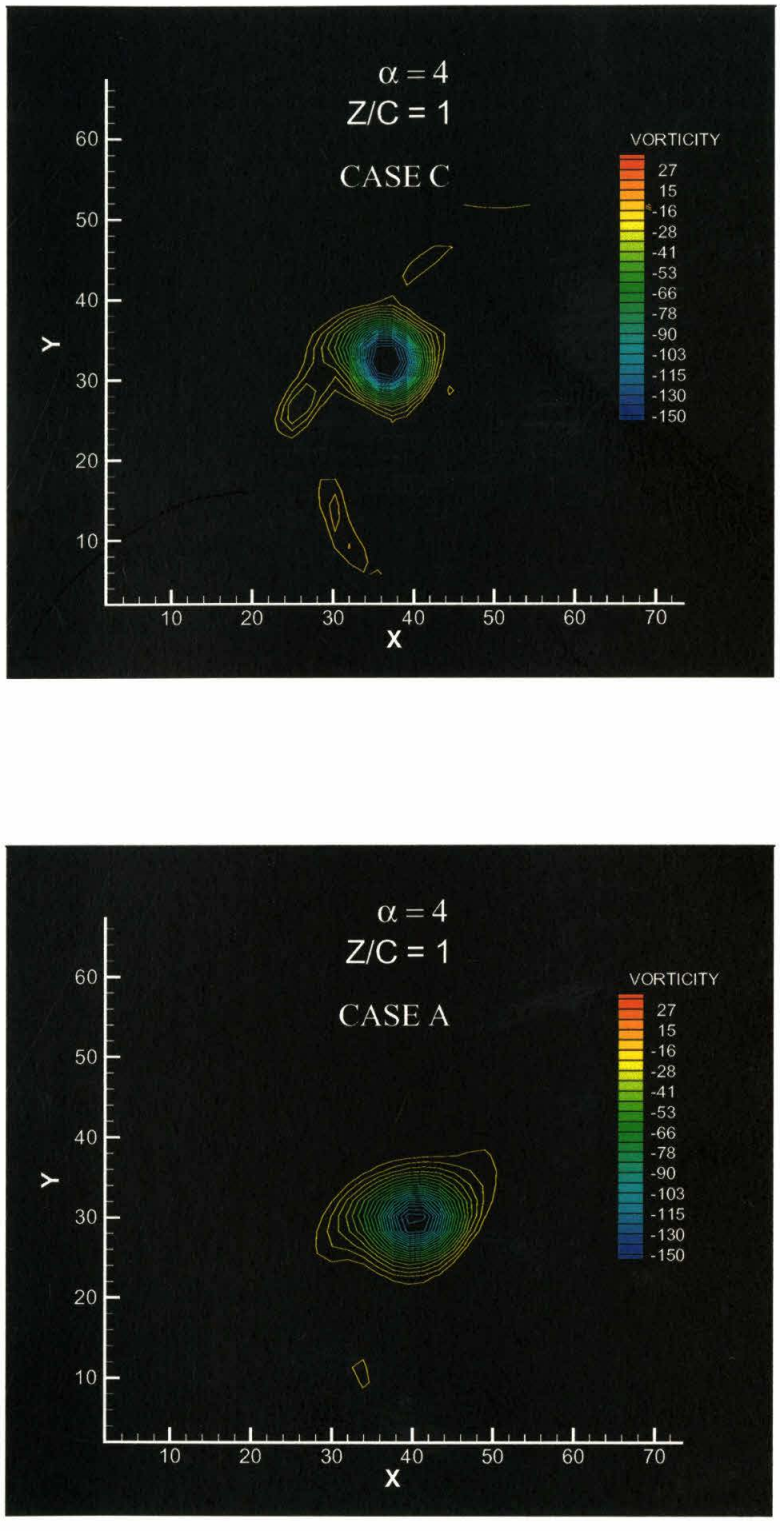

Figure 8.8. Tip geometry modification, axial vorticity field, $\alpha = 4^0$, Z/C = 1

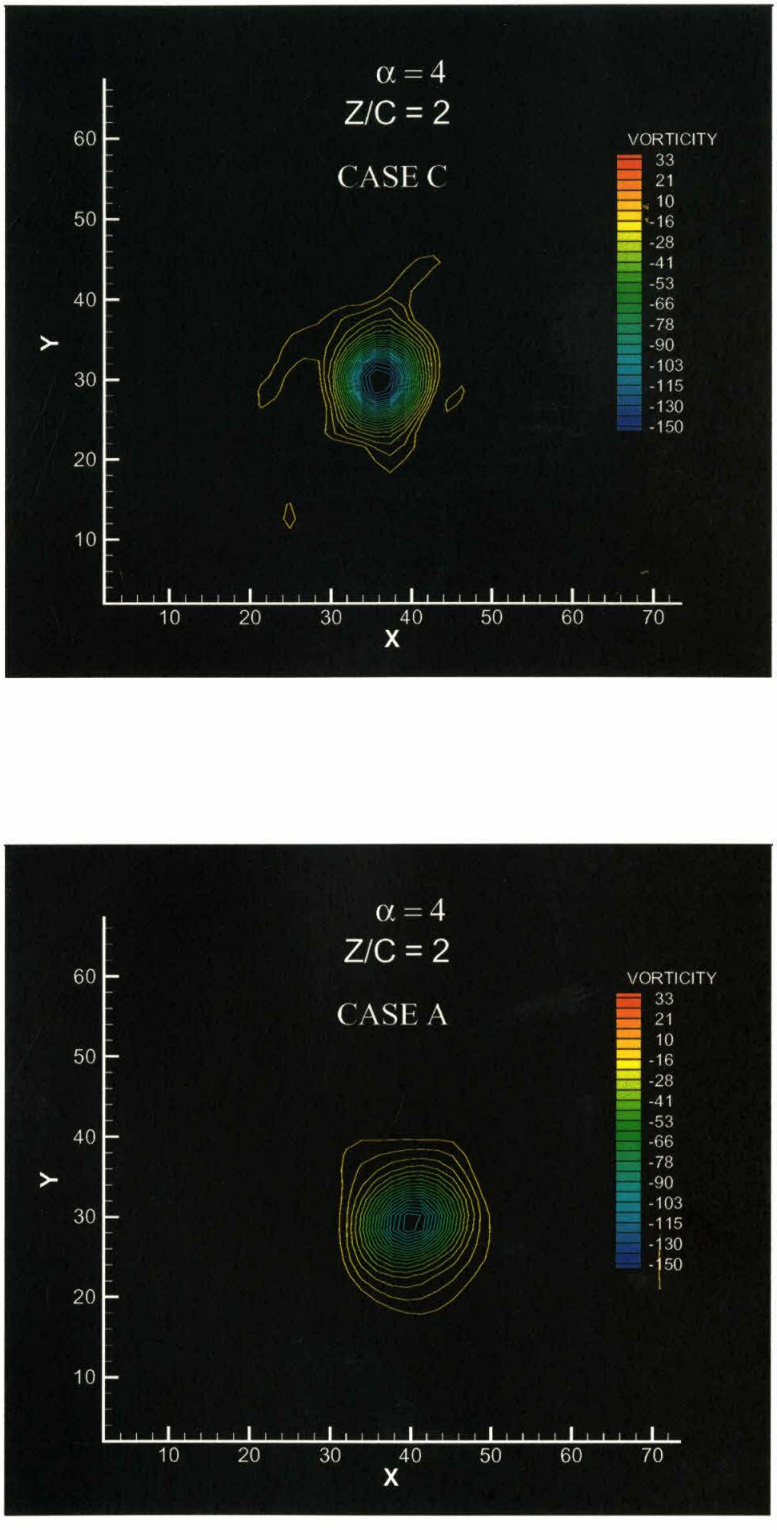

Figure 8.9. Tip geometry modification, axial vorticity field, $\alpha = 4^0$, Z/C = 2

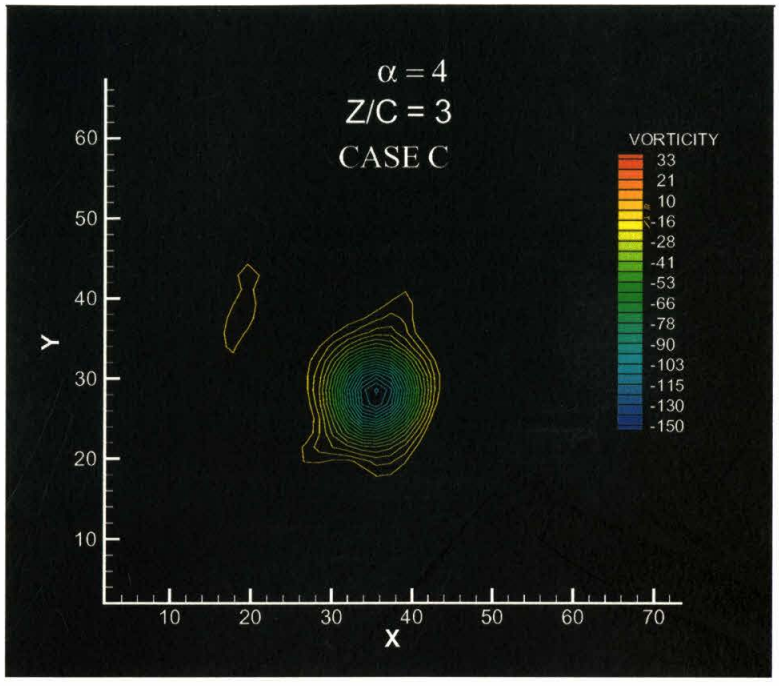

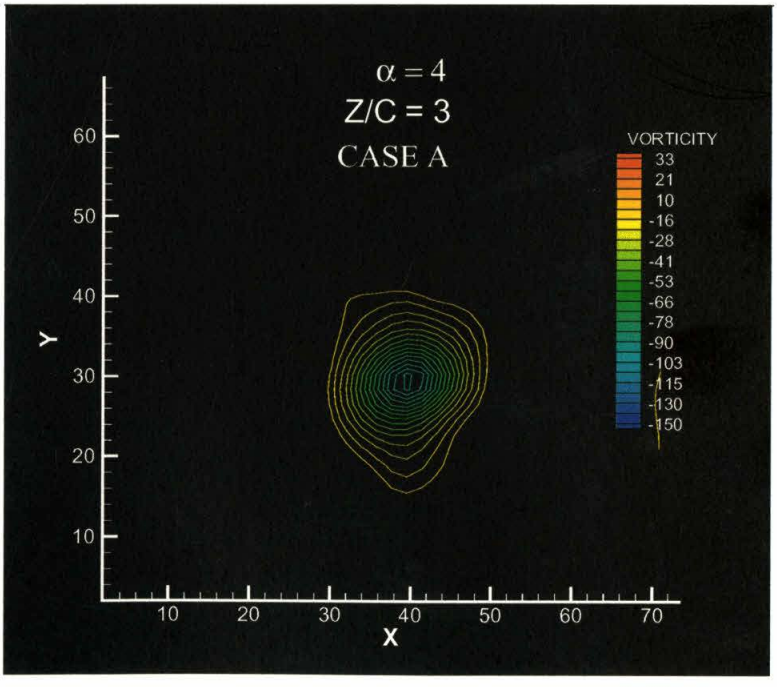

Figure 8.10. Tip geometry modification, axial vorticity field, $\alpha = 4^0$, Z/C = 3

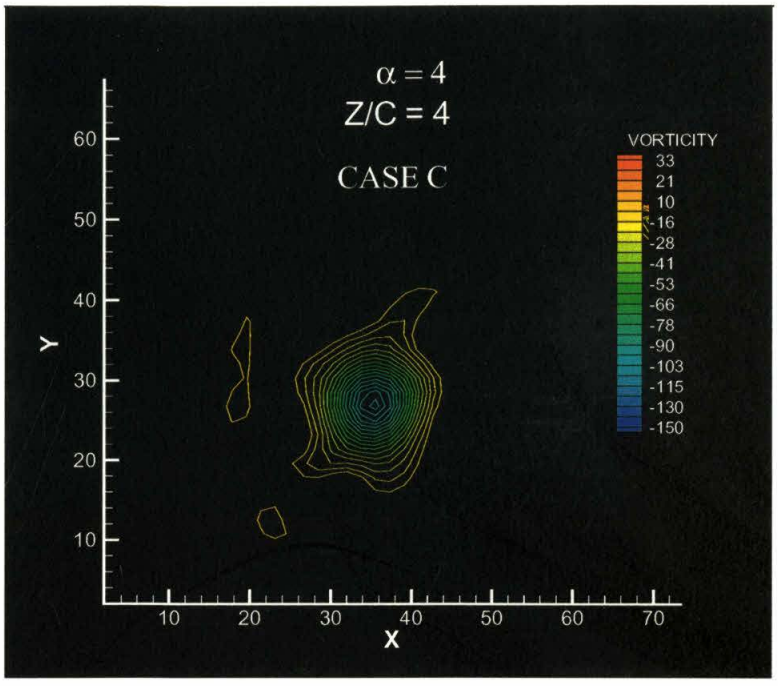

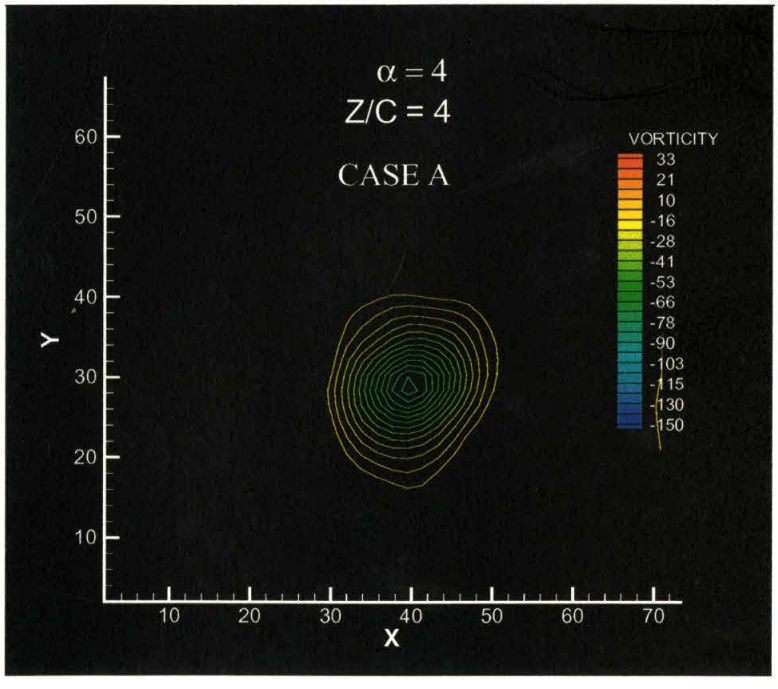

Figure 8.11. Tip geometry modification, axial vorticity field, $\alpha = 4^0$, Z/C = 4

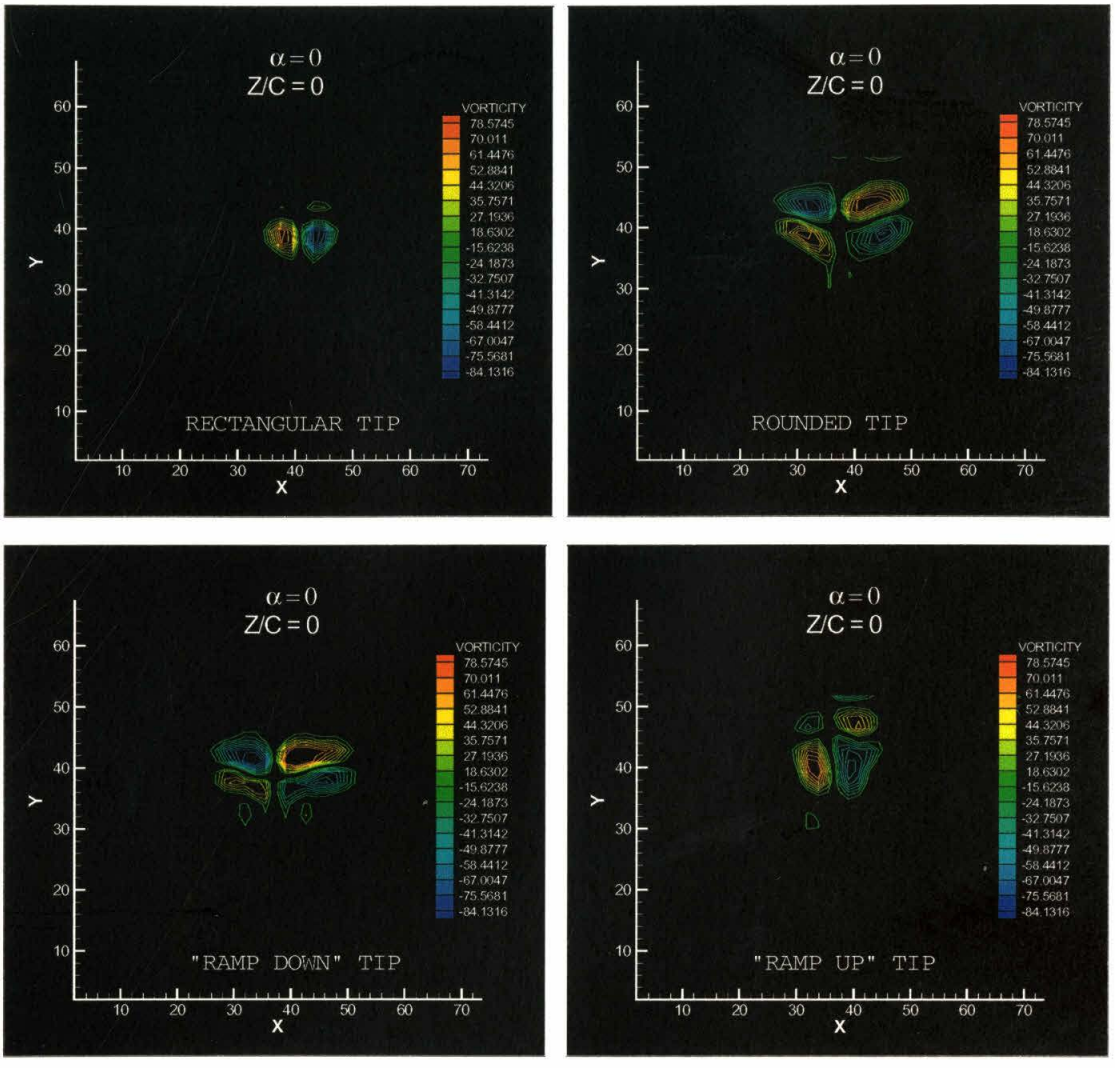

Figure 8.12. Comparison between different types of wing tip geometry

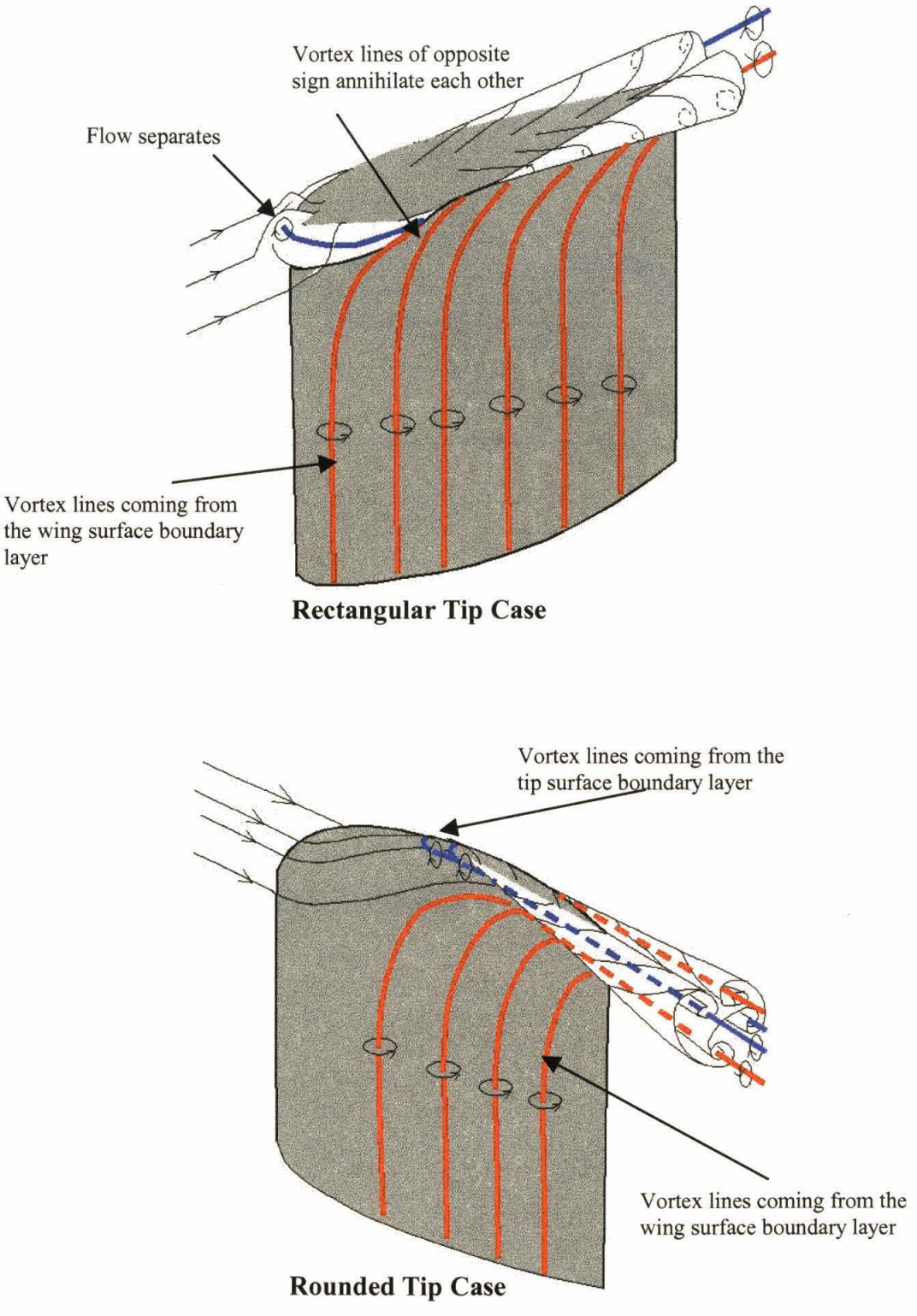

Figure 8.13. Generation of the vortices of opposite sign for $\alpha = 0^0$ case

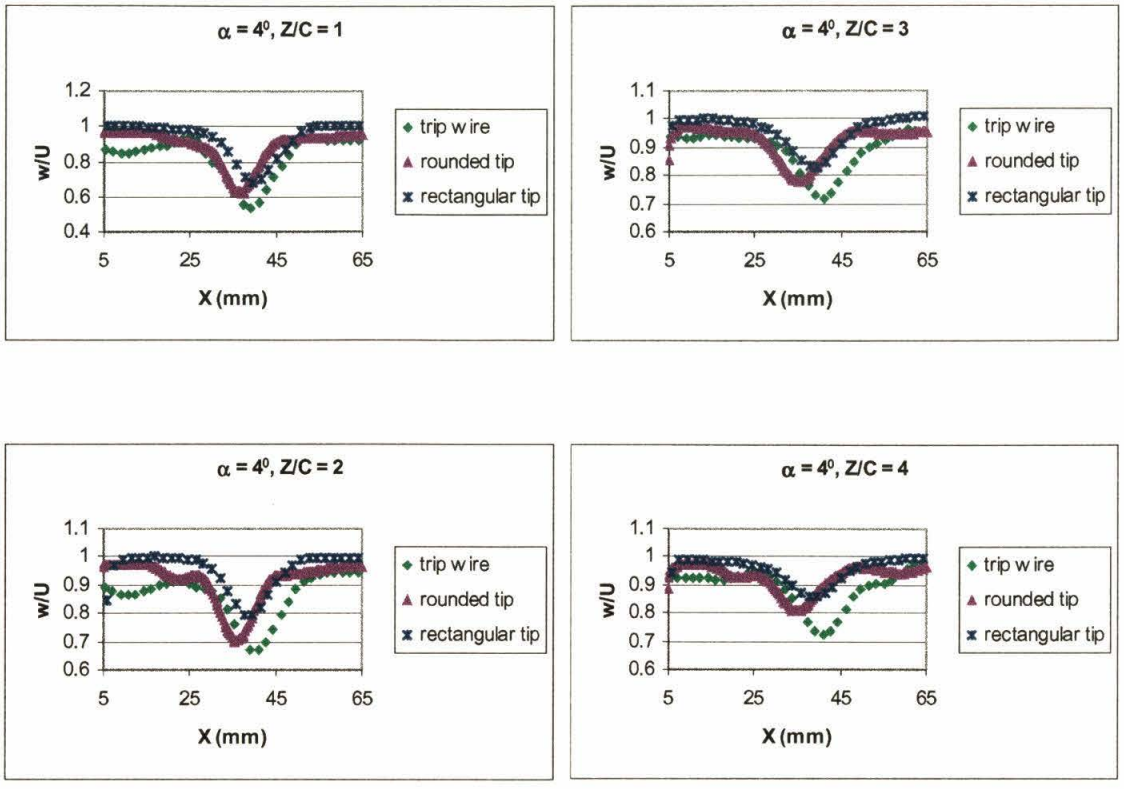

Figure 8.14. Comparison of the axial velocity profiles

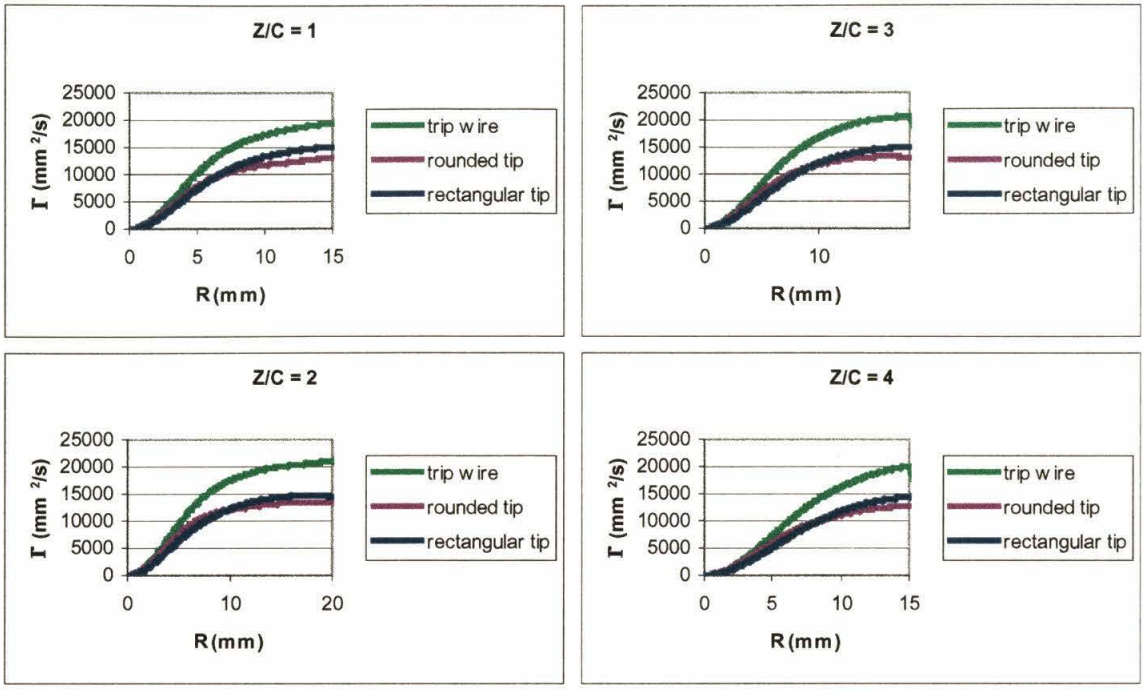

Figure 8.15. Comparison of the circulation profiles of the main tip vortex

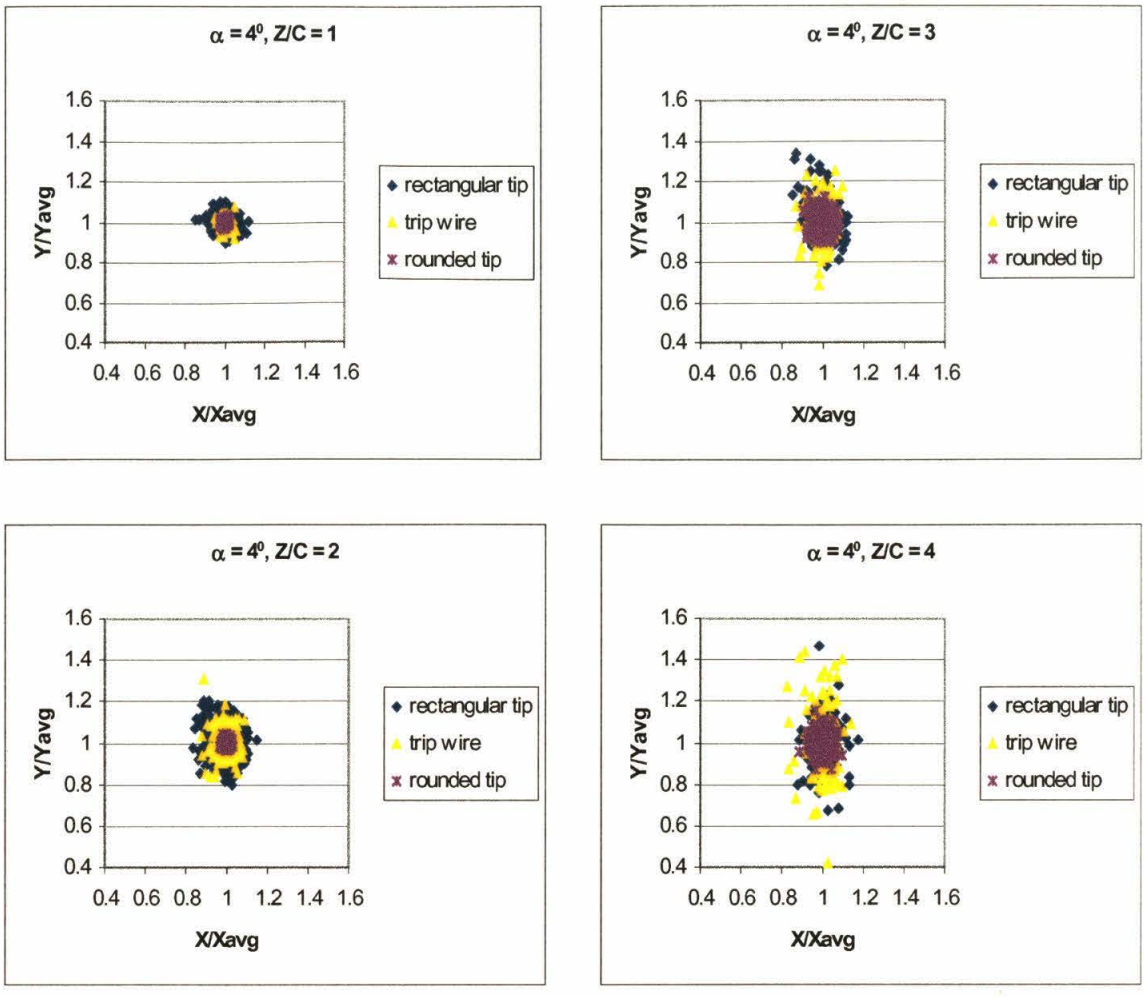

Figure 8.16. Instantaneous location of the vortex center for the three different cases

CHAPTER 9

Summary and Conclusions

An experimental investigation was carried out on the near field dynamics of the wing tip vortex. The trailing vortex was produced by a symmetric wing model, which has an NACA 0012 profile with an effective span of 41.91 cm and a chord length of 9.1cm. Two types of PIV methods, planar DPIV and stereoscopic PIV, were employed in this study. Both methods allow for measurement of in-plane velocity fields in planar slices that are oriented perpendicular to the freestream direction. In addition to the in-plane components, stereoscopic PIV also provided the out-of-plane velocity component within the planar slices. The global instantaneous velocity measurement techniques employed in this study resolve the problem of vortex meandering, which has been a problem in the past in performing accurate velocity measurements by using single point techniques. From the measured velocity fields, flow quantities such as axial vorticity fields and circulation can be calculated. All measurements are conducted at a Reynolds number, based on chord length, of 9040.

9.1 Velocity Field Behind the Wing

Measurements of velocity fields behind the wing were conducted using Stereoscopic PIV. Although many researchers have performed measurements of the

wing tip vortex velocity profiles in the past, the present work is the first attempt to measure all three velocity components within a plane instantaneously. The measurements reveal that the axial velocity inside the vortex core is lower than the freestream velocity in all cases considered in the study. Interestingly, results from measurements made at Z/C = 1 - 5 indicate that the contours of low axial velocity in the region near the tip vortex are elliptical, although the corresponding in-plane vector fields for such cases do not give any indication that the vortex is of elliptical shape.

In the relative coordinate system in which the fluid at infinity is at rest, the magnitude of the peak axial velocity deficit increases with the angle of attack. Also, for a given angle of attack, the core axial velocity deficit decreases with the downstream distance from the wing. The peak axial velocity is of the same order of magnitude as the peak tangential velocity. For a given α, the peak azimuthal velocity decreases with increasing Z/C (streamwise distance from the wing). The value of circulation at a given radial distance from the vortex center increases with the angle of attack. The circulation of wing tip vortex at the trailing edge is approximately 85% to 90% of the value of maximum circulation at stations farther downstream. The size of the vortex core increases with downstream distance, for all α cases. The trends of increasing or decreasing peak azimuthal velocity, peak axial velocity, and core size with increasing downstream distance from the wing agree with the theoretical predictions of Moore and Saffman (1973).

9.2 Vorticity Field Behind the Wing

Average streamwise vorticity fields at the trailing edge indicate that there are several streamwise vortices of opposite sign shed by the wing. At a zero angle of attack, two vortices of opposite sign with approximately the same strength were observed near the tip of the wing. As the incident angle of the wing is increased, the strength of one of these vortices (the one that would develop into the wing tip vortex) increases while the strength of the other decreases. In addition to the two vortices mentioned above, two layers of streamwise vorticity with opposite sign (one layer on the suction side and one layer on the pressure side) are observed at the trailing edge.

Downstream of the wing, the instantaneous fields reveals that the main vortex is surrounded by several satellite vortices. The sign of most of these satellite vortices is opposite that of the main vortex. At least one relatively strong satellite vortex appears in some of the instantaneous fields. Observations of the instantaneous core location suggest that the unsteady motion of the wing tip vortex is a result of interaction of the main trailing vortex with the satellite vortices. In the past, it was believed that the unsteady motion of the wing tip vortex, which is almost always observed in experiments, is due to the freestream turbulence.

9.3 Flow Adjacent to the Wing Tip

Measurements were made in regions adjacent to the wing tip by using planar DPIV. This is the first quantitative velocity field measurement ever conducted in this region by using a non-intrusive experimental technique. In the region near the leading

edge, the axial vorticity field shows the presence of vortices of opposite sign. At streamwise station corresponding to the place where the airfoil section reaches its maximum thickness, the pressure difference on the "pressure" and "suction" side of the wing start to drive the flow of air from the high-pressure side to the low-pressure side (for $\alpha = 4^0$). A structure that closely resembles a "wing tip" vortex is first observed on the suction side of the wing near the tip at the mid-chord. This structure continues to grow and eventually develops into the wing tip vortex farther downstream.

9.4 Effects of Boundary Layer and Tip Geometry

The effects of the boundary layer and wing tip geometry are also examined in the current study. The boundary layer is modified by placing a thin trip wire on the suction side of the wing surface. The measurement results from the boundary layer and the alternative tip geometry (rounded tip) modification were compared with the basic rectangular tip case. The results indicate that the axial vorticity fields are altered by the modifications. The trip wire breaks up the vorticity layer on the suction-side into smaller vortices. Also, the introduction of the trip wire delays the rollup process farther downstream. Two "small" vortices, with signs opposite that of the main vortex, are observed at the trailing edge in both cases (trip wire and rounded tip case). Both modifications also change the strength and the shape of the main vortex.

The results show that the structure of the wing tip vortex is very sensitive to the condition on the suction-side boundary layer and the wing tip geometry. The peak axial velocity deficit is the highest for the case in which a trip wire is placed on the suction side

and the lowest for the rectangular tip case. The value of the peak circulation is always the highest for the case with the trip wire and the lowest for the rounded tip case.

The effect of the modifications is also observed in the instantaneous location of the vortex center. The comparison of the instantaneous location of the vortex core, for the three different cases, supports the statement made earlier that the unsteady motion of the wing tip vortex is a result of an interaction process between the wing tip vortex and the satellite vortices

References

Baker, G. R., Barker, S. J., Bofah, K. K., Saffman, P. G., 1974, Laser anemometer measurements of trailing vortices in water, *Journal of Fluid Mechanics,* **65**, pp. 325-336

Batchelor, G. K., 1964, Axial flow in trailing line vortices, *Journal of Fluid Mechanics,* **20**, pp. 645-658

Bippes, H., 1977, Experimente zur Entwicklung der freien Wirbel hinter einem Rechteckflugel, *Acta Mechanica,* **26**, pp. 223-245

Chen, A. L., Jacob, J. D., Savas, O., 1999, Dynamics of corotating vortex pairs in the wakes of flapped airfoils, *Journal of Fluid Mechanics,* **382**, pp. 155-193

Crouch, J. D., 1997, Instability and transient growth for two trailing-vortex pairs, *Journal of Fluid Mechanics,* **350**, pp. 311-330

Crow, S. C., 1970, Stability theory for a pair of trailing vortices, *AIAA Journal,* **8**, pp. 2172-2179

Deshpande, N. A., 1999, An experimental investigation of high-shear-strain-rate behavior of metals, Eng. Deg. thesis, California Institute of Technology

Devenport, W. J., Rife, M. C., Liapis, S. I., Follin, G. J., 1996, The structure and development of a wing-tip vortex, *Journal of Fluid Mechanics,* **312**, pp. 67-106

Dritschel, D. G., 1995, A general theory for two-dimensional vortex interactions, *Journal of Fluid Mechanics,* **293**, pp. 269-303

Francis, M. S., Kennedy, D. A., 1979, Formation of a trailing vortex, *AIAA Journal*, **16**, pp. 148-154

Green, S. I., 1988, Tip vortices-single phase and cavitating flow phenomena, Ph.D. thesis, California Institute of Technology

Green, S. I., Acosta, A. J., 1991, Unsteady flow in trailing vortices, *Journal of Fluid Mechanics,* **227**, pp. 107-134

Hoffmann, E. R., Joubert, P. N., 1963, Turbulent line vortices, *Journal of Fluid Mechanics,* **16**, pp. 395-411

Houghton, E. L., Carpenter, P. W., 1993, Aerodynamics for engineering students, *Halsted Press.*

Jacob, J., Savas, O., Liepmann, D., 1997, Trailing vortex wake growth characteristics of a high aspect ratio rectangular airfoil, *AIAA Journal,* **35**, pp. 275-280

Jimenez, J., 1975, Stability of a pair of co-rotating vortices, *The Physics of Fluids,* **18**, pp. 1580-1581

Klein, R., Majda, A. J., Damodaran, K., 1995, Simplified equations for the interaction of nearly parallel vortex filaments, *Journal of Fluid Mechanics,* **288**, pp. 201-248

Krasny, R., 1987, Computation of vortex sheet roll-up in the Trefftz plane, *Journal of Fluid Mechanics,* **184**, pp. 123-155

Leblanc, S., Cambon, C., 1998, Effects of the Coriolis force on the stability of Stuart vortices, *Journal of Fluid Mechanics,* **356**, pp. 353-379

Logan, A. H., 1971, Vortex velocity distributions at large downstream distances, *Journal of Aircraft,* **8**, pp. 930-932

Moore, D. W., Saffman, P. G., 1973, Axial flow in laminar trailing vortices, *Proc. R. Soc. Lond. A.,* **333**, pp. 491-508

Moore, D. W., 1974, A numerical study of the roll-up of a finite vortex sheet, *Journal of Fluid Mechanics,* **63**, pp. 225-235

Ol, M. V., 2001, The passage toward stall of nonslender delta wings at low Reynolds number, Ph.D. thesis, California Institute of Technology

Park, H. G., 1998, A study of heat transport processes in the wake of a stationary and oscillating circular cylinder using DPIV/T, Ph.D. thesis, California Institute of Technology

Raffel, M., Willert, C. E., Kompenhans, J., 1998, Particle image velocimetry: a practical guide, *Springer.*

Saffman, P. G., 1993, Vortex dynamics, *Cambridge University Press.*

Sarpkaya, T., 1998, Decay of wake vortices of large aircraft, *AIAA Journal,* **36**, pp. 1671-1679

Shah, P. N., Atsavapranee, P., Hsu, T. Y., Wei, T., McHugh, J., 1999, Turbulent transport in the core of a trailing half-delta-wing vortex, *Journal of Fluid Mechanics,* **387**, pp. 151-175

Shekarriz, A., Fu, T. C., Katz, J., Liu, H. L., Huang, T. T., 1992, Study of junction and tip vortices using particle displacement velocimetry, *AIAA Journal,* **30**, pp. 145-152

Shekarriz, A., Fu, T. C., Katz, J., 1993, Near-field behavior of a tip vortex, *AIAA Journal,* **31**, pp. 112-118

Spalart, P. R., 1998, Airplane trailing vortices, *Annu. Rev. Fluid Mech.,* **30**, pp. 107-138

Vogt, A., Baumann, P., Gharib, M., Kompenhans, J., 1996, Investigations of a wing tip vortex in air by means of DPIV, *19th AIAA Advanced Measurement and Ground Testing Technology Conference,* **AIAA 96-2254**

Widnall, S. E., Bliss, D. B., 1971, Slender-body analysis of the motion and stability of a vortex filament containing axial flow, *Journal of Fluid Mechanics,* **50**, pp. 335-353

Widnall, S. E., 1975, Structure and dynamics of vortex filaments, *Annu. Rev. Fluid Mech.,* **7**, pp. 141-165

Willert, C. E., Gharib, M., 1991, Digital particle image velocimetry, *Experiments in Fluids,* **10**, pp. 181-193

Willert, C. E., 1997, Stereoscopic digital particle image velocimetry for application in wind tunnel flows, *Meas. Sci. Technol.,* **8**, pp. 1465-1479